

AD \_\_\_\_\_

Award Number: DAMD17-99-1-9404

TITLE: Opto-Acoustic Tomography for Early Detection of Breast Cancer

PRINCIPAL INVESTIGATOR: Alexander A. Oraevsky, Ph.D.

CONTRACTING ORGANIZATION: The University of Texas Medical Branch  
at Galveston  
Galveston, Texas 77555-0136

REPORT DATE: September 2001

TYPE OF REPORT: Annual

PREPARED FOR: U.S. Army Medical Research and Materiel Command  
Fort Detrick, Maryland 21702-5012

DISTRIBUTION STATEMENT: Approved for Public Release;  
Distribution Unlimited

The views, opinions and/or findings contained in this report are those of the author(s) and should not be construed as an official Department of the Army position, policy or decision unless so designated by other documentation.

20020717 049

# REPORT DOCUMENTATION PAGE

Form Approved  
OMB No. 074-0188

Public reporting burden for this collection of information is estimated to average 1 hour per response, including the time for reviewing instructions, searching existing data sources, gathering and maintaining the data needed, and completing and reviewing this collection of information. Send comments regarding this burden estimate or any other aspect of this collection of information, including suggestions for reducing this burden to Washington Headquarters Services, Directorate for Information Operations and Reports, 1215 Jefferson Davis Highway, Suite 1204, Arlington, VA 22202-4302, and to the Office of Management and Budget, Paperwork Reduction Project (0704-0188), Washington, DC 20503

<b>1. AGENCY USE ONLY (Leave blank)</b>		<b>2. REPORT DATE</b> September 2001	<b>3. REPORT TYPE AND DATES COVERED</b> Annual (1 Sep 00 - 31 Aug 01)	
<b>4. TITLE AND SUBTITLE</b> Opto-Acoustic Tomography for Early Detection of Breast Cancer			<b>5. FUNDING NUMBERS</b> DAMD17-99-1-9404	
<b>6. AUTHOR(S)</b> Alexander A. Oraevsky, Ph.D.				
<b>7. PERFORMING ORGANIZATION NAME(S) AND ADDRESS(ES)</b> The University of Texas Medical Branch at Galveston Galveston, Texas 77555-0136  E-Mail: <a href="mailto:alexander.oraevsky@utmb.edu">alexander.oraevsky@utmb.edu</a>			<b>8. PERFORMING ORGANIZATION REPORT NUMBER</b>	
<b>9. SPONSORING / MONITORING AGENCY NAME(S) AND ADDRESS(ES)</b> U.S. Army Medical Research and Materiel Command Fort Detrick, Maryland 21702-5012			<b>10. SPONSORING / MONITORING AGENCY REPORT NUMBER</b>	
<b>11. SUPPLEMENTARY NOTES</b>				
<b>12a. DISTRIBUTION / AVAILABILITY STATEMENT</b> Approved for Public Release; Distribution Unlimited				<b>12b. DISTRIBUTION CODE</b>
<b>13. ABSTRACT (Maximum 200 Words)</b>  The major efforts during the Year-2 project were made on testing LOIS in breast cancer patients scheduled for radical mastectomy (1-3 quarters) and on system modifications based on test results (4 <sup>th</sup> quarter). The research aims of the Year-2 were accomplished yielding over 50 two-dimensional optoacoustic images of 10 breast cancer patients. LOIS performance <i>in vivo</i> was compared with its performance <i>ex-vivo</i> in mastectomy specimens. The results demonstrated that LOIS produces high-resolution images of cancerous tumors <i>in vivo</i> with significantly enhanced contrast relative to x-ray mammography or ultrasound. The hypothesis that the optoacoustic contrast results from tumor angiogenesis is being tested by comparing images with immuno-histology. Further contrast enhancement method using nanoparticles was invented. During the Year-2 LOIS electronics was enhanced by a multichannel data acquisition system yielding images in close-to-real time (1 image per 2 seconds). Recommendations made for LOIS modification included: (1) widening the area of optical irradiation in order to cover a larger area of the breast and visualize tumors in greater details, (2) development of digital filters in order to improve resolution, (3) development of optoacoustic transducer array that integrates fiberoptic illumination and piezoelectric detection in order to achieve greater level of convenience for both, the patient and the radiologist. These modifications are being implemented in order to perform LOIS testing in radiology suite during the Year-3.				
<b>14. SUBJECT TERMS</b> Breast Cancer, tumor angiogenesis, laser, optoacoustics, imaging, diagnostics			<b>15. NUMBER OF PAGES</b> 64	
			<b>16. PRICE CODE</b>	
<b>17. SECURITY CLASSIFICATION OF REPORT</b> Unclassified	<b>18. SECURITY CLASSIFICATION OF THIS PAGE</b> Unclassified	<b>19. SECURITY CLASSIFICATION OF ABSTRACT</b> Unclassified	<b>20. LIMITATION OF ABSTRACT</b> Unlimited	

## Table of Contents

### ANNUAL REPORT 2001

(1).	FRONT COVER PAGE	.....	1
(2).	STANDARD FORM 298	.....	2
(3).	TABLE OF CONTENTS	.....	3
(4).	INTRODUCTION	.....	4
(5).	BODY OF REPORT	.....	4
(6).	KEY ACCOMPLISHMENTS	.....	9
(7).	REPORTABLE OUTCOMES	.....	9
(8).	CONCLUSIONS	.....	9
(9).	REFERENCES	.....	10
(10).	APPENDICES	.....	11

#### **(4) INTRODUCTION**

The subject of our project is the diagnostic imaging of breast tumors with new imaging technology, Laser Optoacoustic Imaging System (LOIS). The main merit of LOIS is significantly enhanced tissue contrast based on optical absorption. We are testing hypothesis that prevailing absorption of short laser pulses by advanced angiogenesis in tumors can convert these tumors into bright acoustic sources on the background of normal tissues with low optical absorption in the near-infrared spectral range. Ultrasonic waves, generated in tumors, can deliver diagnostic information to the breast surface, where signals may be detected by piezoelectric transducers. Reconstruction of two-dimensional images of breast sectors can be made on the basis of time-resolved detection and analysis of ultrasound signals detected with an array of transducers located at the breast surface. Optoacoustic tomography takes advantage of modern wide-band ultrasonography and solid-state laser technology. Particularly, we develop signal processing and image reconstruction algorithms based on methods employed in wide-band ultrasonography. Further advancement of ultrasonic detectors into ultrawide-band detection range (20kHz to 20MHz) opens possibility for further enhancement of the optoacoustic image resolution.

The major anticipated advantages of the laser optoacoustic imaging are as follows: (1) high optical contrast between tumors and normal tissues which results possibly from enhanced density of the microcirculation network within and around tumors and enhanced thermoelastic expansion coefficient in cancerous tumors; (2) high sensitivity of detection owed to efficient opto-thermal generation of pressure in tumors, and sensitive detection of resulting ultrasonic waves with novel piezoelectric transducers; (3) high (<1 mm) spatial resolution which results from pulsed laser excitation and time-resolved detection of ultrasonic signal profiles with array detectors; (4) substantial depth of monitoring (up to 8-cm) which results from deep penetration of the near-infrared photons in tissues, efficient conversion of laser energy into ultrasonic waves propagating through the breast with insignificant attenuation and minimal distortion, and from high sensitivity (>2 V/bar) of piezoelectric transducers; and (5) applicability to radiographically dense breasts.

#### **(5) BODY OF REPORT**

The purpose of this BCRP project is to incorporate laser excitation into a wide-band ultrasonography system (with a linear array probe) to yield a clinical prototype Laser Optoacoustic Imaging System (LOIS) and test this system initially in phantoms and then in breast cancer patients. The tissue phantoms with embedded blood vessels were designed to resemble natural optical and acoustic properties of breast and tumors with advanced angiogenesis. Patients with racial differences in skin types were included in the studies to account for variation in optical absorption properties. Clinical studies performed during the Year-2 of the project confirmed our hypothesis that the breast structural heterogeneity *in vivo* does not compromise the optoacoustic image quality and may be accounted for in the optoacoustic image processing.

During the second year period of the project all specific aims and milestones were accomplished. LOIS performance was improved by incorporating multichannel electronics system allowing real-time image acquisition. Initial clinical tests of the system were made on breast cancer patients. Specific details of the optoacoustic imaging system development and tests are presented below.

**Task 3 (Year 2):** Evaluation of the system using 50 patients with advanced cancer and scheduled for radical mastectomy (complete surgical removal of the breast).

**Milestones of Task 3 were accomplished.** The system performance was tested *in vivo* on 10 patients chosen from the examination group of 50 patients diagnosed with breast cancer and

scheduled for the radical surgical mastectomy. Not all patients were eligible for the optoacoustic imaging studies due to the fact that their tumors were very large, occupied substantial portion of the breast, were palpable and were often treated with radio- and chemo- therapy. These large tumors were clearly visualized with x-ray radiography and had significant radiographic contrast. Therefore, such tumors being an “easy target” for conventional breast imaging technologies, could not be used to test hypotheses outlined in our proposal. The following hypotheses were tested (i) whether LOIS is capable of detecting malignant breast tumors *in vivo*. (ii) whether contrast of optoacoustic images is greater than the contrast of x-ray radiography and ultrasound, and (iii) whether optoacoustic images of malignant tumors may be differentiated from that of benign tumors.

Fig. 1 presents typical optoacoustic images obtained *in vivo* from breast cancer patients. Procedure was performed in the surgery suite before radical mastectomy procedure.

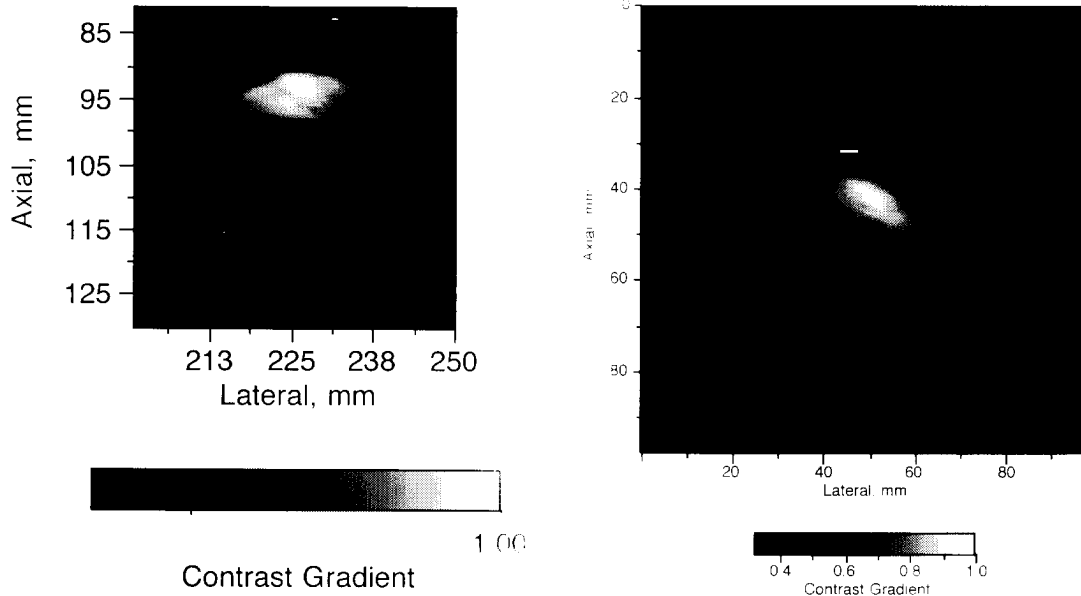


**Figure 1.** Optoacoustic image of a malignant tumor obtained *in vivo* (left, UTMB patient # X15221X), Optoacoustic image of a malignant tumor obtained *in vivo* (right, UTMB patient # X26372X). Note that the contrast is so significant that the entire background of normal tissue appears dark.

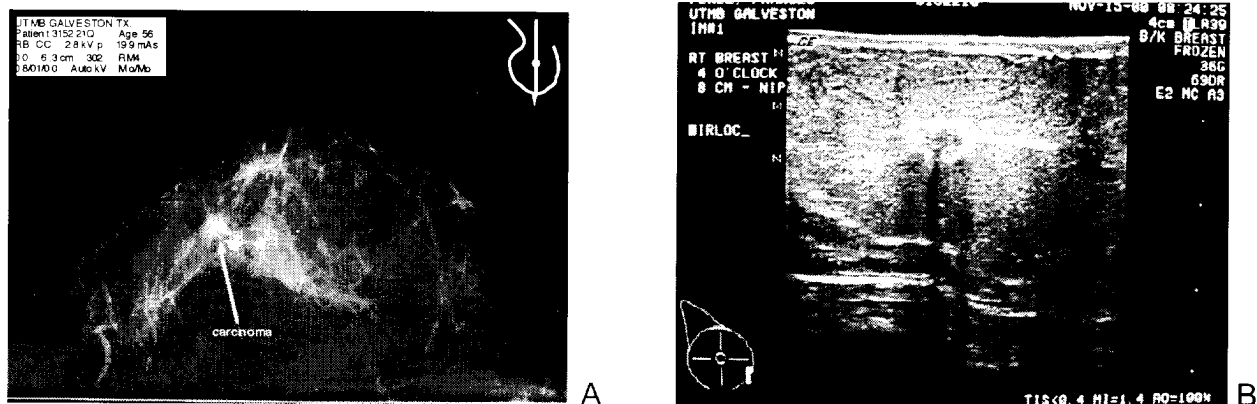


**Figure 2.** X-ray mammography image of a cancerous breast obtained *in vivo* with General Electric mamography system, Mo anode, Mo filter (A). There were 2 suspicious areas on mammogram, only one of them was a ductal carcinoma. Ultrasound image of the same breast showing malignant tumor obtained with Acuson 128 XP/10 3.5 MHz USI system (B). Note that contrast of the tumor relative to background is not sufficient to define exact shape and dimensions of this malignancy.

The contrast and precision of tumor localization in optoacoustic images were compared with that of conventional x-ray mammography and ultrasound images. The same breast was imaged *in vivo* with General Electric mammography system with Mo anode and Mo filter and with Acuson 128 XP/10 system employing 3.5 MHz C3-curved linear array transducer. These images are depicted in Fig. 2. X-ray image revealed two suspicious areas with no microcalcifications. A core-needle biopsy performed after x-ray screening proved that only one of the two suspicious areas was cancerous, and the other area of the breast similarly bright on mammography image was found normal. The ultrasound image of the same tumor was not very impressive. The core of the tumor and its boundaries can not be clearly seen in this image

Optoacoustic images were also correlated to the gross and histology / pathology of the mastectomy specimens. After optoacoustic imaging procedure, a surgical excision of the breast with tumor was performed (Dr. Declan Fleming) and given to a pathologist (Dr. Zoran Gatalica) who examined the mastectomy specimens in order to determine tumor geometry, location of tumors, the type of the tumor and (in selected cases) microvessel density. Laser safety of the system was also evaluated by pathologist. The optoacoustic imaging procedure was performed using laser fluence of 30-50 mJ/cm<sup>2</sup> which corresponds to one-third to one-half of maximum of permissible laser exposure for the skin in the near infrared spectral range, as described in American National Standards for Safe Use of Lasers. Pathology examination compared 10 specimen of tissue involved in optoacoustic imaging and 10 specimen of tissue not involved in optoacoustic imaging. No thermal or mechanical damage to normal tissues surrounding the tumors were found in association with optoacoustic imaging.

In order to perform optoacoustic imaging in real time only a single optical fiber was placed on the breast surface in locations thought to be above or near the tumor. Usually, 4 optoacoustic images were acquired from each breast examined *in vivo*. Thirty two optoacoustic signals were employed for data collection and subsequent image reconstruction. Optoacoustic contrast between the tumor and surrounding normal tissues *in vivo* exceeded 200% in all cases examined and was found equal to that earlier measured *in vitro* mastectomy specimen. This contrast is so significant that surrounding normal tissue look dark on the image. Such a contrast permits detection of small 2-mm tumors at the depth of 6-cm.

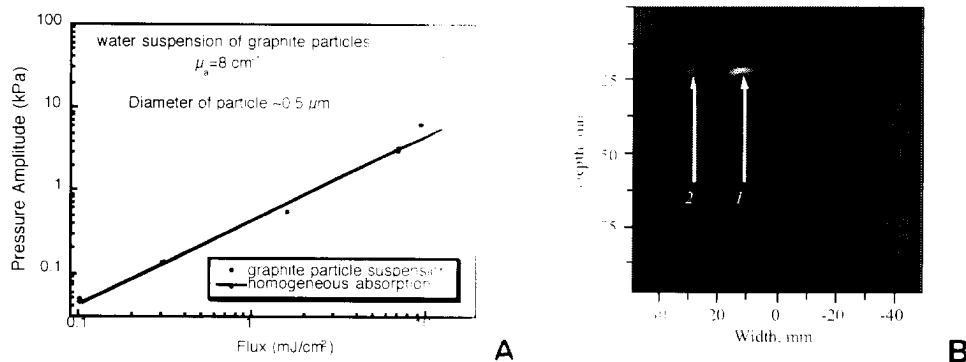


**Figure 3.** Optoacoustic signal amplitude in aqueous solution of nanoparticles as a function of incident optical energy (A). Note signal enhancement after the threshold optical fluence of 10 mJ/cm<sup>2</sup> is reached on the particles. Optoacoustic image of two small objects imbedded in the tissue-like gel phantom (B). Object #1 on the right was colored with absorbing nanoparticles, while object #2 on the left was colored with dye solution of equal absorption coefficient. In spite of equal absorption, the brightness of the object #1 is 10 times higher than the brightness of the object #2.

In the course of the project we invented possibility to further enhance optoacoustic contrast with gold nanoparticles that may be targeted selectively to malignant tumors. Thermodynamics teaches that heat capacity of the particles is proportional to the particle diameter cubed, while the absorbed portion of incident optical energy decreases only as the particle diameter squared. Thus, decrease

in particle diameter yields gradually increasing temperature of the particle subjected to constant fluence of laser energy. This, in turn, permits particle superheating without heating of surrounding tissue. In order to overcome the threshold for evaporation, photodissociation or other gas production at a safe level of laser fluence, the absorbing particles should have dimensions on the nanometer scale (30-150 nm). The optimal size of nanoparticles from the standpoint of optoacoustic efficiency is simultaneously just right for extended circulation of the nanoparticles in the blood stream. Intravenous injection of colloidal gold has been employed for treatment of rheumatoid arthritis for more than three decades and proved to produce tolerable toxicity. Therefore, we anticipate minimal or no accumulation of the proposed nanoparticulate contrast agent in normal cells. Gold is known a noble metal causing no visible toxicity in micromolar concentrations. The progress of the proposed research project will depend on success of development of biomolecule-nanoparticle coupling technique, allowing reliable conjugation of our nanoparticles with ligand peptides and antibodies specific to target-cells. A new grant application was submitted to BCRP-2001 requesting financial support for expansion of the optoacoustic imaging project with nanotechnology.

In order to demonstrate the utility of laser optoacoustic imaging for the quantitative measurement of the hemoglobin oxygenation in vascularized tumors, we have performed pilot experiments with gel phantoms containing embedded "arteries and veins".

The main chromophores in tissue that absorb radiation in the near-infrared range are oxygenated or deoxygenated molecules of hemoglobin in the blood. The contrast in laser optoacoustic imaging is a result largely of the fact that blood is unevenly distributed in tissue. Growing cancerous tumors develop an extensive network of blood vessels through the process of angiogenesis. These vessels are "leaky," and blood concentrates in the tissue of tumor tissue.

When laser optoacoustic imaging is performed with more than one wavelength of light, it has the power to reveal not only where blood is concentrated, but the level of blood oxygenated, measured by the relative concentration of oxygenated and deoxygenated hemoglobin molecules.

The pooled blood in cancerous tumors generally tends to be oxygen poor. The tumor consumes abnormally large amounts of oxygen in the process of active growth. Furthermore, leakage of the blood from the arteries of the tumor prevents its recirculation to the lungs for oxygen replenishment.

Thus, relatively few of the hemoglobin molecules in the blood in a cancerous tumor have an attached oxygen molecule.

Near-infrared radiation with a wavelength of 1064 nm is absorbed about 10 times more strongly by oxyhemoglobin molecules (those with an attached oxygen molecule) than by deoxyhemoglobin molecules (those free of oxygen). Laser optoacoustic imaging with this wavelength largely provides a map of the distribution of oxyhemoglobin.

Near-infrared radiation with a wavelength of 757 nm is absorbed more strongly by deoxyhemoglobin than by oxyhemoglobin molecules although both absorb sufficiently strongly to contribute to a laser optoacoustic image. Measurements made at both 1064 nm and 757 nm provide the necessary information for mapping both blood concentration and blood oxygenation.

The figure below illustrates the sensitivity of laser optoacoustic imaging to blood oxygenation. The phantom consisted of collagen gel mixed with whole milk that had been warmed up and diluted with enough water to give it optical properties similar to what the human breast would have, and then cooled down to solidify. Enough gelatin was dissolved to create a solid mass with a diameter of 12 cm comparable to most human breasts. Imbedded in the phantom were loops of polyethylene tubing to simulate blood vessels. In these loops was sheep blood that had been exposed to oxygen in varying degrees. As shown on the figure, the loop on the left contained blood that independent measures showed was 37% oxygenated. In other words, 37% of the hemoglobin molecules ( $O_2Hb$ ) had an attached oxygen molecule. The loop on the right was partitioned, and the top half contained 28% oxygenated blood, and the bottom half contained 92% oxygenated blood.

The known absorption properties of oxyhemoglobin and deoxyhemoglobin indicate that a laser optoacoustic image taken with a wavelength of 757 nm will show most intensely those portions of

the phantom that are rich in deoxyhemoglobin. These are the portions of the loops that are low in oxyhemoglobin. The laser optoacoustic image on the right of the figure indeed shows the top portion of the loop on the right most intensely, the loop on the left somewhat less intensely, and the bottom portion of the loop on the right least intensely.

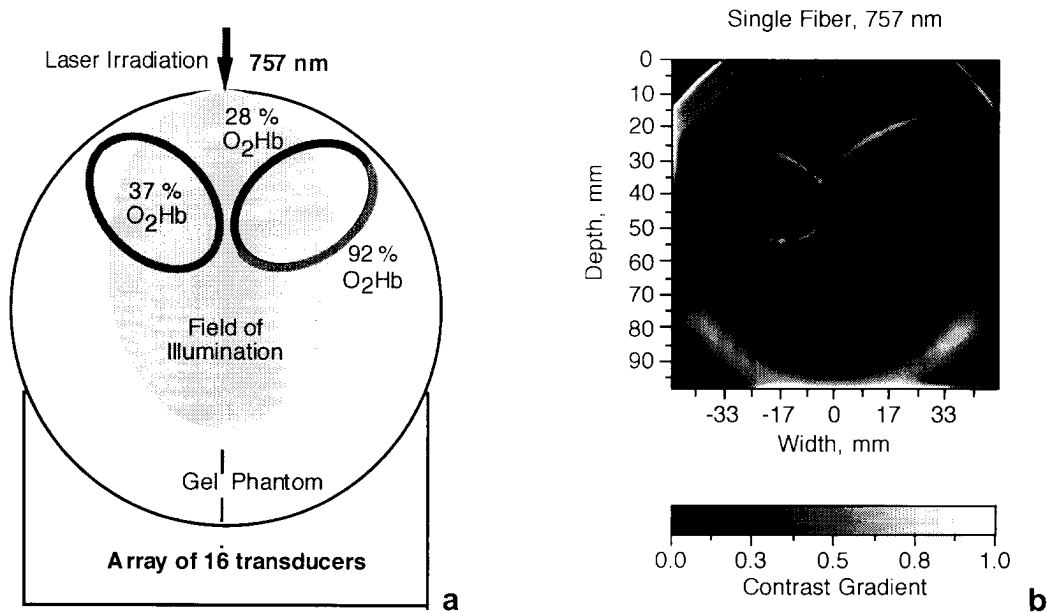


**Figure 4.** Schematic diagram (a) and two-dimensional optoacoustic image of two blood vessel loops in a gel phantom with optical properties similar to those of breast tissue *in vivo*. Imaging was performed using Alexandrite laser at 760-nm.

The test image shows clearly the power of laser optoacoustic imaging to resolve shapes and sizes of blood-filled tumors in the human breasts. It also illustrates the potential for measurement of the blood oxygenation levels of such tumors. This experimental image also contains a few imperfections. Most of the observed artifacts, such as the bright bands through the left loop result from the use of a single irradiation point and a rather small number of transducers in the detector array. These will become negligible when a newer detector array, under construction, is implemented in the course of the Year-3 of the project. The bright band at the bottom of the image near the detector array will be removed by a new filtration procedure.

Data of initial clinical experiments were analyzed, and recommendations were made for LOIS modification in order to improve its specifications and prepare for clinical studies in the radiology suite of patients with smaller breast tumors

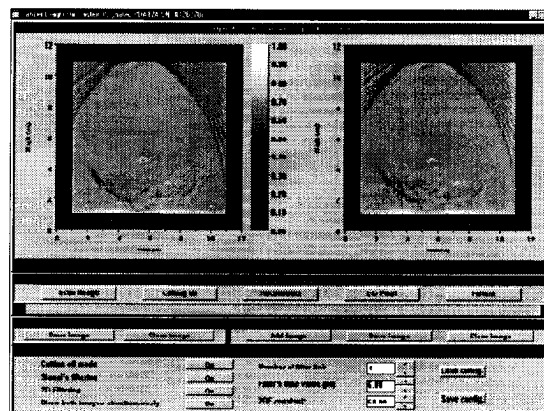


**Figure 5.** New LOIS computer interface for real-time imaging.

In order to optimize optoacoustic system characteristics from the standpoint of diagnostic efficacy, safety, resolution and sensitivity, such laser irradiation parameters as dynamic range and ultrasonic bandwidth of the acoustic detection were varied. Optimal parameters of the array transducer were found to be as follows: (1) ultrasound detection bandwidth: 20 kHz to 4 MHz, dimensions of each transducer 35 mm x 1mm with 1 mm gaps, 64 piezoelements total in 120<sup>0</sup> linear array with diameter of 120 mm. Sensitivity of such transducer made of PZT-5H ceramic embedded in polymer-epoxy resin with 2-2 structure was exceptionally high, >2 V/bar with effective noise pressure of only 4  $\mu$ bar. In the course of the next year project we also plan to use two different wavelengths of laser irradiation, so that diagnostic capability of LOIS can be tested.

## **(6) KEY ACCOMPLISHMENTS**

- Laser Optoacoustic Imaging System (LOIS) was modified and enhanced to operate in real time and at two wavelengths of Nd:YAG or Alexandrite lasers, which should enable diagnostic capability of optoacoustic imaging.
- LOIS was tested in gelatin phantoms simulating dense breast with blood vessels having blood with various degree of oxygen saturation. Experiments demonstrated that LOIS is capable of not only visualizing shape and dimensions of blood vessels, but also differentiating deoxygenated blood from oxygenated blood.
- LOIS was tested in breast cancer patients scheduled for radical mastectomy. Tests demonstrated that LOIS can visualize malignant tumors in vivo with contrast significantly exceeding the contrast of x-ray mammography or ultrasound images.

## **(7) REPORTABLE OUTCOMES**

- Manuscripts: 3 published, 2 in press, 2 submitted, 1 in preparation, Abstracts – 7, Presentations acknowledged USAMRMC support – 7.
- Patents: 1 patent application USPTO # 60/147,577 entitled: “Optoacoustic Monitoring of Blood Oxygenation” (with co-inventors: Rinat Esenaliev, Donald Prough, and Massoud Motamedi). Inventor’s response to the US Patent Office action was submitted.
- Based on work supported by this award the following grant applications were submitted:
  - 1) US Civilian Research and Development Foundation, Co-PI, “Development of algorithms and software codes for 3D optoacoustic tomography”, \$56,800 (funded).
  - 2) Cancer Research Foundation of America, “Quantitative tomography of early detection of Colorectal Cancer”, \$40,000 (awarded).
  - 3) USAMRMC Prostate Cancer Program-2001, “Novel imaging system for early detection of prostate cancer”, \$558,600 (pending).
  - 4) USAMRMC Breast Cancer Program-2001, “Diagnostics of microscopic breast cancer using smart nanoparticles as an optoacoustic contrast agent”, \$402,489 (pending).
  - 5) NIH/NCI, “Diagnostic imaging of blood in breast tumor angiogenesis”, \$1,049,936 (pending).

## **(8) CONCLUSIONS**

- Laser Optoacoustic Imaging System is a useful modality for detection of breast cancer, which provides enhanced tissue contrast. Limits of small tumor detection and diagnostic capability of LOIS may be established in the course the Year-3 project.

## (9) REFERENCES

1. Valeri G. Andreev, A.A. Karabutov, A.A. Oraevsky: "Wide-band acoustic pulse detection in opto-acoustic tomography system", *IEEE Trans Image Proc.*, 2001 (to be submitted).
2. A.A. Oraevsky, A.A. Karabutov, V.A. Andreev, H. Singh, Z. Gatalica, R.D. Fleming: Clinical evaluation of the opto-acoustic imaging for breast cancer, *Radiology*, 2001 (submitted)
3. P.S. Grashin, A.A. Karabutov, N.B. Podymova, I.M. Pelivanov, E.V. Savateeva, A.A. Oraevsky: Time-resolved laser optoacoustic measurement of optical properties in turbid media, *Applied Optics 2001 (submitted)*.
4. A.A. Oraevsky, A.A. Karabutov, V.S. Solomatin, E.V. Savateeva, V.G. Andreev, Z. Gatalica, H. Singh, R.Y.D. Fleming: Laser optoacoustic imaging of breast cancer *in vivo*, *Proc. SPIE* 2001; **4256**: 6-15.
5. E.V. Savateeva, A.A. Karabutov, A.A. Oraevsky: Real-time optoacoustic monitoring of substance penetration in tissues, *Proc. SPIE* 2001; **4256**: 61-69.
6. V.G. Andreev, D.A. Popov, D.V. Sushko, A.A. Karabutov, A.A. Oraevsky: Inverse Radon transform for optoacoustic imaging, *Proc. SPIE* 2001; **4256**: 119-129.
7. A.A. Karabutov, E.V. Savateeva, A.A. Oraevsky: Optoacoustic supercontrast for early cancer detection, *Proc. SPIE* 2001; **4256**: 179-187.
8. A.A. Karabutov, E.V. Savateeva, V.G. Andreev, S.V. Solomatin, R.D.Y. Fleming, Z. Gatalica, H. Singh, M.P. Henrichs, and A.A. Oraevsky: "Optoacoustic images of early cancer in forward and backward modes", *Proc. SPIE* 2001; **4443**: 21-33. (invited).
9. A.A. Oraevsky, A.A. Karabutov, E.V. Savateeva: "Enhancement of optoacoustic tissue contrast with absorbing nanoparticles", *Proc. SPIE* 2001; **4443**: 44-52.

# Laser optoacoustic imaging of breast cancer *in vivo*

Alexander A. Oraevsky<sup>1</sup>, Alexander A. Karabutov<sup>1</sup>, Sergey V. Solomatin<sup>1</sup>,  
Elena V. Savateeva<sup>1</sup>, Valeri G. Andreev<sup>1\*</sup>, Zoran Gatalica<sup>2</sup>, Harbans Singh<sup>3</sup>, R. Declan Fleming<sup>4</sup>

<sup>1</sup>Center for Biomedical Engineering, <sup>2</sup>Department of Pathology, <sup>3</sup>Department of Radiology,  
<sup>4</sup>Department of Surgery, University of Texas Medical Branch, Galveston, TX, 77555

## ABSTRACT

A clinical prototype of the laser optoacoustic imaging system (LOIS) was employed for breast cancer detection and localization in patients with confirmed breast cancer and scheduled for radical mastectomy. The prototype LOIS used a single optical fiber for delivery of laser pulses, an arc shaped 32-element PVDF transducer array for ultrawide-band piezoelectric detection of optoacoustic signals and a single-channel data acquisition card for signal processing. The resonance ultrasound frequency of the 110  $\mu\text{m}$  PVDF film was outside detectable range of ultrasound. Spatial resolution of the transducer array was slightly better than 1mm in radial direction and slightly worse than 1 mm in lateral direction. The system was optimized for contrast and sensitivity. Data acquisition, signal conditioning and image processing were significantly improved and optimized resulting in reduced image frame rate of 2 seconds employing 700 MHz Aphlon processor. The computer code for digital signal processing employed band-pass hyper-Gaussian filtering and denoising. An automatic recognition of the optoacoustic signal detected from the irradiated surface was implemented in order to visualize the breast surface and improve the accuracy of tumor localization. Radial back-projection algorithm was employed adopting combination of integration along spherical wavefronts and integration along planar wavefronts (as in Radon transform) for image reconstruction. The system performance was evaluated initially in breast tissue-like phantoms with embedded blood vessels. Clinical studies in breast cancer patients scheduled for surgical mastectomy were performed and compared with x-ray radiography, ultrasound and pathology reports.

**Keywords:** *Optoacoustic imaging, breast cancer, ultrawide-band acoustic transducer, laser, ultrasound*

## 1. INTRODUCTION

Laser optoacoustic imaging system (LOIS) was proposed for cancer detection in order to combine advantages of optical contrast and sensitive, high-resolution ultrasonic detection in one tomography system [1-4]. One of the major applications is the detection of early breast cancer, especially in younger women. The optoacoustic tomography utilizes analysis of profiles of acoustic signals induced by laser pulses in breast tissue with tumors [5-8]. Application of the ultrawide-band ultrasonic detection instead of detection of photons in optoacoustic tomography helps to overcome two problems associated with strong light scattering in biological tissues and improve depth of monitoring, sensitivity and spatial resolution [9-12]. The profiles of acoustic waves generated under irradiation conditions of temporal pressure confinement in the volume of tumors resemble the profile of absorbed laser energy in the tumors, and can be used to replicate the tumor structure. Tumors with dimensions of 1.5-mm to 15-mm irradiated with laser pulses represent themselves as sources of acoustic waves with ultrasonic frequencies of  $\sim 1$  MHz to  $\sim 100$  kHz. Such ultrasonic waves can propagate in biological tissues with insignificant attenuation [12-13]. However, spherical propagation of acoustic waves changes initial profile of absorbed laser energy (especially in the ultrasonic frequency range  $\leq 1$  MHz), so that the detected signals must be processed by integrating them over the entire time-course of detection in order to be used in the optoacoustic image reconstruction [13-15].

The first few years of our research in the area of optoacoustic imaging of the breast yielded the following results: (1) first clinical prototype system for breast imaging was developed, fabricated and extensively tested in phantoms [10,12], (2) detection and localization of breast tumors in surgical mastectomy specimens were demonstrated [15], (3) parameters of optoacoustic were compared with X-ray mammography, MRI and ultrasound imaging [15,16]. The main merit of optoacoustic imaging was found to be the significant tissue contrast. The image contrast is defined as the difference in optoacoustic image brightness in tumors and in adjacent normal tissue divided to the brightness of normal tissue background. This contrast was found in the range of 1 to 5, which substantially exceeds any other endogenous tissue contrast currently utilized in clinical ultrasonography, MRI and X-ray mammography (usually much less than 1). Based on literature data and our gross observations of tumor cross-sections we hypothesize that the optoacoustic contrast results primarily from increased optical absorption in the dense microvasculature of the tumors [12,17]. However, optical scattering in tumors, especially

those treated with chemo- and radiotherapy, may also significantly contribute to the optoacoustic contrast [18]. Thermoelastic properties of the breast tumors may also add to the optoacoustic contrast, however, were not yet quantified [19]. The lateral resolution of acoustic transducer array was improved relative to that in the system used previously *in vitro*. Comparison of optoacoustic images with those of X-ray radiography, MRI and ultrasound imaging performed *in vitro* revealed good correlation in tumor size and location, and the spatial resolution equal to that of ultrasound (better than 1 mm) was achieved [15].

In this paper, we report initial results of *in vivo* clinical studies involving patients with breast cancer. The clinical optoacoustic system LOIS was assembled of a compact Nd:YAG laser, fiberoptic light delivery system, an arc-array of 32 wide-band acoustic transducers, and a data acquisition board operated by computer. Design of the new system is compact and suitable for performing studies *in vivo*. New signal and image processing employed permitted reconstruction of optoacoustic images in 1 second after data collection.

## 2. MATERIALS AND METHODS

### 2.1. LOIS for clinical studies

Schematic diagram of LOIS-02 is shown in Fig. 1a. A Nd:YAG laser (Big Sky Lasers, MA) operating at the wavelength of 1064 nm was used as a source of near-infrared pulses of 10-ns duration. Repetition rate of laser pulses was 20 Hz. A quartz optical fiber was employed for the laser pulse delivery to the tissue surface. A telescope was used to expand laser beam from the fiber and deliver a parallel beam with diameter of 1-cm to the surface of skin. A glass window was in contact with tissue during irradiation assuring the exact position and providing rigid surface conditions for acoustic pressure coupling. Rigid surface of the irradiated tissue permitted more effective generation of higher ultrasound frequencies at the very surface for better determination of the surface position in the detected signals. This method of irradiation also resulted in generation of minimal tensile pressure, yielding safe laser irradiation conditions [6].

### 2.2. Arc array of ultrawide-band acoustic transducers

A specially designed array of PVDF acoustic transducers was employed in LOIS. The array had 32 rectangular piezoelectric transducers of 1.5 x 12 mm dimensions and 4 mm distance between transducers (see Fig.1). Piezoelectric polymer PVDF of 110- $\mu$ m thickness was used for transducer fabrication. Low acoustic impedance and ability to operate in the ultrawide ultrasonic frequency band without strong resonance and reverberations are the advantages of PVDF for detection of opto-acoustic profiles. Backing material was used for mechanical matching of transducer and damping reverberations after detection. The transducers were located on arc surface of 120-mm diameter. A limited viewing angle of 120 degrees resulted in reduced lateral resolution of 1.5-mm compared with in-depth resolution of 0.8-mm. On the other hand, this geometry provided sufficient resolution in a wide area around the focal zone.

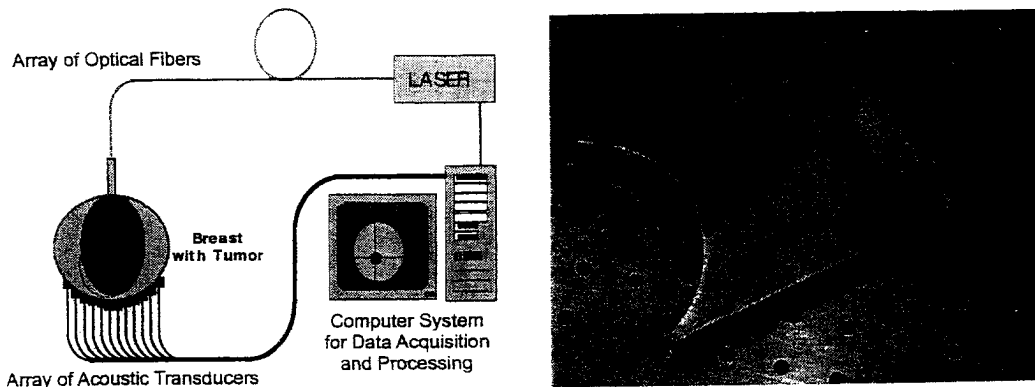


**Figure 1.** Schematic diagram of clinical LOIS (a) and a photograph of the 32-element arc transducer array (b).

Absolute sensitivity of each transducer in the array was measured. Results of this calibration were used in normalizing signals to the sensitivity of each transducer. The mean sensitivity value for transducer array of  $S = 10 \mu\text{V}/\text{Pa}$ . Electric capacity of each transducer was approximately  $C_{pe} = 40 \text{ pF}$ , which resulted in effective noise level of  $20 \mu\text{V}$  as shown in

Figure 2. Electrical voltage corresponding to the effective noise pressure,  $\Delta p$ , can be calculated for a transducer operating in the idler (open circuit) mode as follows [18]:

$$U_{noise} = gl\Delta p = 4.6 \sqrt{\frac{kT_0}{C_{pe}}} \quad (1)$$

where  $g$  is the piezoelectric modulus,  $l$  is the thickness of the piezoelement,  $kT_0$  is the room temperature and  $C_{pe}$  is the electric capacity of the piezoelement. Simultaneously this value of electric capacity is sufficient for effective coupling of electrical signals from transducers into the charge preamplifier and signal processing circuitry.

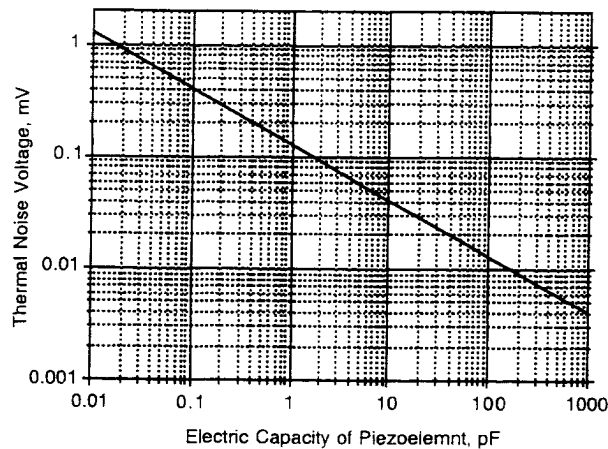


Figure 2. The effective thermal noise pressure in PVDF acoustic transducers as a function of transducer electric capacity.

## 2.2. Signal Filtering in LOIS

The major part of signal processing in LOIS involves various filtering procedures. Each signal detected by acoustic transducers in the array consists of the following three components: (1) a sharp peak produced at the very subsurface layer of the irradiated tissue (a product of tissue local absorption and effective subsurface laser fluence), (2) a low-frequency smooth exponential slope produced by the attenuation of light intensity inside tissue ( $\mu_{eff} \approx 1$ ), and (3) short N-shaped pulses generated by small absorbing tumors. The duration of the N-shaped pulses is defined by the time of sound propagation through the dimension of the tumor in the direction of detection. The time-delay of the optoacoustic signal arrival depends on tumor location relative to the transducers in array. Therefore position of the tumor and its dimensions can be determined from the optoacoustic signals detected by LOIS.

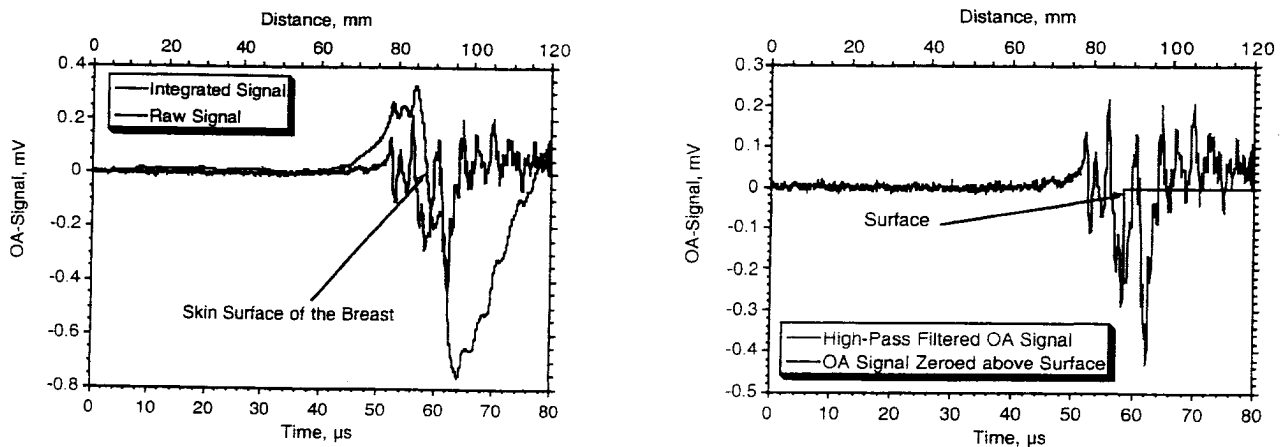
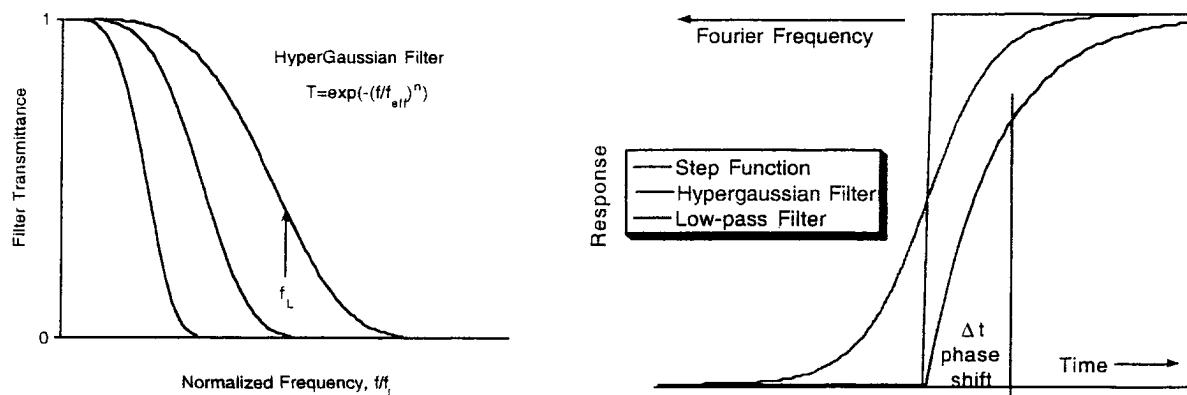


Figure 3. Typical optoacoustic signal detected by a central transducer in array from a breast with tumor and the same signal after integration procedure converting the signal into a profile of absorbed energy distribution (left panel), and the optoacoustic signal zeroed down at the surface position (right panel).

The signal generated by laser pulses in the subsurface layer (very close to the surface) possesses maximum amplitude over the entire time-period of detection. Therefore, the signal gradient is maximal at the tissue surface, which yields high ultrasound frequencies. High ultrasound frequencies that fall near the resonance frequency,  $f_{max}$ , of piezo-elements can induce significant reverberation in the transducer. Our transducers were designed to damp resonance frequencies and widen the range of detectable frequencies. Nevertheless, a strong reverberation takes place after the arrival of the signal from the surface of tissue. These reverberations do not affect the useful part of the optoacoustic profile. Besides, it is convenient to employ the sharp peak with high gradient (derivative) for automatic determination of the tissue surface. The surface position can be accurately detected at the intersection of integrated signal with zero line (see Fig. 3, left panel). The controlling computer generated numerical signal at the surface position determined for each transducer and stored these data in a separate file. All data samples were equaled to zero after the arrival of the signal generated at the tissue surface. The surface-marks generated by computer were used for the surface visualization. Combined image contained surface marks and the image of breast tissue with tumors, showing tumor location relative to the irradiated surface.

Before the integrated signal could be used for image reconstruction, it is often desirable to eliminate or reduce its low frequency component associated with homogeneous light attenuation inside the tissue, because it can significantly decrease the image contrast. This was achieved in LOIS with high-pass Gaussian filtering with RC cells. The value of  $RC \sim 10 \mu s$  defines the cut-off ultrasonic frequency, and the sharpness of the filter cut-off is defined by the number of RC cells. The greater the number of elementary RC cells, the steeper the slope of the filter transfer function. The cut-off frequency and the slope of the transfer function of the filter could be varied conveniently by the radiologist-operator.



**Figure 4.** Hyper-Gaussian filter transfer function (left panel) and filter responses for various types of RC filters (right panel).

In case when large tumors are present in the breast, the optoacoustic signals coming from tumors carry significant low-frequency component. Therefore, elimination of exponential trend associated with effective optical attenuation in tissue may simultaneously remove useful information about tumor internal structure from the image. Ideal filter would be represented by a step-function 0-to-1 with infinitely sharp slope. However, real filter possess certain resolution, yielding smooth slope from 0-to-1 over a period of its RC constant. It is important to note that the standard RC filter can have a level greater than zero only after it is initiated. The “inertia” of a standard RC filter produces not only widening of signals after filtration, but also delays of the signal components relative to their original positions on the time course. These delays mean phase shifts in the frequency domain and result in blurring of optoacoustic images reconstructed using signals filtered with a standard RC-filters. Figure 4 (left) shows graphically the difference between an ideal step-function and a real filter. To avoid, the problem of phase-shifts upon filtering, we employed Hyper-Gaussian filters with variable parameters for band-pass filtering of integrated optoacoustic signals:

$$G = \exp\left[-\left(\frac{f}{f_{eff}}\right)^n\right] \tag{1}$$

where  $G$  is the filter transfer function,  $f$  is the ultrasonic frequency in optoacoustic signals,  $f_{eff}$  is the effective cut-off frequency, and  $n$  is the hyper-Gaussian parameter. The graphical expression of this filter is depicted in Figure 4 (right panel). Integrated signals filtered from high frequency noise were used as input data for the image reconstruction code.

Application of the filters shown in Fig. 4 for elimination of high-frequency noise and low-frequency exponential trends in optoacoustic signals yielded profiles without widening or delays in signal components. Figure 5 depicts integrated optoacoustic signal before and after filtering low-frequency components with hyper-Gaussian filter. In spite of generally satisfactory results, some distortions can be observed after filtration, showing artifacts of negative signal values, minor inside tissue and especially noticeable above the tissue surface. Any artifacts in the signals were equaled to zero before the image reconstruction.

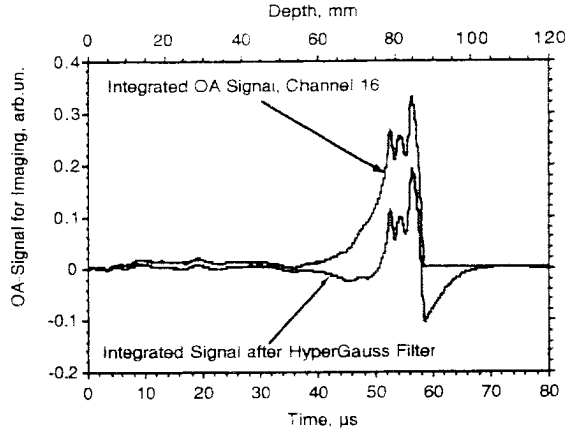


**Figure 5.** Integral of a band-pass-filtered optoacoustic signal starting at the tissue surface and the same integral filtered through a low-pass Gaussian filter in order to eliminate exponential trend associated with effective optical attenuation in tissue and reveal the position and the size of a breast tumor.

### 2.3. Optoacoustic Image Reconstruction

A radial back-projection algorithm, developed for the optoacoustic imaging and described in our earlier publications was employed [10, 20-22]. For the reconstruction of two-dimensional optoacoustic images we used signal integrals shown in Fig 5 and projected them back onto the two-dimensional grid taking into account the directivity pattern (angle of acceptance) of each transducer in the array. The image represents distribution of a product of thermo-acoustic efficiency, optical absorption and absorbed laser energy. The back-projected images acquired with only limited number of detectors display artifacts associated with and image reconstruction using incomplete set of data. The contrast of these images could be improved through the image filtration procedure applied to the entire two-dimensional image [15]. However, unprocessed optoacoustic images contain quantitative information of distribution of absorbed optical energy in tissue. This quantitative information may be used for functional imaging and estimate of tissue optical properties.

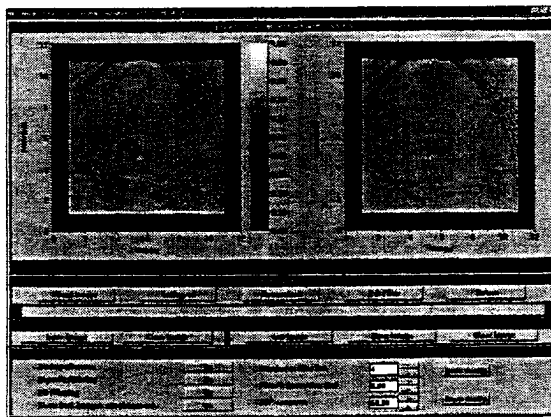


**Figure 6.** LOIS computer interface.

LOIS interface is presented in Fig. 6. Each new image is displayed on the left panel. The right panel allows accumulation and averaging of multiple images. Data acquisition time in LOIS-02 equals 13 seconds for one fiber position. The laser pulse repetition rate is assumed to be 20 Hz and 16 pulses for averaged acquisitions are employed. Data processing and back-projected image formation takes 0.8 seconds. Image filtration and its optimal processing take 0.2 seconds. Total time equals 14 sec. Current design of the laser optoacoustic imaging system (LOIS) allows operator to scan the acoustic detector

array manually through the breast and to obtain images of chosen parts of the breast.

### 3. RESULTS AND DISCUSSION

#### 3.1. Initial Tests of Clinical LOIS

Laser optoacoustic imaging system was tested in various phantoms. As shown in the diagram on Figure 7, the artificial blood vessels were located at different depths and were placed either parallel or perpendicular to the imaging plane. Position of the transducer array was at the bottom of the image (not shown). Surface position is visible as a bright area on the images. A single fiber was used for irradiation at only one location on the surface of the phantom. A photograph of the phantom is presented in Fig. 7 (right). The phantom was imaged twice, one time with optical fiber positioned at one point of its surface and the second time at the opposite position (the phantom was rotated 180 degrees).

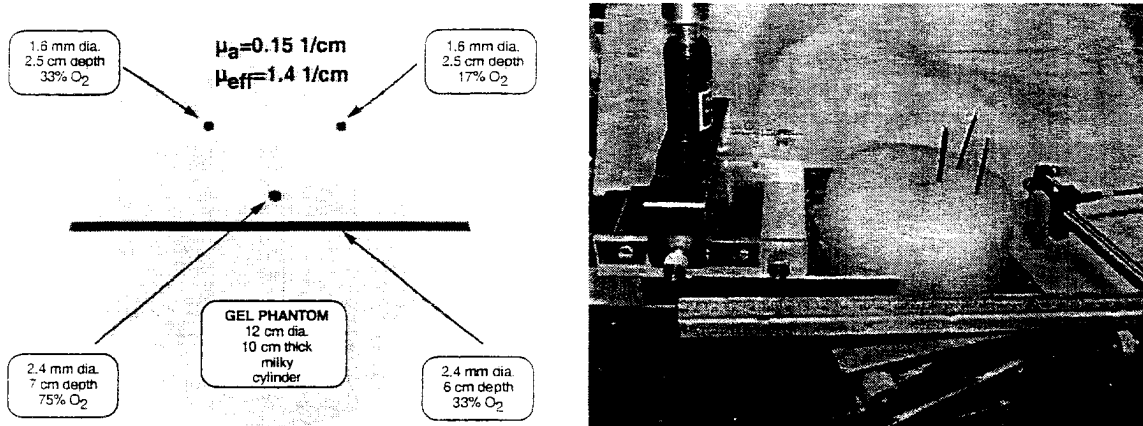


**Figure 7.** Left panel: Collagen gel phantom with artificial blood vessels filled with rabbit blood having various levels of oxygenation. Positions of blood vessels and percent of oxyhemoglobin are shown in windows. Optical properties of this phantom were similar to the optical properties of the breast at the wavelength of 1064 nm. Right panel: Photograph of the same phantom with artificial blood vessels. Transducer array and optical fiber are also presented on the photograph.

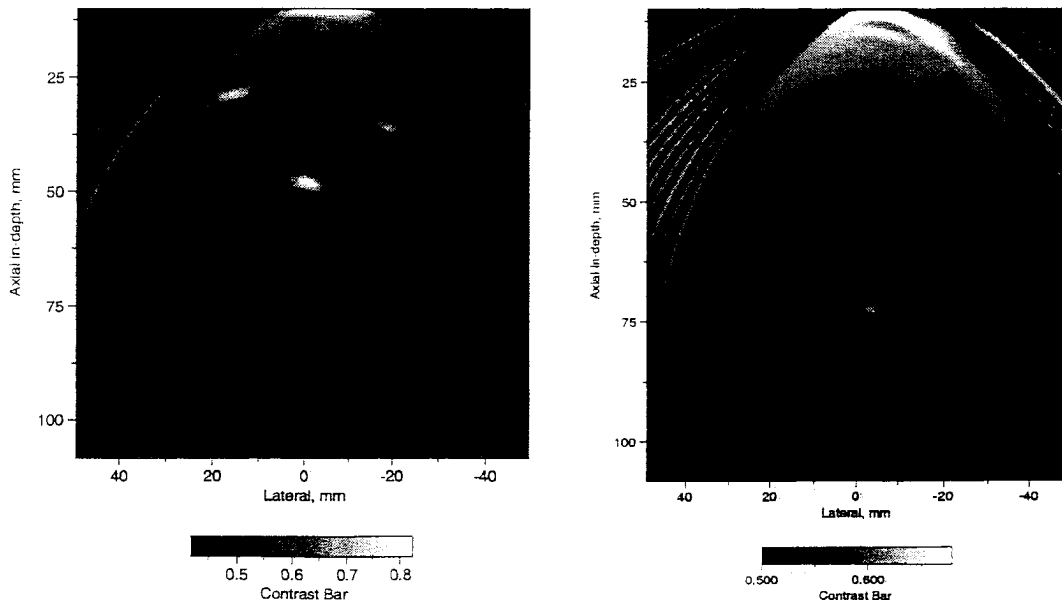


**Figure 8.** Optoacoustic image of blood vessels in milky gelatin phantom. Contrast of blood vessels relative to background is shown on Contrast Bar. Depth from the surface is depicted on the left vertical axis of each image.

Two-dimensional images of blood vessels of different diameter and filled with blood having different level of oxygenation is

shown in Figure 8. Whole milk was diluted by water to obtain the effective optical attenuation coefficient  $1.4 \text{ cm}^{-1}$  in order to mimic the upper limit of optical scattering in the breast tissue at the wavelength of 1064 nm. Optical absorption coefficients of blood in blood vessels varied from 0.8 to 4.0 per cm depending on oxygen content. The first image was reconstructed using optoacoustic signal integrals filtered through a low frequency filter in order to remove the exponential trend associated with effective optical attenuation (Fig. 8 left). The second image was not filtered through a low frequency filter, so that exponential profile of light distribution in the phantom could be observed (Fig. 8, right).

The image of blood vessel cross-sections differs from the correct circular shape. This fact has a simple explanation. As the angle of acceptance of these objects by the transducer array was about  $120^\circ$  only one-third of data needed for complete image reconstruction were collected and employed in image reconstruction. This limited lateral resolution in the far zone of the images presented in Fig. 8. An increase of the acceptance angle for the blood vessel located farther from the irradiation site and closer to the detector array resulted in a better reproduction of its circular cross-section in the image, as clearly depicted in Fig. 8 (right panel) showing an image of a blood vessel in the near zone. The angle of acceptance in this case is about  $180^\circ$  and as a consequence the shape of image highly correlates with real shape of the circle. Note that our image reconstruction algorithm allows accurate reproduction of spherical objects and cylindrical objects (see a blood vessel in the center going in horizontal direction). Thus, we may predict that objects with random shapes will be correctly reproduced on LOIS images. The low frequency filtration procedure demonstrated in Fig. 8 (left panel) yield image with completely eliminated artifacts due to  $1/r$  noise-enhancement near transducers.

All blood vessels were clearly resolved and depicted as separate objects. The relative position of the blood vessels as depicted on the optoacoustic images accurately resembles their position as shown on photograph Fig. 7 (right panel) and their depths are in good agreement with their real location. This imaging experiment demonstrated sensitivity of LOIS sufficient for detection of blood vessels at the depth of over 75 mm in an optical strongly scattering and absorbing phantom. The brightness of the blood vessel images was proportional to the amount of absorbed optical energy, which in turn was proportional to the level of blood oxygenation in each vessel

### 3.2. Quantitative Optoacoustic Imaging

Optoacoustic tomography visualizes the spatial distribution of absorbed optical energy in tissue. However, distortion of optoacoustic signals upon propagation through thick layers of tissue and signal processing may in principle modify the original profile. We tested possibility to obtain axial in depth profiles of absorbed optical energy from optoacoustic images from human muscle tissue. A human arm was imaged in the area of byceps with LOIS designed for breast cancer imaging.

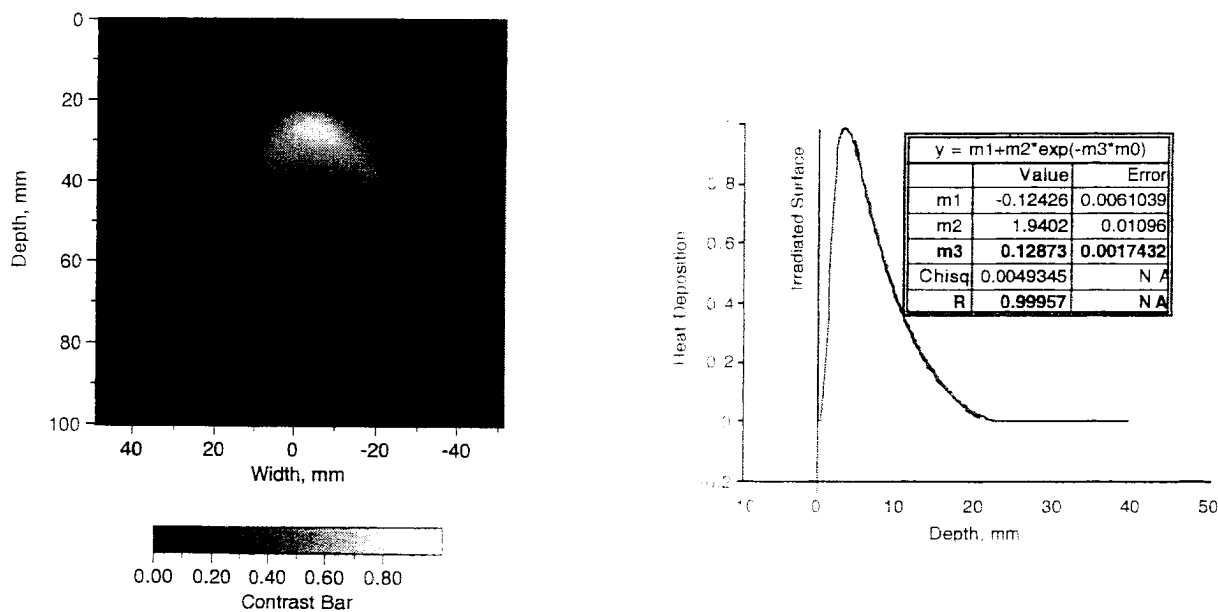


**Figure 9.** Optoacoustic image of human arm in the area of byceps (left panel) and in-depth cross-section of this image resembling the profile of absorbed optical energy (right panel). The effective optical attenuation coefficient,  $\mu_{eff}=1.28 \text{ cm}^{-1}$ .

Only high frequency filtering was applied to the optoacoustic image. This experiments demonstrated that quantitative

information can be obtained from optoacoustic images. Neither signal correction for acoustic diffraction, nor reconstruction of absorbed optical energy distribution from optoacoustic signals, nor correction for sensitivity of individual piezoelectric transducers changed quantitative information. The effective optical attenuation coefficient,  $\mu_{\text{eff}}=1.28 \text{ cm}^{-1}$ , determined from exponential fit of the optoacoustic profile, was in a good agreement with results of direct measurements of optical properties in this tissue.

### 3.2. Imaging Breast Cancer *in vivo*

Eligible patients were chosen from the group of patients scheduled for radical surgical mastectomy with breast cancer diagnosed with x-ray mammography or a combination of x-ray mammography and other imaging modalities (ultrasound, MRI) and biopsy. The patients were imaged in the surgery room before surgery. Two-dimensional optoacoustic images were acquired in several locations on the breast with cancer. Irradiation with 512 pulses from a nanosecond Nd:YAG laser operating at the wavelength of 1064 nm was performed only at one site of breast skin surface. Optoacoustic transducer array was placed on the opposite side of the breast approximately beneath the point of irradiation. Irradiation point was placed approximately above the area suspicious of being a tumor. The exact location of tumors was not known prior to optoacoustic imaging procedure, however, approximate location could be determined from the mammogram. Tumors were sometimes palpable and biopsy incision was visible on the spared segment of skin. However, some tumors were not palpable and located deep within the breast. Two exemplary optoacoustic images of breast carcinoma is presented in Figure 10.

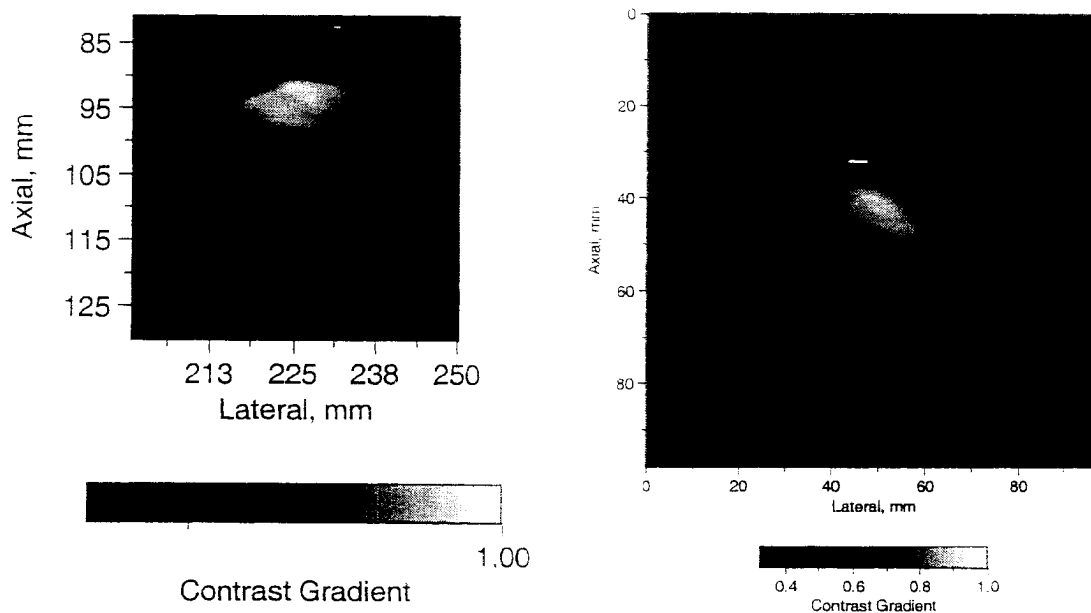


**Figure 10.** Optoacoustic image of a malignant tumor obtained *in vivo* (left, UTMB patient # 315221Q), Optoacoustic image of a malignant tumor obtained *in vivo* (right, UTMB patient # 026372P).

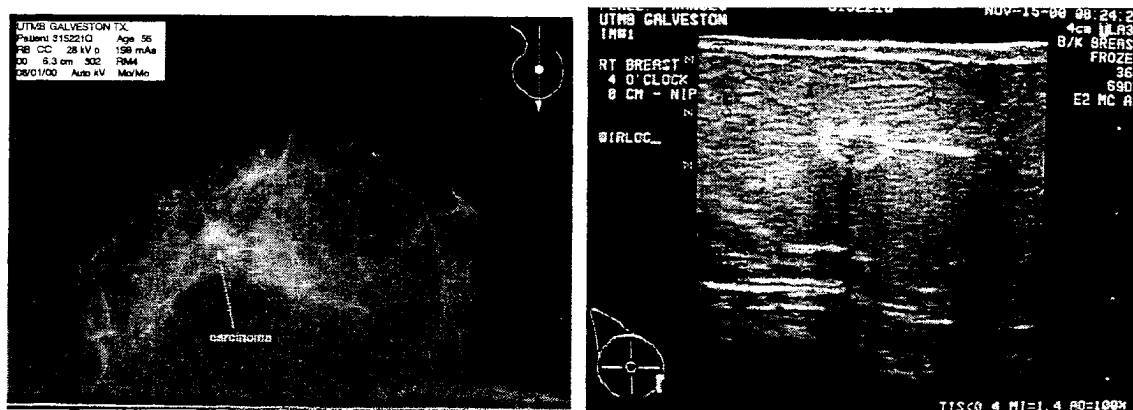


**Figure 11.** X-ray mammography image of a cancerous breast (left). There were 2 suspicious areas on mammogram, only one of them was a ductal carcinoma. Ultrasound image of the same breast showing malignant tumor. UTMB Patient # 315221.

The main conclusion that could be made from clinical experiments on breast cancer patients is that optoacoustic tomography provides enhanced contrast between normal tissues and cancerous tumors. This contrast varies, however, no one tumor of 5 tumors examined had contrast less than 1, i.e. the optoacoustic amplitude is twice higher in tumors relative to normal background. Optoacoustic images presented in Fig. 10 depict details of tumor structure based mainly on optical properties of cancerous tissues. Location of the tumors inside the breast and the tumor dimensions also were accurately determined from the optoacoustic images and confirmed through comparison with x-ray mammography, ultrasound and pathological examination (see Figure 11). Figure 11 presents x-ray mammography and ultrasound images of the breast with a malignant tumor, which was depicted in optoacoustic image in Fig. 10 (left). The position of the tumor relative to the skin surface was better determined from ultrasound image. However, detailed structure of the tumor was better visualized in x-ray mammography image. On the other hand, x-ray image depicted two areas suspicious of being cancerous, and only one area contained malignant tumor (as determined by pathology study). The tumor core brightly displayed in the optoacoustic image was not visible in neither x-ray or ultrasound images, but was confirmed after subsequent pathology examination. The dimension of a tumor core can be estimated as 10x7 mm. Tumor was detected at the depth of 11 mm from the surface. Contrast between the tumor and surrounding normal tissues in this image exceeds 1.2. The contrast in ultrasound image and x-ray mammography image of the same tumor did not exceed 0.1. Resolution of image visualization with LOIS (~ 1-mm) was comparable with that of x-ray mammography and ultrasound. Results of comparison between optoacoustic, ultrasonic and x-ray radiography images for the patient 026372 (see Fig. 10, right) and for the other 3 patients were qualitatively similar.

#### 4. CONCLUSION

The first clinical prototype of the laser optoacoustic system for two-dimensional imaging of the breast *in vivo* was developed and employed for detection of breast cancer in 5 patients. The system employed an array of 32 elements of ultrawide-band PVDF transducers (20kHz-2MHz) shaped as an arc of 120 degrees. The system initially was tested in various phantoms and demonstrated specifications that make it suitable for high-contrast imaging human tissues. Sensitivity of LOIS permits detection of 2-mm blood vessels at the depth of 7.5 cm. In depth resolution equals 0.4 mm, lateral resolution is about 1 mm depending on position of tumor relative to the transducer array. Quantitative information on distribution of absorbed optical energy can be obtained from optoacoustic images. This clinical prototype LOIS is the basis for the next generations of three-dimensional imaging systems to be developed at UTMB in collaboration with LaserSonix Technologies, Inc. (Houston, TX).

#### 5. ACKNOWLEDGMENTS

This work was supported by the National Cancer Institute (grant #R29-CA80221), DOD Breast Cancer Research Program, US Army (grant #DAMD17-99-1-9404) and US Civilian Research and Development Foundation (grant # RP2-2109).

#### 6. REFERENCES

1. A.A. Oraevsky, S.L. Jacques, R.O. Esenaliev, F.K. Tittel: Time-Resolved Optoacoustic Imaging in Layered Biological Tissues", In: "Advances in Optical Imaging and Photon Migration", vol. 21, ed. by R.R. Alfano, Academic Press (1994) pp. 161-165.
2. A.A. Oraevsky, S.L. Jacques, R.O. Esenaliev, F.K. Tittel: Laser based optoacoustic imaging in biological tissues, *Proc. SPIE* 1994; **2134A**: 122-128.
3. R.A. Kruger, P. Liu: Photoacoustic ultrasound: Pulse production and detection in 0.5% Liposyn, *Medical Physics*, 1994; **21**(7): 1179-1184.
4. A.A. Oraevsky, R.O. Esenaliev, S.L. Jacques, S. Thomsen, F.K. Tittel: Lateral and z-axial resolution in laser optoacoustic imaging with ultrasonic transducers, *Proc. SPIE* 1995; **2389**: 198-208.
5. RA Kruger: Photoacoustic ultrasound, *Med. Phys.* 1994; **21**(1): 127-131
6. A.A. Oraevsky: Laser optoacoustic imaging for cancer diagnosis, *LEOS NewsLetter* 1996; **10**(6): 17-20.
7. A.A. Oraevsky, R.O. Esenaliev, S.L. Jacques, F.K. Tittel: Laser Opto-Acoustic Tomography for medical diagnostics: principles, *Proc. SPIE* 1996; **2676**: 22-31.
8. A.A. Oraevsky, R.O. Esenaliev, S.L. Jacques, F.K. Tittel, D. Medina: "Breast Cancer Diagnostics by Laser Optoacoustic Tomography", In: "Trends in Optics and Photonics", vol. II, ed. by R.R. Alfano and J.G. Fujimoto, OSA Publishing House, pp. 316-321 (1996).
9. A.A. Oraevsky, R.O. Esenaliev, S.L. Jacques, S. Thomsen, F.K. Tittel: Lateral and z-axial resolution in laser optoacoustic imaging with ultrasonic transducers, *Proc. SPIE* 1995; **2389**: 198-208.

10. A.A. Oraevsky, V.G. Andreev, A.A. Karabutov, R.O. Esenaliev: Two-dimensional optoacoustic tomography: array transducers and image reconstruction algorithm, *Proc. SPIE* **3601**: 256-267 (1999).
11. R.O. Esenaliev, A.A. Karabutov, A.A. Oraevsky: Sensitivity of laser opto-acoustic imaging in detection of small deeply embedded tumors, *IEEE J. ST Quant. Electr.* 1999; **5**(4):981-988.
12. A.A. Oraevsky, A.A. Karabutov, V.G. Andreev, R.O. Esenaliev: Laser opto-acoustic imaging of the breast: Detection of cancer angiogenesis, *Proc. SPIE* **3597**: 352-363 (1999).
13. A.A. Karabutov, N.B. Podymova, V.S. Letokhov: Time-resolved laser optoacoustic tomography of inhomogeneous media, *Appl. Phys.* **B 63**, pp. 545-563, 1996.
14. A.A. Oraevsky, R.O. Esenaliev, A.A. Karabutov: Laser optoacoustic tomography of layered tissues: signal processing, *Proc. SPIE* 1997; **2979**: 59-70.
15. V.A. Andreev, A.A. Karabutov, V.S. Solomatin, E.V. Savateeva, V.A. Aleynikov, Y.V. Julina, D.R. Fleming, A.A. Oraevsky: Optoacoustic Tomography of tumors in the breast, *Proc. SPIE* 2000; 3916: 36-47.
16. R.O. Esenaliev, F.K. Tittel, S.L. Thomsen, B. Fornage, C. Stelling, A.A. Karabutov, and A.A. Oraevsky: Laser optoacoustic imaging for breast cancer diagnostics: Limit of detection and comparison with X-ray and ultrasound imaging, *Proc. SPIE* 1997; **2979**: 71-82.
17. N. Weidner, J.P. Semple, W.R. Welch, and J. Folkman: Tumor angiogenesis and metastasis - correlation in invasive breast carcinoma, *New Engl. J. Med.*, 324, pp. 1-7, 1991.
18. A.A. Karabutov, A.A. Oraevsky: Ultimate sensitivity of wide-band detection for laser-induced ultrasonic transients, *Proc. SPIE* 2000; 3916: 228-239.
19. N.Ghosh, S.K. Mohanty, S.K. Majumder, P.K. Gupta: Measurement of optical transport properties of normal and malignant human breast tissue, *Appl. Optics* 2001; 40(1): 176-184.
20. G.S. Kino: "Acoustic waves. Devices, imaging, and analog signal processing", Prentice-Hall, Englewood Cliffs, 1987.
21. P. Liu: Image reconstruction from photoacoustic pressure signals. *Proc. SPIE* **2681**: 285 - 296 (1999).
22. K.C. Ternovoy, M.V. Sinkov: "Introduction to modern tomography", Naukova Dumka, Kyiv, Ukraine (1996).

# Inverse Radon Transform for Optoacoustic Imaging

Valeriy G. Andreev<sup>1</sup>, Dmitriy A. Popov<sup>1</sup>, Dmitriy V. Sushko<sup>1</sup>,  
Alexander A. Karabutov<sup>2</sup>, Alexander A. Oraevsky<sup>2</sup>

<sup>1</sup>M.V.Lomonosov Moscow State University, Moscow 119899, RUSSIA,

<sup>2</sup>University of Texas Medical Branch at Galveston, Texas, 77555 USA

## ABSTRACT

Mathematical model of image reconstruction for two-dimensional optoacoustic imaging system is described. It was assumed that (1) receiving transducers are uniformly distributed along the perimeter of a 60-mm radius ring with 2.1-mm gaps between transducer centers and (2) initial data were known with 0.1-mm increments. The algorithm of radial back projection with convolution was used for optoacoustic image reconstruction. The convolution was evaluated with modified Shepp-Logan (MSL) and rectangular (RECT) space spectrum windows. Linear interpolation was applied for calculation of the convolution at the intermediate space points. The following four criteria were employed for estimation of resulting image quality: (1) noise level on entire tomogram, (2) a jump transfer function, (3) loss contrast function and (4) the contrast-dimension relation. Theoretical expressions for these parameters were derived and used for optimization of the proposed algorithm. Two-dimensional images of computer simulated spherical objects were reconstructed. It was shown that 0.1-mm spatial resolution could be obtained provided the signal-to-noise ratio equals approximately 3 at the tomogram. A very small (0.2-mm diameter) tumor and a small (2-mm diameter) tumor could be clearly revealed at the tomogram if their optical absorption contrast equals at least 2 and 0.1 respectively.

**Keywords:** image reconstruction, tomography, filtered backprojection algorithm, image quality criteria

## 1. INTRODUCTION

A clinical prototype of the laser optoacoustic imaging system (LOIS) with 32-arc transducer array was successfully tested in mastectomy samples and in vivo studies [1,2]. Pronounced optoacoustic contrast of 1.2-to 3.5 was demonstrated. Design of the acoustic array allows operator to scan through the breast manually and obtain images of chosen parts of the breast in real time. The main drawback of this system is a limited viewing angle ( $120^\circ$ ), which resulted in insufficient lateral resolution. A new optoacoustic tomography system designed for stationary investigation is under development in UTMB now. It employs acoustic array with 180 transducers uniformly distributed along the surface of hollow cylinder. A breast is placed inside cylinder filled with degassed and deionized water. It is illuminated by laser pulses delivered through optical fibers located in gaps between acoustic transducers. A complete set of data for high quality image reconstruction can be collected in this configuration. A purpose of this work was to develop an algorithm and software code for the breast cancer image reconstruction optimized for the system with cylindrical transducer array consisting of rings with evenly spread piezoelectric detectors.

## 2. METHODS

Let  $\vec{r}$  to be a radius -vector of one of transducers in array. The temporal integral of acoustic pressure detected by transducer at the time  $t$  can be expressed as the superposition of waves radiated by optoacoustic sources located on the spherical surface  $\Sigma$  of radius equaled to time of sound propagation  $c_s t$  [1]:

$$u(\vec{r}, t) = \frac{\beta}{4\pi C_p c_s t} \iint_{\Sigma} Q(\vec{r} + c_s t \vec{n}) d\Sigma \quad (1)$$

where  $\beta$  is the thermal coefficient of volume expansion of the tissue;  $C_p$  is the specific thermal capacity. Function  $Q(r') = \mu_a(r')F(r')$  is the product of light absorption coefficient,  $\mu_a$  and laser fluence  $F$  in the area where optoacoustic sources are distributed. Equation (1) is of general character and it can be considered as the fundamental imaging equation for optoacoustic tomography.

## 2.1. Two-dimensional solution

In 2-dimensional case equation (1) can be written in the following form:

$$u(\alpha, r) = \int_{\Gamma(\alpha, r)} f ds, \quad (2)$$

where  $\Gamma(\alpha, r)$  is the arc of radius  $r$  with origin in the center of receiving transducer with coordinates  $(\cos \alpha, \sin \alpha)$ . We supposed here without loss of generality that transducers are placed on the cylindrical surface with unity radius. Eq. (2) presents a general problem of integral geometry of function reconstruction from a set of its integrals along curves. A common approach to solution of this problem described in [3,4] allows reducing of eq. (2) to the set of simultaneous equations of Volterra type with weak singularity kernel.

To define these equations we introduce cylindrical coordinates  $(p, \theta)$ :  $x = p \cos \theta, y = \sin \theta$  and variable  $\rho = 1 - r$ . Let  $v(\alpha, \rho) = u(\alpha, 1 - r)$  then following [4] one can receive a set of equations:

$$v_k(\rho) = 2 \int_{\rho}^1 h(p, \rho) T_{|k|} \left( \frac{p^2 + 2\rho - \rho^2}{2p} \right) f_k(p) dp, \quad (3)$$

where  $v_k(\rho)$ ,  $f_k(p)$  are the Fourier coefficients of corresponding functions  $v(\alpha, \rho)$ ,  $f(p, \theta)$ :

$$v_k(\rho) = \frac{1}{2\pi} \int_0^{2\pi} e^{-ik\alpha} v(\alpha, \rho) d\alpha, \quad f_k(p) = \frac{1}{2\pi} \int_0^{2\pi} e^{-ik\theta} f(p, \theta) d\theta.$$

Function  $T_k(x)$  is the Chebyshev polynomial of the first type. Function  $h(p, \rho)$  is expressed as:

$$h(p, \rho) = \left[ 1 + \frac{(p^2 - 2\rho + \rho^2)^2}{4p^2 - (p^2 + 2\rho - \rho^2)^2} \right]^{1/2}. \quad \text{It has a singularity provided that } \rho \rightarrow p.$$

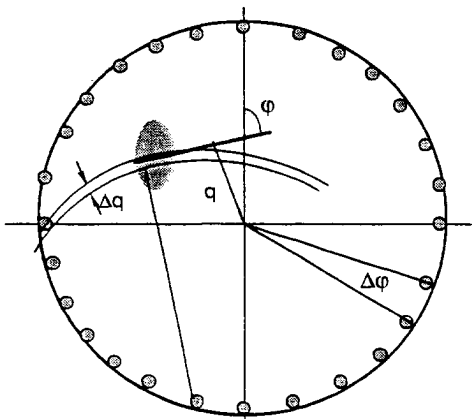


**Figure 1.** Reduction to the problem of Radon transform.

As a result the problem is reduced to classical Radon problem. A filtered backprojection algorithm is employed for image reconstruction in the area of interest with sufficient resolution.

Development of algorithm of the spatial distribution of optoacoustic sources reconstruction completely based on the exact solution of equations (3) has serious mathematical difficulties. In general we have to solve an infinite set of equations each of them has a singularity. We have tested several methods of numerical solution of eqs. (3), but all of them resulted in algorithms of high complexity and weak convergence. These algorithms could not provide a function reconstruction with necessary precision.

We propose to use an iterative approach for the solution of the inverse problem. At the first step limited number of equations (3) are solved in whole area and this solution provides an image with low resolution. Nevertheless this approximate solution can be used for localization of area containing suspicious object. At the second step integrals inside area of interest are calculated as difference between measured data (2) and integrals of function defined at the first step over part of arcs outside of area of interest. At the third step we suppose that area of interest is small compared to the entire object. It allows substituting of the integrals along arcs by integrals along straight lines that tangent to corresponding arc curves.

## 2.2. Filtered backprojection algorithm

In this study we proposed that location of area of interest and integrals of desired function along straight lines are already known. Therefore ultimate quality of reconstructed images can be evaluated when filtered backprojection algorithm is employed.

From mathematical point of view the following integrals along lines  $x \cos \varphi + y \sin \varphi = q$  defined in canonical coordinates  $(q, \varphi)$  are known:

$$u(\varphi, q) = \int_{-\infty}^{+\infty} f(q \cos \varphi + \xi \sin \varphi, q \sin \varphi - \xi \cos \varphi) d\xi. \quad (4)$$

A lot of approaches are supposed for the solution of this problem [5-7]. Most of practical tomography systems employ convolution and backprojection algorithms that are based on the projection theorem:

$$\hat{u}(\varphi, \lambda) = \hat{f}(\lambda \cos \varphi, \lambda \sin \varphi), \quad (5)$$

where  $\hat{u}$  denotes the Fourier transform of the function  $u$  on independent variable  $q$   $\hat{u}(\varphi, \lambda) = \int_{-\infty}^{+\infty} e^{i\lambda q} u(\varphi, q) dq$ .

Two-dimensional Fourier transform of desired function  $u$  calculated in polar coordinates ( $\lambda_1 = \lambda \cos \varphi$ ,  $\lambda_2 = \lambda \sin \varphi$ ) is on the right side of eq. (5). To get inversion formula for the desired function  $f$  one has to calculate two-dimensional inverse Fourier transform:

$$f(x, y) = \frac{1}{4\pi^2} \int_0^{2\pi} d\varphi \int_{-\infty}^{+\infty} e^{-i\lambda(x \cos \varphi + y \sin \varphi)} |\lambda| d\lambda \int_{-\infty}^{+\infty} e^{i\lambda q} u(\varphi, q) dq. \quad (6)$$

General theory of convolution and backprojection algorithms has been extensively developed [5,8,9].

Let  $u_{kj} = u(\varphi_k, q_j)$  is the initial integral defined on the line with coordinates  $(\varphi_k, q_j)$ . By definition, coordinates  $\varphi_k$  and  $q_j$  are given by following relations:

$$\begin{aligned} \varphi_k &= k \Delta\varphi, & k &= 0, 1, \dots, (N_\varphi - 1), & \Delta\varphi &= \frac{\pi}{N_\varphi}, \\ q_j &= j \Delta q, & j &= 0, \pm 1, \pm 2, \dots, N_q \end{aligned} \quad (7)$$

where  $\Delta q$  is the discretization step in radial direction,  $\Delta\varphi$  is the angular distance between two neighboring transducers (see Fig. 1). The cycle condition  $u_{j2N_\varphi} = u_{j0}$  is satisfied. Value of  $\Delta q$  can be evaluated from time sampling interval  $\Delta t$  of the analog-digital converter employed in the tomography system:  $\Delta q = c_s \Delta t$  ( $c_s$  is the speed of sound in the tissue).

The phenomenological model of measurement procedure, in particular the inaccuracy of ultrasonic detectors can be taken into account by introducing apparatus function  $\Pi(q)$ :

$$u^\Pi(\varphi_k, q_j) = \int_{-\infty}^{+\infty} \Pi(q_j - q') u(\varphi_k, q') dq'. \quad (8)$$

Algorithm based on the inversion formula (6) consists of two steps. Function  $\psi^A(\varphi_k, a)$  is computed as a convolution of measured data with a kernel  $H^A(s)$ , and function  $f$  is resulted as sum of  $\psi^A(\varphi_k, a)$  over entire angles:

$$\psi^A(\varphi_k, a) = \sum_j H^A(a - q_j) u^\Pi(\varphi_k, q_j) \Delta q \quad (9)$$

$$f^A(x, y) = \sum_{k=0}^{N_f-1} \psi^A(\varphi_k, x \cos \varphi_k + y \sin \varphi_k) \Delta \varphi$$

Kernel  $H^A(s)$  depends on the effective regularizer  $R^A(\lambda)$ :

$$H^A(s) = \frac{1}{2\pi^2} \int_0^\infty \lambda R^A(\lambda) \cos \lambda s \, d\lambda \quad (10)$$

where  $\lambda$  is a spatial frequency. A specific form of effective regularizer in turn is defined by regularizer  $R(\lambda)$  and algorithm of data interpolation employed. We restricted ourselves to algorithms with linear interpolation procedure, which can be described in the following way. Let introduce regularizer as a function, which satisfies the conditions:

$$R(0) = 1; \quad R(\lambda) = R(-\lambda); \quad R(\lambda) = 0 \quad \text{if} \quad |\lambda| > \Omega, \quad (11)$$

where  $\Omega = \frac{\pi}{\Delta q}$  is the Nyquist frequency. A kernel corresponding to the regularizer is calculated:

$$H_R(s) = \frac{1}{2\pi^2} \int_0^\infty \lambda R(\lambda) \cos \lambda s \, d\lambda.$$

It allows calculating of the function  $\psi_R(\varphi_k, n\Delta q)$  at sampling points:

$$\psi_R(\varphi_k, n\Delta q) = \sum_j H_R(n\Delta q - j\Delta q) u^\Pi(\varphi_k, q_j) \Delta q \quad (12)$$

Function  $\psi$  in the intermediate points is computed by using a linear data interpolation. Effective regularizer satisfying this procedure has a following form:

$$R^A(\lambda) = \frac{1}{|\lambda|} \left( \frac{\sin \frac{\lambda \Delta q}{2}}{\frac{\lambda \Delta q}{2}} \right)^2 \sum_{n=-\infty}^{+\infty} |\lambda + 2n\Omega| R(\lambda + 2n\Omega) \quad (13)$$

We used modified Shepp-Logan (MSL)  $R_1(\lambda)$  and rectangular (RECT)  $R_2(\lambda)$  spectral windows:

$$R_1(\lambda) = \begin{cases} \left( \frac{\lambda \Delta q}{2} \right)^{-1} \sin \frac{\lambda \Delta q}{2}, & |\lambda| \leq \Omega; \\ 0, & |\lambda| > \Omega; \end{cases} \quad R_2(\lambda) = \begin{cases} 1, & |\lambda| \leq \Omega; \\ 0, & |\lambda| > \Omega. \end{cases} \quad (14)$$

Rectangular window provides the flat spectral characteristic up to Nyquist frequency, MSL window reduces the contribution of high frequencies.

For the simplicity we will assume that apparatus function is characterized by uniform sensitivity and can be expressed in the form:

$$\Pi(q) = \begin{cases} 1, & |q| \leq \frac{\Delta q}{2}; \\ 0, & |q| > \frac{\Delta q}{2}. \end{cases} \quad (15)$$

### 3. RESULTS

In this section results of the numerical experiments will be described. Numerical simulations were performed with computer code developed on the base of mathematical model of two-dimensional optoacoustic tomography system (MMT). The basic MMT includes: (1) method of object definition – function  $f$ ; (2) algorithm of initial data generation – function  $u^\Pi(\varphi_k, q_j)$  and noise  $\Delta_{jk}$ ; (3) algorithm of reconstruction – filtered backprojection and (4) algorithm of image quality estimation.

To perform computer simulation of image reconstruction we have to specify the parameters of the optoacoustic tomography system. We assume that a diameter of the ring there acoustic transducer are located is 120 mm, number of transducers is 180, therefore the angular discretization parameter  $\Delta\varphi = 2^\circ$ . Image reconstruction with the step of discretization in the radial direction  $\Delta q=0.1$  mm is referred to the variant 1. In variants 2 and 3 the calculations were performed with steps  $\Delta q=0.3$  mm and  $\Delta q=0.5$  mm. Initial data averaged on the corresponding intervals were employed for image reconstruction with enlarged steps:

$$u^\Pi(\varphi_k, j\Delta q_{m+1}) = \frac{1}{2m+1} \sum_{\alpha=j-m}^{j+m} u^\Pi(\varphi_k, \alpha\Delta q_1) \quad (m = 1, 2). \quad (16)$$

We consider reconstructed object to be a homogeneous disk of radius 5 mm with characteristic function:

$$f(x, y) = f_0(x, y) = \begin{cases} 1 & , (x, y) \in D_0; \\ 0 & , (x, y) \in D_0^c, \end{cases} \quad (17)$$

In this case maximum initial signal can be estimated as 10mm. We consider the noise to be one-tenth of a maximum signal:  $\sigma(u) = 10^{-1} \max u^\Pi(\varphi, q) \approx 1.0$  mm.

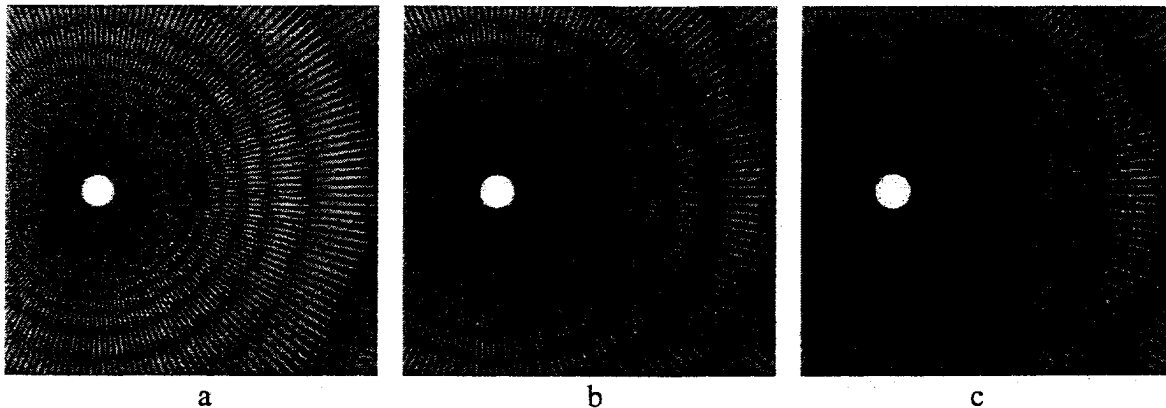


**Figure 2.** Image of the homogeneous disk of 5 mm radius without noise. The 256-grade gray scale lies in the range  $(-0.1 - 0.1)$ . a -  $\Delta q=0.1$  mm; b -  $\Delta q=0.3$  mm; c -  $\Delta q=0.5$  mm.

Images of the homogeneous disk with center at  $(-30, 0)$  are presented in Fig.2 and Fig.3. Initial data without noise (Fig.2) and with noise (Fig.3) were used for the image reconstruction. Calculations were performed for three variants corresponding to different steps of discretization in radial direction  $\Delta q$  in the square with 60-mm side. MSL spectrum window was employed.

The tomograms presented in Fig. 2 allows to estimate the artifacts level for tree variants of reconstruction. By artifact one usually mean different kinds of systematic reconstruction errors. Unlike noise, artifacts demonstrate a clear well-ordered geometric structure that depends on the nature of systematic errors. The artifacts presented in Fig. 2 are the result of discretization errors. Their ray-like structure is defined by the significant difference in the numbers of angular and spatial samples. Artifact level can be estimated as a ratio of maximum deviation on the tomogram outside of the disk image to the mean value inside disk. We received the following values: variant V1 ( $\Delta q=0.1$  mm) – 10%, V2 ( $\Delta q=0.3$  mm) – 4.4%, V3 ( $\Delta q=0.5$  mm) – 2.7%.

In practical tomography the discretization artifact levels are small and dominated by noise and other errors. It is clearly demonstrated in Fig.3 where the image of the same object in the presence of noise is shown. Noise level is three times higher than artifacts, but in somewhere the regular structure is slightly appeared. Noise level can be defined as mean square deviation on the tomogram calculated in the region sufficiently far from the object. The noise levels determined for three variants of image reconstruction are presented in Table1:

Table 1. Parameters of the filters.

	V1	V2	V3
MSL	0.304	0.058	0.027
RECT	0.657	0.126	0.059

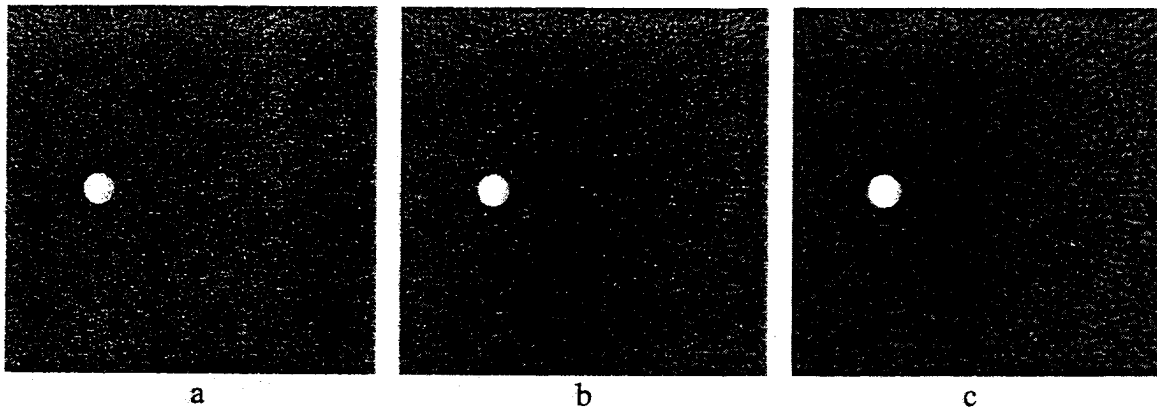


Figure 3. Image of the homogeneous disk of 5 mm radius with noise. The 256-grade gray scale lies in the range  $(-0.3 - 0.3)$ . a -  $\Delta q=0.1$  mm; b -  $\Delta q=0.3$  mm; c -  $\Delta q=0.5$  mm.

Noise level is significantly reduced then averaging is applied, the tomogram becomes smoother. But in the same time sharpness of the object edges is also reduced, and the spatial resolution decreases. To demonstrate the special resolution provided by the filtered backprojection algorithm the images of two disks separated by a small gap were reconstructed. Calculations were performed with noisy initial data and MSL spectral window was employed. Results are shown in Fig.4. The 0.1 mm gap is clearly resolved only on the tomogram calculated with step  $\Delta q=0.1$  mm, but this tomogram is noisy one. Calculations with variants 2 and 3 provide more smooth tomogram but with low resolution. The 0.3 mm gap is resolved on entire tomograms.

#### 4. DISCUSSION

The main problem discussed in this section is the choice of quantitative parameters describing the quality of homographic images. In practice, this problem is solved by choosing several basic quality criteria and describing the corresponding measurement methods. We will use following quality criteria: (1) noise level on the tomogram, (2) jump transfer function, (3) loss contrast function and (4) contrast-dimension curve. These criteria allow us to optimize the reconstruction algorithm and compare the quality of images obtained in various tomography systems. General theory developed in [9] provides theoretical estimations of the main parameters of reconstruction quality. We will adapt them for optoacoustic tomography system and compare theoretical estimations with results of numerical simulation.

Noise level on the tomogram can be estimated as

$$\sigma^2(f^A) \approx \frac{\sigma^2(u) \Delta\varphi \Delta q}{4\pi^2} \int_0^\infty \lambda^2 R^A(\lambda)^2 d\lambda \quad (18)$$

where  $\sigma(u)$  is the mean square deviation of the initial data noise and  $R^A(\lambda)$  is the effective regularizer. For the algorithm we used in our calculation this formula can be simplified:

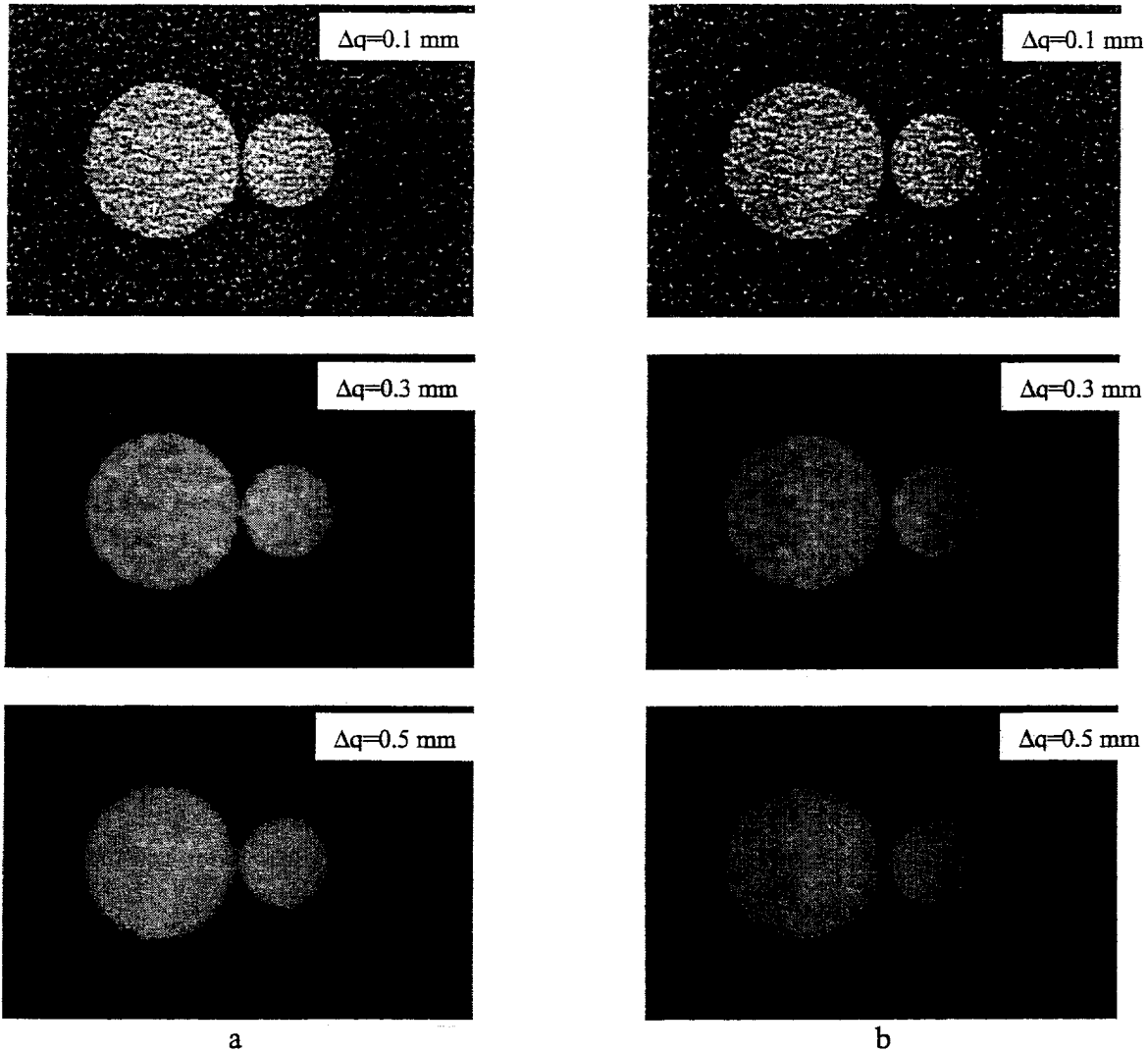


**Figure 4.** Images of two disks of radii 5 mm and 3 mm with a small gap between them. The gap value is 0.1 mm (a) and 0.3 mm (b). The 256-grade gray scale lies in the range  $(-0.5 - 1.5)$ .

$$\sigma^2(f^A) \approx \sigma^2(u) \frac{\Delta\varphi}{\Delta q^2} c_\sigma(A) , \quad (19)$$

where constant value  $c_\sigma(A)$  depends on spectrum window:

$$c_{\sigma}(A) = \begin{cases} 1/12\pi \approx 0.02658 & , \quad R = R_1; \\ \pi/18 - 1/6\pi \approx 0.121481 & , \quad R = R_2. \end{cases} \quad (20)$$

In particular, for the case when steps of discretization  $\Delta\varphi = 2^0$  and  $\Delta q = 0.1$  mm (variant V1), spectral window R1 and initial data with noise  $\sigma(u) = 0.1$  cm, formula (15) give the 30%-noise on the tomogram. This value corresponds well to results of our numerical simulations presented in Table 1.

A jump transfer function (JTF) can be used as a measure of spatial resolution on the resulted image. The JTF characterizes the smoothing of discontinuity of object edges on the tomogram. To define JTF one has to restore the characteristic function of the disk with radius  $b \gg \Delta q$  provided  $f^A = 1$  in center part of the disk. Let the disk center has coordinates  $(a_x, a_y)$ , then reconstruction of function  $f^A(n\Delta x, a_y)$  with the small step  $\Delta x \ll \Delta q$  results in JTF:  $P^A(x) = f^A(x + a_x + b, a_y)$   $x > 0$ . Theoretical estimation provides the following formula for JTF:

$$P^A(x) \approx \frac{1}{2} - \frac{1}{\pi} \int_0^{\infty} \hat{\Pi}(\lambda) R^A(\lambda) \frac{\sin \lambda x}{\lambda} d\lambda, \quad (21)$$

where  $\hat{\Pi}(\lambda)$  is the Fourier transform of apparatus function.

Figure 5 shows jump transfer functions corresponding to MSL spectral window (three upper curves) and RECT window

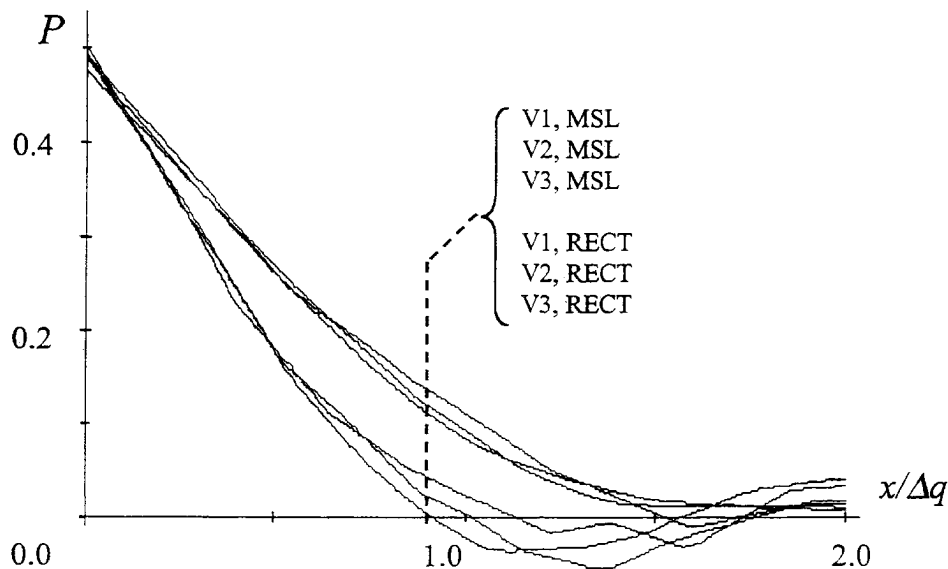
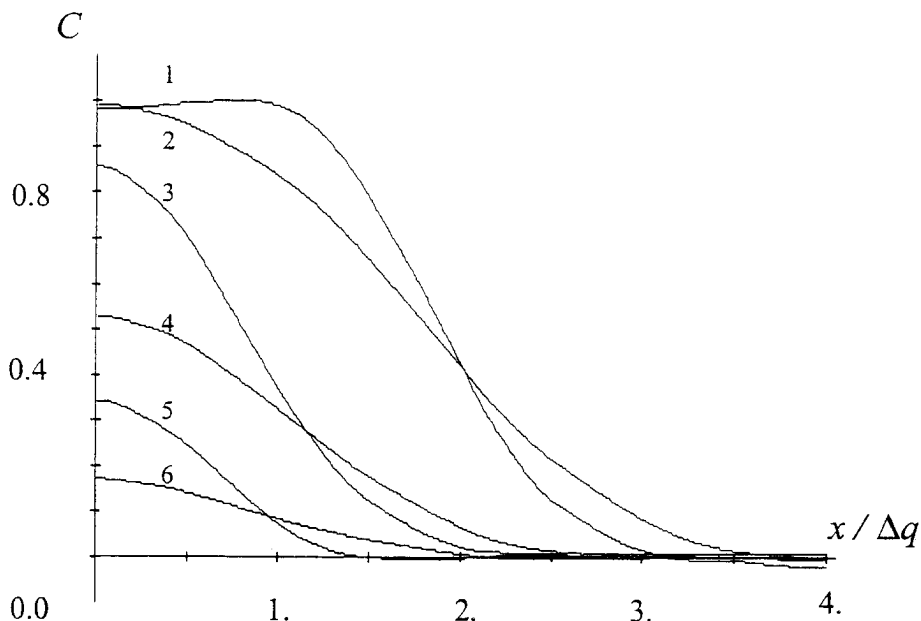


Figure 5. Jump transfer function.

(three lower curves). These data were resulted from reconstruction of the characteristic function of the disk with radius 5 mm without noise. Calculations were performed along X-axis in the range  $[-25.0, -25.0 + 2\Delta q_i]$  with step  $\Delta x = \Delta q_i / 200$  ( $i=1,2,3$  correspond to variant of reconstruction). Rectangular window provides more sharp edge of image; at  $x=0$  as it follows from formula (16) these curves have the same value equaled to 0.5.

Contrast loss function can be evaluated from the reconstruction of the small disks. Fig.6 represents tomogram profiles along x-axis obtained in exactly the same way as a jump transfer function, but with disks of different radii:  $b=2\Delta q=0.2$  mm,  $b=\Delta q$ ,  $b=\Delta q/2$  and with the x-variable representing the distance from the center of the disk. Disk center was at the point  $(-30.0, 0)$ .



**Figure 6.** Images of small disks. Curves correspond to the following parameters: 1 -  $b=0.2$  mm, V1, RECT; 2 -  $b=0.2$  mm, V1, MSL; 3 -  $b=0.1$  mm, V2, RECT; 4 -  $b=0.1$  mm, V2, MSL; 5 -  $b=0.05$  mm, V3, RECT; 6 -  $b=0.05$  mm, V3, MSL.

The even curves were reconstructed with MSL window; they are flatter than corresponding curves reconstructed with RECT window. Contrast  $C$  in the disk image center is reduced with radius decreasing. We used the contrast definition as excess of function over background related to the background itself:  $C = \frac{f^A - \sigma}{\sigma} = \frac{f^A}{\sigma} - 1$ . Dependence of contrast in the center of a small object on its dimension is described by the contrast loss function  $C^A(b)$ . Theory provides the following estimation for the contrast loss function in the case of small disk with radius  $b$  [9]:

$$C^A(b) \approx b \int_0^{\infty} \hat{\Pi}(\lambda) R^A(\lambda) J_1(\lambda b) d\lambda, \quad (22)$$

where  $J_1(\lambda b)$  is Bessel function of the 1-st order. Fig.7 shows the contrast loss function calculated for variants V1-V3 with MSL window.

The contrast-dimension function  $CD^A(b)$  is defined from the relation:

$$CD^A(b) \cdot C^A(b) = \gamma \sigma(f^A) \quad (23)$$

where  $\sigma$  is the noise level on the tomogram,  $\gamma$  is a given number called as the detection level. As follows from this definition the  $CD^A(b)$  is the contrast value such that the corresponding signal is  $\gamma$  times more than the noise level.

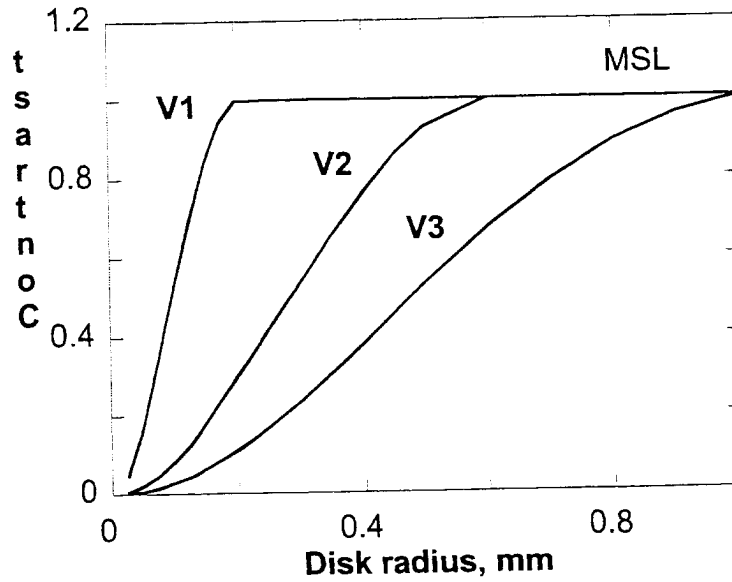


Figure 7. Contrast loss function.

Usually the detection level is chosen as 3. Contrast-dimension curve divides the plot surface on two parts: area of visible contrasts (upper the curve) and invisible ones (below the curve). Contrast-dimension function is a universal characteristic of any tomography system. It can be employed for X-ray, MRI, Ultrasound systems for their performance comparison. Fig. 8 shows that inclusion of 0.2 mm radius can be revealed on the tomogram provided its contrast is 1 or higher. For smaller objects (0.1 mm, for example) the contrast should be 3 and higher.

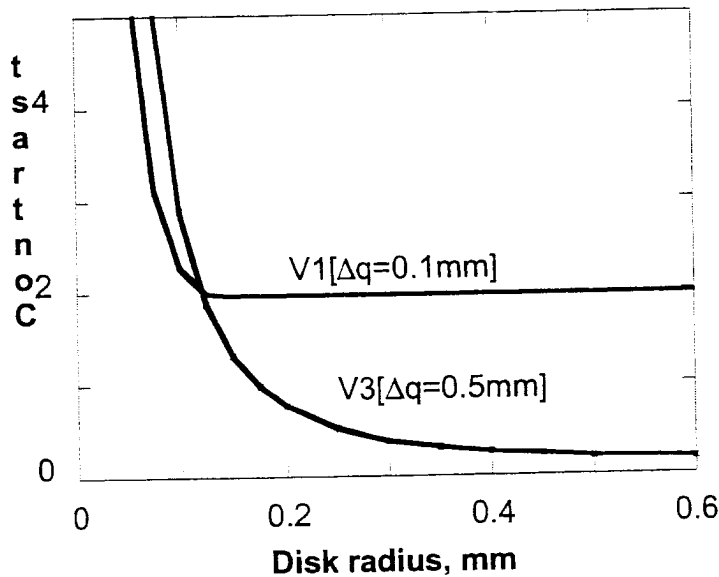


Figure 8. Contrast-dimension function when rectangular spectrum window was used.

It is necessary to emphasize that the functions  $P^A(x), C^A(b)$  characterizing the spatial resolution depends on only ratios  $x/\Delta q, R/\Delta q$ . Therefore the expressions (17), (18) derived for these functions have a universal character, if all dimensions are normalized by discretization step  $\Delta q$ . It allows us to employ results of [9] and this work for optoacoustic systems of various configurations.

## 5. CONCLUSION

This work is the first step for a development of mathematical model of image reconstruction for a two-dimensional optoacoustic imaging system with cylindrical transducer array. We considered only one stage of this model namely filtered backprojection algorithm in assumption that integrals along straight lines are known. We are planning to generalize this algorithm to the case of integrals along arcs. It will allow us to reconstruct images of the inclusions located in the transducers vicinity.

## 6. ACKNOWLEDGMENTS

This work was supported by the National Cancer Institute (grant #R29-CA80221), DOD Breast Cancer Research Program, US Army (grant #DAMD17-99-1-9404) and US Civilian Research and Development Foundation (grant # RP2-2109).

## 7. REFERENCES

1. V.G.Andreev, A.A.Karabutov, S.V.Solomatin, E.V.Savateeva, V.L.Aleynikov, Y.V.Zhulina, R.D. Fleming, A.A. A.A. Oraevsky. Opto-acoustic tomography of breast cancer with arc-array-transducer, *Proc. SPIE* **3916**: 36-47 (2000).
2. A.A.Oraevsky, V.G.Andreev, A.A.Karabutov, S.V.Solomatin, E.V.Savateeva, R.D. Fleming. Laser optoacoustic imaging of breast cancer in vivo, *Proc. SPIE* **4256-02** (2001).
3. M.M.Lavrentiev, V.G.Romanov, V.G.Vasiliev: "Multidimensional inverse problems for differential equations", Novosibirsk, Nauka, 1969.
4. V.G.Romanov: "Some inverse problems for the equations of hyperbolic type", Novosibirsk, Nauka, 1972.
5. F. Natterer: "Mathematics of Computerized Tomography", John Wiley & Sons, 1986.
6. S.R.Deans: "The Radon Transform and Some of its Applications", John Wiley & Sons, 1983.
7. S. Helgason: "The Radon Transform", Birkhäuser, 1980.
8. D.A.Popov. Reconstruction of characteristic functions in two-dimensional Radon tomography. *Uspekhi Mat. Nauk*, v.53 (1998), no.1, 116-198. English translation in *Russian Math. Surveys*, v.53 (1998).
9. D.A.Popov, E.B.Sokolova, D.V.Sushko. Mathematical Models in Two-Dimensional Radon Tomography. In *Applied Problems of Radon Transform*. Providence, RI: Amer. Math. Soc., 1994, p. 129-204.

# Optoacoustic Supercontrast for Early Cancer Detection

Alexander A. Karabutov, Elena V. Savateeva, and Alexander A. Oraevsky

Optoacoustic Imaging and Spectroscopy Laboratory, CBME,  
University of Texas Medical Branch, Galveston, Texas, 77555-0456

## ABSTRACT

Thermal mechanism is fundamental for the generation of ultrasonic waves in a course of absorption of laser radiation. Its efficiency is relatively low, but increases significantly with temperature (thermal non-linearity). If the phase transition of the irradiated medium occur, the efficiency may exceed its linear regime value several orders of magnitude. The idea of optoacoustic supercontrast for early cancer detection is based on this fact. We performed feasibility studies and describe requirements to and properties of the optoacoustic supercontrast agent based on nanoscopic particles. The results of the preliminary experiments with the metal and carbon nanoparticles as optoacoustic supercontrast are presented. Theoretical estimations show the possibility to enhance the efficiency of optoacoustic generation up to three orders of magnitude under irradiation conditions of laser optoacoustic imaging in the depth of human tissue.

*Keywords: optoacoustic effect, light absorption and scattering, optoacoustic transients, nanoparticles*

## 1. INTRODUCTION

The optoacoustic tomography (OAT) is a novel promising technique for diagnostic imaging of cancer [1-4]. OAT employs illumination of tissue under study with short laser pulses, generation of ultrasonic waves in tissue due to absorption of laser radiation and detection of profiles of ultrasonic waves with high temporal resolution by an array of ultrawide-band acoustic transducers [5,6]. The optoacoustic imaging takes advantage of high optical contrast between normal and cancerous tissue and low distortion of ultrasonic waves delivering information on the distribution of absorbed optical energy. Estimations show, that it is possible to detect an absorbing sphere with 1 mm in diameter and optical properties of cancerous tissue at a depth of 7 cm in the breast [7,8]. However, the exact value of optoacoustic contrast in small early tumors is yet to be determined. Currently, it is believed that the main portion of the optoacoustic contrast comes from tumor angiogenesis. It is unlikely that an advanced angiogenesis can be developed at the microscopic stage of early tumors. Therefore, further enhancement of optoacoustic imaging contrast will be useful for detection of early cancer at significant depth. Simultaneously, the enhanced contrast would permit application of much lower laser energy for irradiation, which in turn may replace flash-lamp pumped lasers currently employed in OAT with inexpensive and compact diode lasers. In addition, greater sensitivity of OAT will allow the use of greater repetition rate of laser pulses, yielding greater signal-to-noise ratio. The optoacoustic contrast is determined not only by the variations of light absorption and scattering coefficient, but also by the variation of the optoacoustic efficiency. Thus, the idea is not to enhance average light absorption in tissue (as conventional exogenous contrast agents would), but to enhance the optoacoustic efficiency. It is well established, that generation of acoustic waves is substantially more effective if the evaporation or other gas production takes place [9-13]. On the other hand, for the optoacoustic imaging of biological tissue to be safe, the average temperature rise may not exceed 1°C. Therefore, the evaporation can take place only at extremely small absorbing centers in the tissue not to damage the tissue. To achieve threshold for evaporation, photodissociation or other gas production at a safe level of laser energy fluence, the absorbing particles should have dimensions on the nanometer scale. The same limitation for the particle size comes with necessity for the contrast agent to diffuse between cells and penetrate cell membranes.

## 2. THEORY OF OPTOACOUSTIC PHENOMENA IN HETEROGENEOUS MEDIUM

Let us for simplicity reason consider a turbid medium as a clear medium with immersed absorbing particles ( $R_0$  - radius of the particle). Let concentration of the particles,  $n$ , be sufficiently high, so that the quantity of the particles in the

“elementary” volume of  $a \times a \times a$  (see Fig.1) is substantially greater than unity:  $na^3 \gg 1$ .

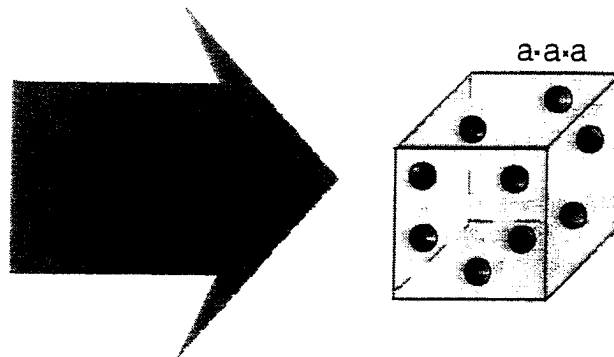


Figure 1. Schematics of heterogeneous medium with distributed nanoparticles.

On the other hand, the concentration should be limited, so that the optical absorption over the “elementary” volume can be taken as homogeneous:  $\sigma na \ll 1$  ( $\sigma = \xi \pi R_0^2$  - cross-section of optical absorption of the particle). Particle absorbs laser radiation and its temperature rises up. Surrounding liquid is heated due to heat diffusion from the particle. Pulsed laser heating of absorbing particle immersed in transparent liquid can be treated in several stages.

If the temperature of the particle does not exceed the boiling point of the liquid,  $T_{ev}$ , (lower limit of the laser fluence), the phase transition cannot occur.

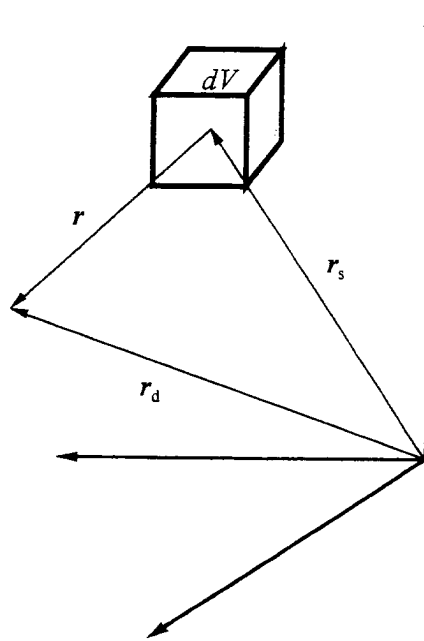


Figure 2. The system of coordinates for calculation of a small volume irradiation.

The temperature of the liquid around the particle after irradiation by the laser pulse can be taken in the following form (the temperature fields of the particles don't overlap due to short laser pulse duration and low concentration of the particles):

$$T = T_0 + (T_p - T_0) \frac{R_0}{r} \exp\left(-\frac{(r - R_0)^2}{4\chi\tau_L}\right); \quad r > R_0. \quad (1)$$

where  $\chi$  is diffusivity of the liquid,  $\tau_L$  is laser pulse duration,  $T_p \leq T_{ev}$  is the temperature of the particle (we consider the temperature in the particle homogeneous).

According to (1), the temperature of the particles can be found as:

$$T_p = T_0 + \frac{\sigma \Phi_0}{4(\rho c_p)_l \sqrt{\chi \tau_L} (\sqrt{\pi} + 2x + \zeta/x)}, \quad (2)$$

where  $\rho$  is the density of the medium (subscript  $L$  stands for "liquid", and subscript  $p$  stands for "particle"),  $c_p$  is the specific heat,  $x = \sqrt{\chi \tau_L} / R_0$  is the ratio of heat diffusion length and particle radius,  $\zeta = \frac{(\rho c_p)_p}{3(\rho c_p)_l}$  characterizes the ratio of heat capacity of the particle and surrounding liquid.

Evaporation starts when the temperature of the particle reaches the boiling point. This threshold of evaporation can be estimated as:

$$\Phi_{th} = \frac{T_{ev} - T_0}{\xi} (\rho c_p)_l * 4 \sqrt{\chi \tau_L} (\sqrt{\pi} + 2x + \zeta/x). \quad (3)$$

The threshold has a minimum at certain particle radius,  $x_{min} = \sqrt{\zeta/2}$ . This gives an optimal radius of the particle in order to minimize the evaporation threshold:

$$R_{opt} = \sqrt{\frac{6(\rho c_p)_l}{(\rho c_p)_p} \chi \tau_L}. \quad (4)$$

The optimal radius of the particle depends on the laser pulse duration, specific heat of the particle and and specific heat of the surrounding liquid. For carbon or metal particle in water and 10 ns laser pulse optimal radius is of the order of 110 nm to 130 nm. As thermal diffusion length in the particle is of the order of 1  $\mu\text{m}$ , the model of homogeneously heated particle is valid. In these conditions the threshold of evaporation may be presented as:

$$\Phi_{min} = \frac{T_{ev} - T_0}{\xi} (\rho c_p)_l 4 \sqrt{\chi \tau_L} (\sqrt{\pi} + 2\sqrt{2\zeta}) \sim 14 \text{ mJ/cm}^2. \quad (5)$$

In an optimum situation, heat containing in the surrounding liquid 4-5 times exceeds that of the particle. If the laser fluence exceeds the threshold (5), evaporation at the particle takes place. If laser fluence does not exceed the threshold (5), then the evaporation of the liquid does not occur and excitation of ultrasound wave takes place due to thermal expansion of the particle and surrounding layer of liquid. As the local temperature rise can be several tens of degrees and higher, the so-called thermal nonlinearity phenomema can occur. The thermal nonlinearity leads to the rise of the efficiency of optoacoustic generation 3-4 times in a case of water (see below).

If the laser fluence exceeds threshold (5) the temperature of the particle and surrounding liquids comes to boiling point at some moment  $t_{ev}$  in a course of laser pulse. Then thin vapor layer is generated around the particle. Due to lower heat conductivity of vapor (relatively to that of liquid), the temperature of the particle continues to increase. After the laser pulse the temperature of the particle relax to the initial value due to heat fluence from the particle through the vapor layer into the liquid. The total mass of the vapor is determined by the heat transmitted from the particle to the liquid. In a course of relaxation at some moment of time the temperature of the particle becomes lower then the boiling point and condensation of the vapor starts. Total mass of vapor produced around single particle does not exceed the following value:

$$m_v = \sigma \Phi_0 / \lambda \quad (6)$$

where  $\lambda$  is the heat of evaporation. We neglect the heat contain of the particle.

The pressure wave, generated by heated elementary volume can be taken in the form:

$$p' = \frac{\rho}{4\pi r} \frac{d^2(\delta V)}{dt^2} \quad (7)$$

where  $\delta V$  is a variation of the elementary volume due thermal expansion and vapor production.

In case of homogeneous bulk absorption of light the expansion of an elementary volume,  $\delta V$ , can be expressed as in [7]:

$$\frac{\delta V_1}{a^3} = \frac{\beta}{\rho c_p} \mu_a \Phi_0 \quad (8)$$

where  $\beta$  is the volume expansion coefficient. Thermal expansion coefficient depends on the temperature and for water this dependence is quite strong (so-called "thermal nonlinearity", see Fig.3). Therefore, before the temperature of the particle can reach the boiling point, the efficiency of the optoacoustic generation increases up to 2-3 times.

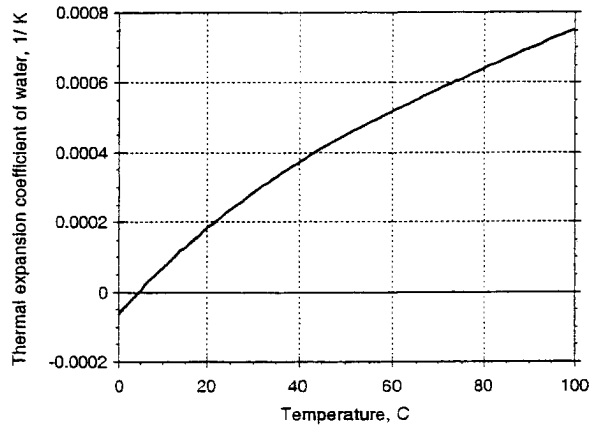


Figure 3. Thermal expansion coefficient of water as a function of temperature.

The thermal sources, producing the acoustic wave can, taken as follows:

$$\beta \delta T = \left( \beta_0 + \frac{d\beta}{dT} \delta T \right) \delta T. \quad (9)$$

Expression (9) shows, that for low temperature rise  $|\beta_0^{-1} d\beta/dT \delta T| \ll 1$  the first term in the brackets dominates and the distribution of heat source is proportional to the temperature rise  $\delta T$ . In an opposite case of relatively high temperature rise  $|\beta_0^{-1} d\beta/dT \delta T| \gg 1$  the second term is much greater than the first and the distribution of heat source is proportional to  $\delta T^2$ . Thus for short laser pulse the spatial distribution of heat sources will be a sum of two exponents:

$$\beta \delta T = \frac{\mu_a \Phi_0}{\rho c_p} \beta_0 e^{-\mu_a z} + \left( \frac{\mu_a \Phi_0}{\rho c_p} \right)^2 \frac{d\beta}{dT} e^{-2\mu_a z}. \quad (10)$$

For low temperature rise (low fluence) the leading edge of the optoacoustic signal (that resembles the spatial distribution of heat sources) will have exponential shape with the exponent  $\mu_a c_0 t$ ; at higher fluence the exponential slope will be 2 times sharper:  $2\mu_a c_0 t$ . In a case of heterogeneous medium with absorbing centers, the variation of the elementary volume due to vapor production can be estimated as (we consider pressure relaxed):

$$\frac{\delta V_2}{a^3} = \frac{\mu_a \Phi_0}{\rho_v \lambda} \quad (11)$$

where  $\rho_v$  is the vapor density. Heating of the vapor will give further rise to the elementary volume:

$$\frac{\delta V_3}{a^3} = \frac{\mu_a \Phi_0}{p_0} \frac{\gamma - 1}{\gamma} \quad (12)$$

where  $\gamma$  is the adiabatic exponent,  $p_0$  is ambient pressure.

Let's compare the efficiency of various mechanisms of the optoacoustic phenomena. Volume deformation per unit specific heat release for various mechanisms are presented in the Table below.

	Thermal expansion of liquid water	Vapor Production	Thermal expansion of water vapor
$\delta V / \mu_a \Phi_0 a^3, \text{ cm}^3 / \text{J}$	$8.6 * 10^{-5}$	$3.2 * 10^{-1}$	1.7

Thus, light absorption by submicron-size particles can enhance the efficiency of optoacoustic generation by several orders of magnitude, but this process has a threshold dependent on laser pulse duration and size of the particle.

### 3. MATERIALS AND EXPERIMENTAL SET-UP

Studies of the optoacoustic phenomena in heterogeneous media were made with the Q-switched Nd-YAG laser (laser pulse duration  $\tau_L \approx 14 \text{ ns}$  at 1/e level) operated at fundamental ( $\lambda = 1.064 \mu\text{m}$ ) wavelength and the second harmonic ( $\lambda = 0.532 \mu\text{m}$ ). The laser pulse energy was varied by neutral density filters. Pulse repetition rate did not exceed 3 Hz and was chosen to fulfill the safety requirement not to elevate the average temperature of the medium more than 1 degree. Actually, most of the measurements have been done with single laser pulses.

We used optically heterogeneous media: water solution of India ink of various concentrations, water suspension of gold nanoparticles (diameter 10 nm, 30 nm and 100 nm) with the volume concentration of the particles of the order of  $10^{-6}$ . As a reference homogeneous medium water solution of cupric chloride of various concentrations was employed.

The enhancement of the optoacoustic imaging contrast in heterogeneous medium was investigated with laser optoacoustic imaging system (LOIS-2) designed for breast cancer imaging. The system uses 32-element arc-shaped array of piezoelectric transducers with ultrasonic frequency band of 0.05-3 MHz, which provides spatial resolution of the order of 0.5 mm.

### 4. EXPERIMENTAL RESULTS

The leading edges of optoacoustic signals generated in 1% solution of India ink in water for various energy fluences are depicted in Fig. 4. The light absorption coefficient of this solution was  $\mu_a = 18 \text{ cm}^{-1}$ .

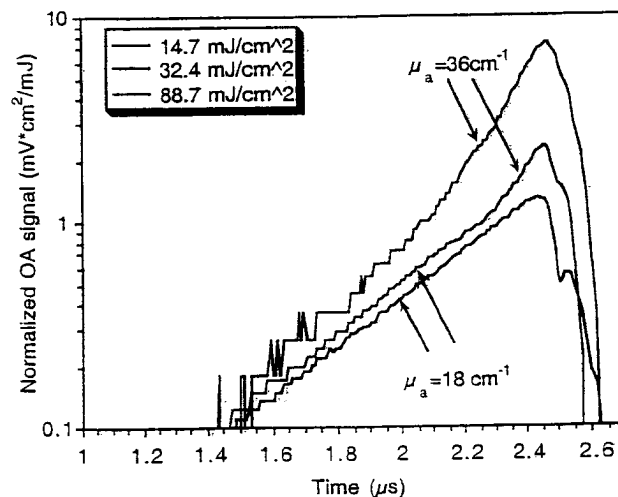


Figure 4. Profiles of leading edges of the optoacoustic signals in aqueous solutions of 1% India ink generated by laser pulses with three different fluences.

For low fluence ( $\Phi_0 = 14.7 \text{ mJ/cm}^2$ ) the leading edge has exponential shape with the exponent, consistent with the light absorption coefficient (see (10)). With an increase of the incident fluence ( $\Phi_0 = 88.7 \text{ mJ/cm}^2$ ), the slope becomes steeper and corresponds to 2 times sharper exponent (see (10), the second term). In the intermediate case ( $\Phi_0 = 32.4 \text{ mJ/cm}^2$ ) beneath the surface the slope is two times higher, then in the depth of the irradiated volume (see Fig.4). This is in consistence with the "thermal nonlinearity" model (see (9)-(10)).

Let's discuss the intermediate case  $\Phi_0 = 32.4 \text{ mJ/cm}^2$  in more details. If we assume homogeneous absorption of light in the aqueous solution, the maximum temperature-rise will be  $\Delta T = \mu_a \Phi_0 / \rho c_p \approx 0.14 \text{ K}$ . On the other hand, the influence of thermal nonlinearity is so significant, that it cannot be expected for such a low temperature elevation. The local temperature-rise can be estimated from the ratio of the amplitudes of exponents in (10). Fit of the leading edge of the optoacoustic signal with the formula (10) yields  $\beta_0^{-1} \frac{d\beta}{dT} \delta T \approx 0.51$ , which makes it possible to estimate the local temperature elevation as  $\delta T \approx 10 \text{ K}$  (for water at room temperature  $\beta_0^{-1} \frac{d\beta}{dT} \approx 0.05 \text{ K}^{-1}$ ). Thus, the absorbing carbon particles are exposed to at least 70 times higher temperature-rise then the average temperature elevation in the irradiated volume of the solution. Inside the practice the temperature is even higher.

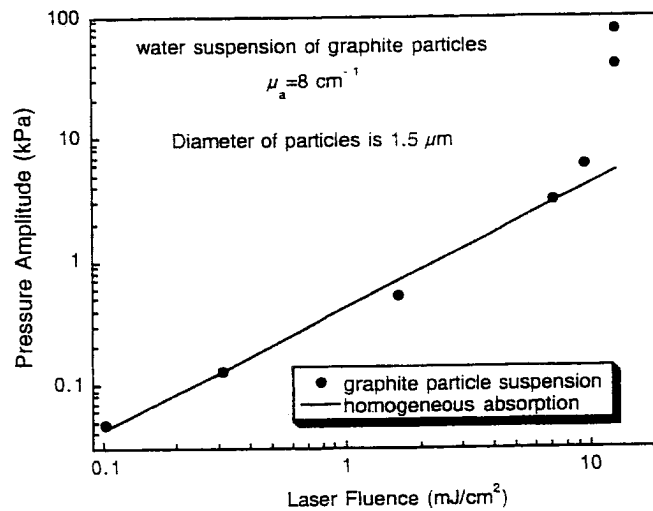


Figure 5. Amplitude of optoacoustic signal vs. energy fluence for water suspension of carbon particles.

The dependence of the amplitude of optoacoustic signal vs. laser energy fluence for water suspension of carbon particles is presented in Fig.5. The diameter of the particles was close to optimal (see (4)), so it was reasonable to expect manifestation of evaporation at absorbing centers for the laser fluence of approximately  $(15 - 20) \text{ mJ/cm}^2$  and significant thermal nonlinearity below this limit.

The presented data is consistent with the theoretical model discussed above. For fluences  $\Phi_0 < 8 \text{ mJ/cm}^2$  the amplitude of the optoacoustic signal generated in heterogeneous medium (points in Fig.5) is proportional to the fluence and coincides well with the theoretical value for homogeneous medium (solid line). This means that the temperature-rise at the absorbing particle is relatively low (at least below 10 K) and no thermal nonlinearity is manifested.

In the fluence range of  $8 \text{ mJ/cm}^2 < \Phi_0 < 15 \text{ mJ/cm}^2$  the amplitude of the optoacoustic signal generated in heterogeneous medium exceeds that in a homogeneous medium up to 3 times. This corresponds well to the rise of optoacoustic generation efficiency due to thermal nonlinearity below the evaporation threshold. For higher fluence  $\Phi_0 > 15 \text{ mJ/cm}^2$  a sharp increase of the amplitude of excited signals takes place. It may occur due to the elevation of the temperature of particles to the boiling point and following evaporation of water layer around the absorbing particle. In accordance with the enhancement of the efficiency of optoacoustic generation in vapor production regime (see Table 1), a dramatic increase of the amplitude of

Optoacoustic images of the same vessels filled with the water suspension of gold particles of various diameter at  $\lambda = 0.53 \mu\text{m}$  are presented in Fig.7 (volume concentration of the particles was  $3 \cdot 10^{-6}$ ). For the fluence below the evaporation threshold (Fig.7a) the 100 nm in diameter particles (vessel 3) produce the brightest image, due to higher light absorption coefficient of the solution. Correspondingly, the solutions of 30 nm (vessel 2) and 10 nm (vessel 1) particles produce the images with lower intensity. For the fluence above evaporation threshold (Fig.7b) the brightest image was produced by 10 nm particles, and the intensity of the images is reverse to that below the threshold.

## 5. DISCUSSION AND CONCLUSIONS

Light absorbing nanoparticles were studied as a potentially very effective contrast agent for laser optoacoustic imaging in tissue. Enhanced efficiency of acoustic wave generation can take place due to superheating of absorbing particles followed by evaporation of the surrounding water layer. Some other phenomena of phase transition and gas production can be utilized. Laser generation of ultrasound in heterogeneous medium can be 2-3 orders more efficient than that in optically homogeneous medium. An optimal particle size yielding minimal threshold of evaporation at the particle surface was found in the range of ~100-nm. The threshold of evaporation is relatively high and exceeds  $10 \text{ mJ/cm}^2$  for metal or carbon particles suspension in water. However, application of the plasmon resonance absorption in the particle, the threshold can be lowered drastically (due to higher crosssection of light absorption). One can expect a decrease of the threshold up to 2-3 orders of magnitude in case of utilization of plasmon resonance for nanoparticle absorption.

Nanotechnology is a rapidly expanding field of science and engineering that offers a unique potential for integrating contrast agents and receptor-specific markers for cancer, promising to yield smart contrast agents. Gold nanoshells filled with silica can be produced to absorb strongly the desired wavelength of near infrared laser pulses [14]. These nanoparticles may be further modified to yield exponential enhancement of optoacoustic signals upon pulsed laser irradiation. Effective bioconjugates have been found to link various nanoparticles with biological molecules [15]. The problem of selective targeting of cancerous cells and tissues is currently also under active development. Peptides, other ligands and antibodies specific to surface receptors in breast cancer cells or endothelial cell of tumor microcapillary network are available for selective targeting of malignant tumors [16,17]. Thus, all components are available for successful development of the optoacoustic imaging technique with supercontrast. A receptor-specific contrast agent in combination with optoacoustic imaging may dramatically enhance the level of sensitivity of detection of small breast tumors, reduce the rate of false positives and negatives, provide diagnostic imaging information, and be useful in monitoring for early stages of breast cancer and cancer recurrence.

We conclude that absorbing nanoparticles conjugated with targeting agents specific to cancer may be applied as a particulate contrast agent for early detection of cancer with laser optoacoustic imaging system.

## 6. ACKNOWLEDGEMENTS

This work was supported by the National Cancer Institute (grant #R29-CA80221) and DOD Breast Cancer Research Program, US Army (grant #DAMD17-99-1-9404).

## 7. REFERENCES

1. A.A. Oraevsky, S.L. Jacques, R.O. Esenaliev, F.K. Tittel: Time-Resolved Optoacoustic Imaging in Layered Biological Tissues", In: "Advances in Optical Imaging and Photon Migration", vol. 21, ed. by R.R. Alfano, Academic Press (1994) pp. 161-165.
2. A.A. Oraevsky, S.L. Jacques, R.O. Esenaliev, F.K. Tittel: Laser based optoacoustic imaging in biological tissues, *Proc. SPIE* 1994; **2134A**: 122-128.
3. R.A. Kruger, P. Liu: Photoacoustic ultrasound: Pulse production and detection in 0.5% Liposyn, *Medical Physics*, 1994; **21**(7): 1179-1184.
4. R.A. Kruger: Photoacoustic ultrasound, *Med. Phys.* 1994; **21**(1): 127-131
5. A.A. Oraevsky, S.L. Jacques, F.K. Tittel: Measurement of tissue optical properties by time-resolved detection of laser-induced transient stress, *Applied Optics*, 1997; **36**(1): 402-415

6. A.A. Oraevsky: Laser optoacoustic imaging for cancer diagnosis. *LEOS NewsLetter* 1996; **10**(6): 17-20.
7. A.A. Oraevsky, V.G.Andreev, A.A.Karabutov, R.O.Esenaliev, "Two-dimensional optoacoustic tomography: transducer array and image reconstruction algorithm", *SPIE Proceed.* **3601**, 256-267 (1999).
8. R.O. Esenaliev, A.A. Karabutov, A.A. Oraevsky: Sensitivity of laser opto-acoustic imaging in detection of small deeply embedded tumors, *IEEE J. ST Quant. Electr.* 1999; **5**(4):981-988.
9. G.J. Diebold, M.I. Khan, S.M. Park: "Photoacoustic signatures of particulate matter: optical production of acoustis monopole radiation", *Science* 1990; **250**: 101-104.
10. F.V. Bunkin, M.I. Tribelsky, *Sov.Phys.Uspekhi*, **130**, 193 (1980).
11. M.W. Sigrist, Laser generation of acoustic pulses, *J. Appl. Phys.*, **60**. R83 (1986).
12. R.O. Esenaliev, A.A. Karabutov, N.B. Podymova, V.S. Letokhov, "Laser ablation of aqueous solutions with spatially homogeneous and heterogeneous absorption". *Appl. Phys. B*, **59**. 73-81 (1994).
13. A.C. Beveridge, T.E. McGrath, G.J. Diebold, A.A. Karabutov, "Photoacoustic shock generation in carbon suspension", *Appl. Phys. Lett.*, **75**(26), 4204-4206 (1999).
14. S.J. Oldenburg, R.D. Averitt, S.L. Wescott, N.J. Halas: Nanoengineering of optical resonances, *Chem. Phys. Lett.* 1998; **288**: 243-247.
15. H. Pinto-Alphandary, A. Adremont, P. Couvreur: "Targeted delivery of antibiotics using liposomes and nanoparticles: research and applications. *Int. J. Antimicrob Agents* 2000; **13**(3):155-168.
16. H.M. Ellerby, R. Pasqualini et al. Anti-cancer activity of targeted pro-apoptotic peptides, *Nature Med.* 1999; **5**(9): 1032-1038.
17. L.M. Weiner, G.P. Adams: New approaches to antibody therapy, *Oncogene* 2000; **19**(53): 6144-6151.

# Enhancement of optoacoustic tissue contrast with absorbing nanoparticles

Alexander A. Oraevsky, Alexander A. Karabutov, and Elena V. Savateeva

Optoacoustic Imaging and Spectroscopy Laboratory, Center for Biomedical Engineering,  
University of Texas Medical Branch, Galveston, Texas, 77555-0456

## ABSTRACT

Laser induced phase transition in the liquid surrounding absorbing nanoparticle results in dramatic enhancement of the thermoacoustic efficiency and excitation of high-amplitude pressure waves. Feasibility study were performed in tissue phantoms. Experiments supported with theoretical model demonstrated possibility to increase the efficiency of optoacoustic generation in tissue up to three orders of magnitude by application of absorbing nanoparticles with optimal diameter.

**Keywords:** *optoacoustic effect, light absorption and scattering, optoacoustic transients, nanoparticles*

## 1. INTRODUCTION

The optoacoustic tomography (OAT) is a novel promising technique for diagnostic imaging of cancer [1-4]. OAT employs illumination of tissue under study with short laser pulses, generation of ultrasonic waves in tissue due to absorption of laser radiation and detection of profiles of ultrasonic waves with high temporal resolution by an array of ultrawide-band acoustic transducers [5,6]. The optoacoustic imaging takes advantage of high optical contrast between normal and cancerous tissue and low distortion of ultrasonic waves delivering information on the distribution of absorbed optical energy. Estimations show, that it is possible to detect an absorbing sphere with 1 mm in diameter and optical properties of cancerous tissue at a depth of 7 cm in the breast [7,8]. However, the exact value of optoacoustic contrast in small early tumors is yet to be determined. Currently, it is believed that the main portion of the optoacoustic contrast comes from tumor angiogenesis. It is unlikely that an advanced angiogenesis can be developed at the microscopic stage of early tumors. Therefore, further enhancement of optoacoustic imaging contrast will be useful for detection of early cancer at significant depth. Simultaneously, the enhanced contrast would permit application of much lower laser energy for irradiation, which in turn may replace flash-lamp pumped lasers currently employed in OAT with inexpensive and compact diode lasers. In addition, greater sensitivity of OAT will allow the use of greater repetition rate of laser pulses, yielding greater signal-to-noise ratio. The optoacoustic contrast is determined not only by the variations of light absorption and scattering coefficient, but also by the variation of the optoacoustic efficiency. Thus, the idea is not to enhance average light absorption in tissue (as conventional exogenous contrast agents would), but to enhance the optoacoustic efficiency. It is well established, that generation of acoustic waves is substantially more effective if the evaporation or other gas production takes place [9-13]. On the other hand, for the optoacoustic imaging of biological tissue to be safe, the average temperature rise may not exceed 1°C. Therefore, the evaporation can take place only at extremely small absorbing centers in the tissue not to damage the tissue. To achieve threshold for evaporation, photodissociation or other gas production at a safe level of laser energy fluence, the absorbing particles should have dimensions on the nanometer scale. The same limitation for the particle size comes with necessity for the contrast agent to diffuse between cells and penetrate cell membranes

## 2. OPTOACOUSTIC PHENOMENA IN HETEROGENEOUS MEDIUM

Let us for simplicity reason consider a turbid medium as a clear medium with immersed absorbing particles ( $R_0$  - radius of the particle). Let concentration of the particles,  $n$ , be sufficiently high, so that the quantity of the particles in the "elementary" volume of  $a \times a \times a$  (see Fig.1) is substantially greater than unity:  $na^3 \gg 1$ .

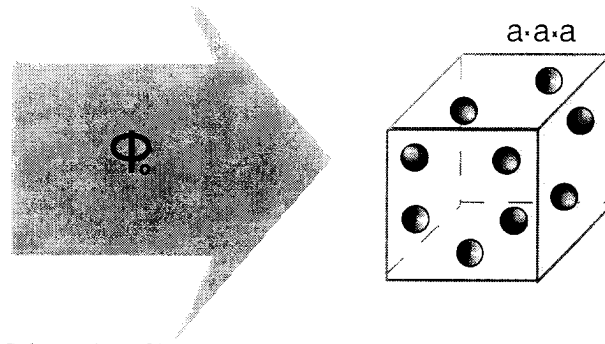


**Figure 1.** Schematics of heterogeneous medium with distributed nanoparticles.

On the other hand, the concentration should be limited, so that the optical absorption over the “elementary” volume can be taken as homogeneous:  $\sigma na \ll 1$  ( $\sigma = \xi \pi R_0^2$  - cross-section of optical absorption of the particle). Particle absorbs laser radiation and its temperature rises up. Surrounding liquid is heated due to heat diffusion from the particle. Pulsed laser heating of an absorbing particle immersed in transparent liquid can be treated in several stages.

If the temperature of the particle does not exceed the boiling point of the liquid,  $T_{ev}$ , (lower limit of the laser fluence), the phase transition cannot occur.

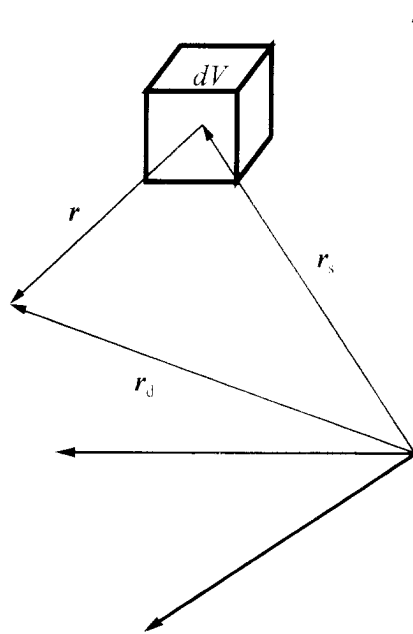


**Figure 2.** The system of coordinates for calculation of a small volume irradiation.

The temperature of the liquid around the particle after irradiation by the laser pulse can be taken in the following form (the temperature fields of the particles don't overlap due to short laser pulse duration and low concentration of the particles):

$$T = T_0 + (T_p - T_0) \frac{R_0}{r} \exp\left(-\frac{(r - R_0)^2}{4\chi\tau_L}\right); \quad r > R_0. \quad (1)$$

where  $\chi$  is diffusivity of the liquid,  $\tau_L$  is laser pulse duration,  $T_p \leq T_{ev}$  is the temperature of the particle (we consider the temperature distribution in the particle homogeneous).

According to (1), the temperature of the particles can be found as:

$$T_p = T_0 + \frac{\sigma \Phi_0}{4(\rho c_p)_l \sqrt{\chi \tau_L} (\sqrt{\pi} + 2x + \zeta/x)}, \quad (2)$$

where  $\rho$  is the density of the medium (subscript  $l$  stands for “liquid”, and subscript  $p$  stands for “particle”),  $c_p$  is the specific heat,  $x = \sqrt{\chi \tau_L} / R_0$  is the ratio of heat diffusion length and particle radius,  $\zeta = \frac{(\rho c_p)_p}{3(\rho c_p)_l}$  characterizes the ratio of heat capacity of the particle and surrounding liquid.

Evaporation starts when the temperature of the particle reaches the boiling point. This threshold of evaporation can be estimated as:

$$\Phi_{th} = \frac{T_{ev} - T_0}{\xi} (\rho c_p)_l * 4 \sqrt{\chi \tau_L} (\sqrt{\pi} + 2x + \zeta/x). \quad (3)$$

The threshold has a minimum at certain particle radius,  $x_{min} = \sqrt{\zeta/2}$ . This gives an optimal radius of the particle in order to minimize the evaporation threshold:

$$R_{opt} = \sqrt{\frac{6(\rho c_p)_l}{(\rho c_p)_p} \chi \tau_L}. \quad (4)$$

The optimal radius of the particle depends on the laser pulse duration, specific heat of the particle and specific heat of the surrounding liquid. For carbon or metal particle in water and 10 ns laser pulse optimal radius is of the order of 110 nm to 130 nm. As thermal diffusion length in the particle is of the order of 1  $\mu$ m, the model of homogeneously heated particle is valid. In these conditions the threshold of evaporation may be presented as:

$$\Phi_{min} = \frac{T_{ev} - T_0}{\xi} (\rho c_p)_l 4 \sqrt{\chi \tau_L} (\sqrt{\pi} + 2\sqrt{2\zeta}) \sim 14 \text{ mJ/cm}^2. \quad (5)$$

In an optimum situation, heat containing in the surrounding liquid 4-5 times exceeds that of the particle. If the laser fluence exceeds the threshold (5), evaporation at the particle takes place. If laser fluence does not exceed the threshold (5), then the evaporation of the liquid does not occur and excitation of ultrasound wave takes place due to thermal expansion of the particle and surrounding layer of liquid. As the local temperature rise can be several tens of degrees and higher, the so-called thermal nonlinearity phenomenon is manifested. The thermal nonlinearity leads to the rise of the efficiency of optoacoustic generation 3-4 times in a case of water (see below).

If the laser fluence exceeds threshold (5) the temperature of the particle and surrounding liquids comes to boiling point at some moment  $t_{ev}$  in a course of laser pulse. Then thin vapor layer is generated around the particle. Due to lower heat conductivity of vapor (relatively to that of liquid), the temperature of the particle continues to increase. After the laser pulse the temperature of the particle relax to the initial value due to heat flux from the particle through the vapor layer into the liquid. The total mass of the vapor is determined by the heat, transmitted from the particle to the liquid. In a course of relaxation at some moment of time the temperature of the particle becomes lower than the boiling point and condensation of the vapor starts. Total mass of vapor produced around single particle does not exceed the following value:

$$m_v = \sigma \Phi_0 / \lambda \quad (6)$$

where  $\lambda$  is the heat of evaporation. We neglect the heat contain of the particle.

The pressure wave, generated by heated elementary volume can be taken in the form:

$$p' = \frac{\rho}{4\pi r} \frac{d^2(\delta V)}{dt^2} \quad (7)$$

where  $\delta V$  is a variation of the elementary volume due thermal expansion and vapor production.

In case of homogeneous bulk absorption of light the expansion of an elementary volume,  $\delta V$ , can be expressed as in [7]:

$$\frac{\delta V_1}{a^3} = \frac{\beta}{\rho c_p} \mu_a \Phi_0 \quad (8)$$

where  $\beta$  is the volume expansion coefficient. Thermal expansion coefficient depends on the temperature and for water this dependence is quite strong (so-called “thermal nonlinearity”, see Fig.3). Therefore, before the temperature of the particle can reach the boiling point, the efficiency of the optoacoustic generation increases up to 2-3 times.

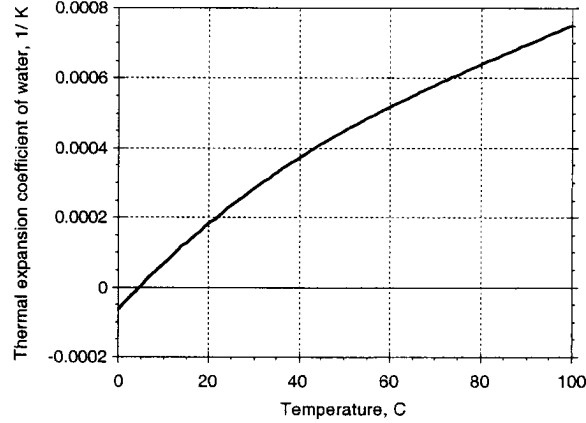


**Figure 3.** Thermal expansion coefficient of water as a function of temperature.

The thermal sources, producing the acoustic wave can, taken as follows:

$$\beta \delta T = \left( \beta_0 + \frac{d\beta}{dT} \delta T \right) \delta T. \quad (9)$$

Expression (9) shows, that for low temperature rise  $\left| \beta_0^{-1} \frac{d\beta}{dT} \delta T \right| \ll 1$  the first term in the brackets dominates and the distribution of heat source is proportional to the temperature rise  $\delta T$ . In an opposite case of relatively high temperature rise  $\left| \beta_0^{-1} \frac{d\beta}{dT} \delta T \right| \gg 1$  the second term is much greater than the first and the distribution of heat source is proportional to  $\delta T^2$ . Thus for short laser pulse the spatial distribution of heat sources will be a sum of two exponents:

$$\beta \delta T = \frac{\mu_a \Phi_0}{\rho c_p} \beta_0 e^{-\mu_a z} + \left( \frac{\mu_a \Phi_0}{\rho c_p} \right)^2 \frac{d\beta}{dT} e^{-2\mu_a z}. \quad (10)$$

For low temperature rise (low fluence) the leading edge of the optoacoustic signal (that resembles the spatial distribution of heat sources) will have exponential shape with the exponent  $\mu_a c_0 t$ ; at higher fluence the exponential slope will be 2 times sharper:  $2\mu_a c_0 t$ . In a case of heterogeneous medium with absorbing centers, the variation of the elementary volume due to vapor production can be estimated as (we consider pressure relaxed):

$$\frac{\delta V_2}{a^3} = \frac{\mu_a \Phi_0}{\rho_v \lambda} \quad (11)$$

where  $\rho_v$  is the vapor density. Heating of the vapor will give further rise to the elementary volume:

$$\frac{\delta V_3}{a^3} = \frac{\mu_a \Phi_0}{p_0} \frac{\gamma - 1}{\gamma} \quad (12)$$

where  $\gamma$  is the adiabatic exponent,  $p_0$  is ambient pressure.

Let's compare the efficiency of various mechanisms of the optoacoustic phenomena. Volume deformation per unit specific heat release for various mechanisms are presented in the Table below.

	Thermal expansion of liquid water	Vapor Production	Thermal expansion of water vapor
$\delta V/\mu_a \Phi_0 a^3, \text{ cm}^3/\text{J}$	$8.6 \cdot 10^{-5}$	$3.2 \cdot 10^{-1}$	1.7

Thus, light absorption by submicron-size particles can enhance the efficiency of optoacoustic generation by several orders of magnitude, but this process has a threshold dependent on laser pulse duration, size of the particle and the light absorption cross-section.

### 3. MATERIALS AND EXPERIMENTAL SET-UP

Studies of the optoacoustic phenomena in heterogeneous media were performed with the Q-switched Nd-YAG laser (laser pulse duration  $\tau_L \approx 14 \text{ ns}$  at  $1/e$  level) operated at fundamental ( $\lambda = 1.064 \mu\text{m}$ ) wavelength and the second harmonic ( $\lambda = 0.532 \mu\text{m}$ ). The laser pulse energy was varied by neutral density filters. Pulse repetition rate did not exceed 3 Hz and was chosen to fulfill the safety requirement not to elevate the average temperature of the medium more than 1 degree. Actually, most of the measurements have been done with single laser pulses.

We used optically heterogeneous media: water solution of India ink of various concentrations, water suspension of gold nanoparticles (diameter 10 nm, 30 nm and 100 nm) with the volume concentration of the particles of the order of  $10^{-6}$ . As a reference homogeneous medium water solution of cupric chloride of various concentrations was employed.

The enhancement of the optoacoustic imaging contrast in heterogeneous medium was investigated with laser optoacoustic imaging system (LOIS-2) designed for breast cancer imaging. The system uses 32-element arc-shaped array of piezoelectric transducers with ultrasonic frequency band of 0.05-3 MHz, which provides spatial resolution of the order of 0.5 mm.

### 4. EXPERIMENTAL RESULTS

The leading edges of optoacoustic signals generated in 1% solution of India ink in water for various energy fluences are depicted in Fig. 4. The light absorption coefficient of this solution was  $\mu_a = 18 \text{ cm}^{-1}$ .

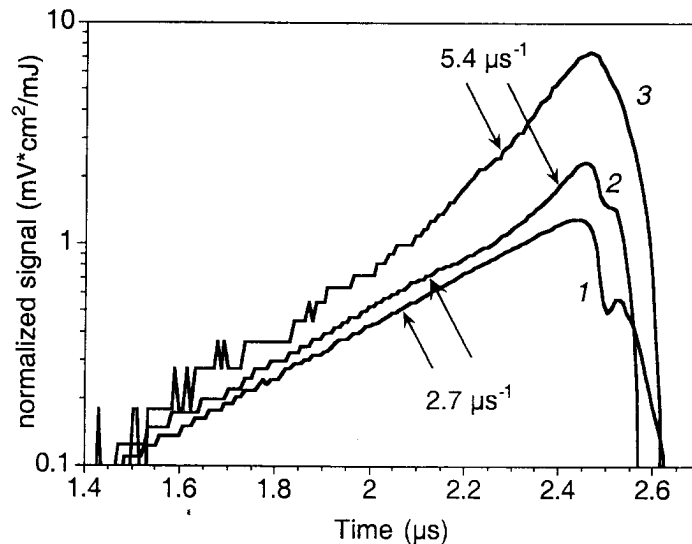


**Figure 4.** Profiles of leading edges of the optoacoustic signals in aqueous solutions of 1% India ink generated by laser pulses with three different fluences.

For low fluence ( $\Phi_0 = 14.7 \text{ mJ/cm}^2$ , curve 1) the leading edge has exponential shape with the exponent, consistent with the light absorption coefficient (see (10)). With an increase of the incident fluence ( $\Phi_0 = 88.7 \text{ mJ/cm}^2$ , curve 3), the slope becomes steeper and corresponds to 2 times sharper exponent (see (10), the second term). In the intermediate case ( $\Phi_0 = 32.4 \text{ mJ/cm}^2$ , curve 2) beneath the surface the slope is two times higher, then in the depth of the irradiated volume (see Fig.4). This is in consistence with the “thermal nonlinearity” model (see (9)-(10)).

Let’s discuss the intermediate case  $\Phi_0 = 32.4 \text{ mJ/cm}^2$  in more details. If we assume homogeneous absorption of light in the aqueous solution, the maximum temperature-rise will be  $\Delta T = \mu_a \Phi_0 / \rho c_p \approx 0.14 \text{ K}$ . On the other hand, the influence of thermal nonlinearity is so significant, that temperature elevation can’t be expected such low. The local temperature-rise can be estimated from the ratio of the amplitudes of exponents in (10). Fit of the leading edge of the optoacoustic signal with the formula (10) yields  $\beta_0^{-1} \frac{d\beta}{dT} \delta T \approx 0.51$ , which makes it possible to estimate the local temperature elevation as  $\delta T \approx 10 \text{ K}$  (for water at room temperature  $\beta_0^{-1} \frac{d\beta}{dT} \approx 0.05 \text{ K}^{-1}$ ). Thus, the absorbing carbon particles are exposed to at least 70 times higher temperature-rise then the average temperature elevation in the irradiated volume of the solution.

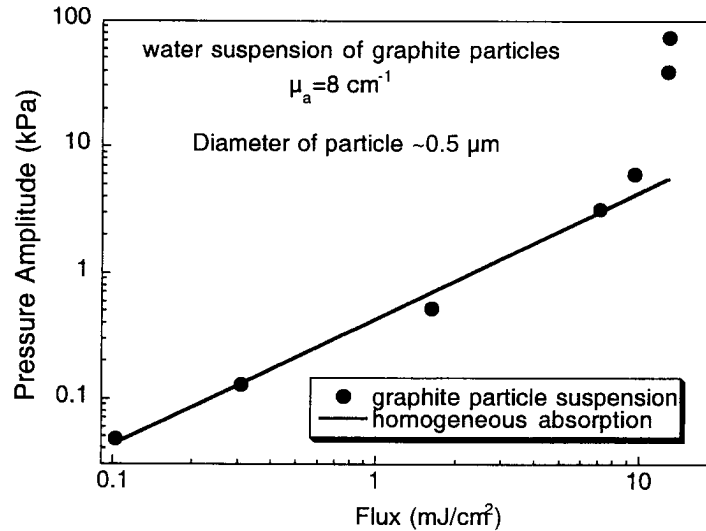


**Figure 5.** Amplitude of optoacoustic signal vs. energy fluence for water suspension of carbon particles.

The dependence of the amplitude of optoacoustic signal vs. laser energy fluence for water suspension of carbon particles is presented in Fig.5. The diameter of the particles was approximately  $0.5 \mu\text{m}$  and was close to optimal value (see (4)), so it was reasonable to expect manifestation of evaporation at absorbing centers for the laser fluence of approximately  $(15 - 20) \text{ mJ/cm}^2$  and significant thermal nonlinearity below this limit.

The presented data is consistent with the theoretical model discussed above. For fluences  $\Phi_0 < 8 \text{ mJ/cm}^2$  the amplitude of the optoacoustic signal generated in heterogeneous medium (points in Fig.5) is proportional to the fluence and coincides well with the theoretical value for homogeneous medium (solid line). This means that the temperature-rise at the absorbing particle is relatively low (at least below 10 K) and no thermal nonlinearity is manifested.

In the fluence range of  $8 \text{ mJ/cm}^2 < \Phi_0 < 15 \text{ mJ/cm}^2$  the amplitude of the optoacoustic signal generated in heterogeneous medium exceeds that in a homogeneous medium up to 3 times. This corresponds well to the rise of optoacoustic generation efficiency due to thermal nonlinearity below the evaporation threshold. For higher fluence  $\Phi_0 > 15 \text{ mJ/cm}^2$  a sharp increase of the amplitude of excited signals takes place. It may occur due to the elevation of the temperature of particles to the boiling point and following evaporation of water layer around the absorbing particle. In accordance with the enhancement of the efficiency of optoacoustic generation in vapor production regime (see Table), a dramatic increase of the amplitude of

optoacoustic signal can be seen. The enhancement of the amplitude of optoacoustic signal about 2 orders was achieved. The threshold of evaporation at the particle is in good agreement with the theoretical estimations (see (5)).

The experiments described above were performed with a single piezoelectric transducer. To investigate the enhancement of the contrast of optoacoustic imaging with the heterogeneous absorbing medium, a 32-elements arc-shaped transducer array of LOIS-2 imaging system was employed. The transducer was attached to the tank, filled with milk (light attenuation coefficient  $\mu_{eff} = 1 \text{ cm}^{-1}$ ). Two 2.4-mm diameter vessels were embedded in the tank. One of them was filled with water solution of cupric chloride (homogeneous absorber), the other – with water solution of India ink (heterogeneous absorber). The light absorption coefficient of heterogeneous and homogeneous medium was the same.

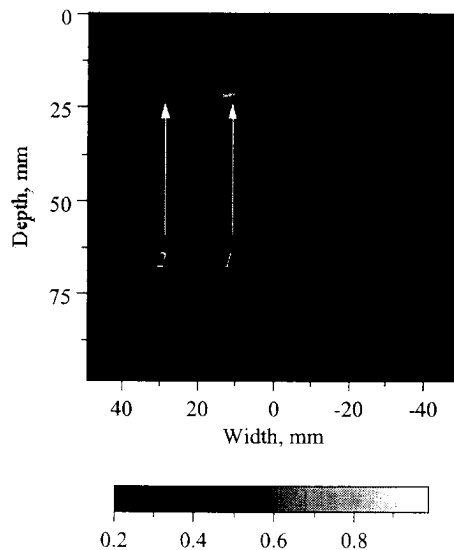


**Figure 6.** Optoacoustic image of vessels with heterogeneous (1) and homogeneous (2) absorption.

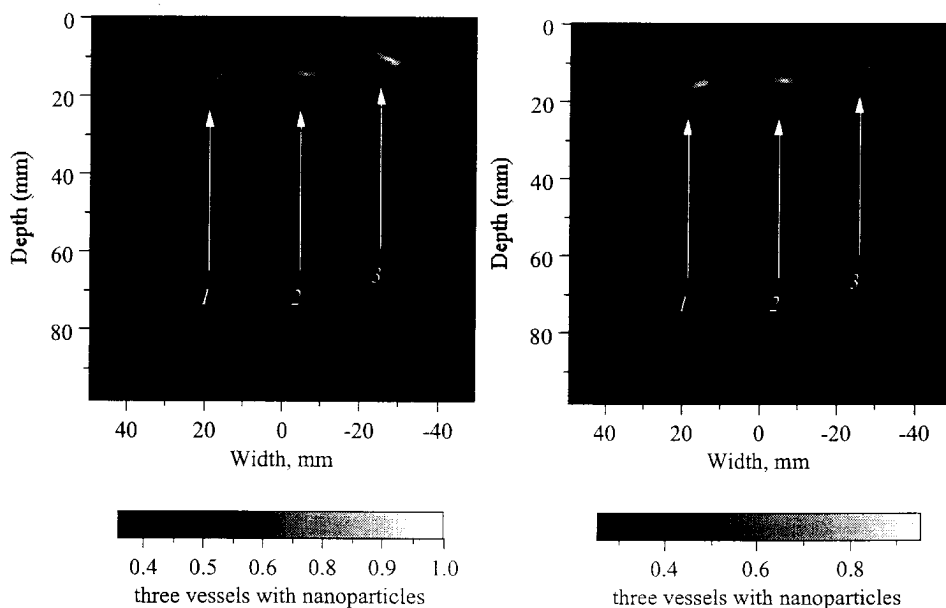


**Figure 7.** Optoacoustic image of vessels with gold particles 10 nm in diameter (1), 30 nm (2) and 100 nm (3).  $\Phi_0 = 13.4 \text{ mJ/cm}^2$  (left panel). Optoacoustic image of similar nanoparticles at  $\Phi_0 = 71 \text{ mJ/cm}^2$  (right panel).

Optoacoustic images of the same vessels filled with the water suspension of gold particles of various diameter at  $\lambda = 0.53 \mu\text{m}$  are presented in Fig.7 (volume concentration of the particles was  $3 \cdot 10^{-6}$ ). For the fluence below the evaporation threshold (Fig.7a) the 100 nm in diameter particles (vessel 3) produce the brightest image, due to higher light absorption coefficient of the solution. Correspondingly, the solutions of 30 nm (vessel 2) and 10 nm (vessel 1) particles produce the images with lower intensity. For the fluence above evaporation threshold (Fig.7b) the brightest image was produced by 10 nm particles, and the intensity of the images is reverse to that below the threshold.

## 5. DISCUSSION AND CONCLUSIONS

Light absorbing nanoparticles were studied as a potentially very effective contrast agent for laser optoacoustic imaging in tissue. Enhanced efficiency of acoustic wave generation can take place due to superheating of absorbing particles followed by evaporation of the surrounding water layer. Some other phenomena of phase transition and gas production can be utilized. Laser generation of ultrasound in heterogeneous medium can be 2-3 orders more efficient than that in optically homogeneous medium. An optimal particle size yielding minimal threshold of evaporation at the particle surface was found in the range of ~200-nm. The threshold of evaporation is relatively high and exceeds  $10 \text{ mJ/cm}^2$  for metal or carbon particles suspension in water. However, application of the plasmon resonance absorption in the particle, the threshold can be lowered drastically (due to higher cross-section of light absorption). One can expect a decrease of the threshold up to 2-3 orders of magnitude in case of utilization of plasmon resonance for nanoparticle absorption.

Nanotechnology is a rapidly expanding field of science and engineering that offers a unique potential for integrating contrast agents and receptor-specific markers for cancer, promising to yield smart contrast agents. Gold nanoshells filled with silica can be produced to absorb strongly the desired wavelength of near infrared laser pulses [14]. These nanoparticles may be further modified to yield exponential enhancement of optoacoustic signals upon pulsed laser irradiation. Effective bioconjugates have been found to link various nanoparticles with biological molecules [15]. The problem of selective targeting of cancerous cells and tissues is currently also under active development. Peptides, other ligands and antibodies specific to surface receptors in breast cancer cells or endothelial cell of tumor microcapillary network are available for selective targeting of malignant tumors [16,17]. Thus, all components are available for successful development of the optoacoustic imaging technique with supercontrast. A receptor-specific contrast agent in combination with optoacoustic imaging may dramatically enhance the level of sensitivity of detection of small breast tumors, reduce the rate of false positives and negatives, provide diagnostic imaging information, and be useful in monitoring for early stages of breast cancer and cancer recurrence.

We conclude that absorbing nanoparticles conjugated with targeting agents specific to cancer may be applied as a particulate contrast agent for early detection of cancer with laser optoacoustic imaging system.

## 6. ACKNOWLEDGEMENTS

This work was supported by the National Cancer Institute (grant #R29-CA80221) and DOD Breast Cancer Research Program, US Army (grant #DAMD17-99-1-9404).

## 7. REFERENCES

1. A.A. Oraevsky, S.L. Jacques, R.O. Esenaliev, F.K. Tittel: Time-Resolved Optoacoustic Imaging in Layered Biological Tissues", In: "Advances in Optical Imaging and Photon Migration", vol. 21, ed. by R.R. Alfano, Academic Press (1994) pp. 161-165.
2. A.A. Oraevsky, S.L. Jacques, R.O. Esenaliev, F.K. Tittel: Laser based optoacoustic imaging in biological tissues, *Proc. SPIE* 1994; **2134A**: 122-128.
3. R.A. Kruger, P. Liu: Photoacoustic ultrasound: Pulse production and detection in 0.5% Liposyn, *Medical Physics*, 1994; **21**(7): 1179-1184.
4. R.A. Kruger: Photoacoustic ultrasound, *Med. Phys.* 1994; **21**(1): 127-131
5. A.A. Oraevsky, S.L. Jacques, F.K. Tittel: Measurement of tissue optical properties by time-resolved detection of laser-induced transient stress, *Applied Optics*, 1997; **36**(1): 402-415.

6. A.A. Oraevsky: Laser optoacoustic imaging for cancer diagnosis, *LEOS NewsLetter* 1996; **10**(6): 17-20.
7. A.A. Oraevsky, V.G.Andreev, A.A.Karabutov, R.O.Esenaliev, "Two-dimensional optoacoustic tomography: transducer array and image reconstruction algorithm", *SPIE Proceed.* **3601**, 256-267 (1999).
8. R.O. Esenaliev, A.A. Karabutov, A.A. Oraevsky: Sensitivity of laser opto-acoustic imaging in detection of small deeply embedded tumors, *IEEE J. ST Quant. Electr.* 1999; **5**(4):981-988.
9. G.J. Diebold, M.I. Khan, S.M. Park: "Photoacoustic signatures of particulate matter: optical production of acoustis monopole radiation", *Science* 1990; **250**: 101-104.
10. F.V. Bunkin, M.I. Tribelsky, *Sov.Phys.Uspekhi*, **130**, 193 (1980).
11. M.W. Sigrist, Laser generation of acoustic pulses, *J. Appl. Phys.*, **60**, R83 (1986).
12. R.O. Esenaliev, A.A. Karabutov, N.B. Podymova, V.S. Letokhov, "Laser ablation of aqueous solutions with spatially homogeneous and heterogeneous absorption", *Appl. Phys. B*, **59**, 73-81 (1994).
13. A.C. Beveridge, T.E. McGrath, G.J. Diebold, A.A. Karabutov, "Photoacoustic shock generation in carbon suspension", *Appl. Phys. Lett.*, **75**(26), 4204-4206 (1999).
14. S.J. Oldenburg, R.D. Averitt, S.L. Wescott, N.J. Halas: Nanoengineering of optical resonances, *Chem. Phys. Lett.* 1998; **288**: 243-247.
15. H. Pinto-Alphandary, A. Adremont, P. Couvreur: "Targeted delivery of antibiotics using liposomes and nanoparticles: research and applications. *Int. J. Antimicrob Agents* 2000; **13**(3):155-168.
16. H.M. Ellerby, R. Pasqualini et al. Anti-cancer activity of targeted pro-apoptotic peptides, *Nature Med.* 1999; **5**(9): 1032-1038.
17. L.M. Weiner, G.P. Adams: New approaches to antibody therapy, *Oncogene* 2000; **19**(53): 6144-6151.

# Optoacoustic images of early cancer in forward and backward modes

A.A. Karabutov<sup>1</sup>, V.G. Andreev<sup>1</sup>, B. Bell<sup>1</sup>, R.D. Fleming<sup>4</sup>, Z. Gatalica<sup>2</sup>, M. Motamedi<sup>1,4</sup>,  
E.V. Savateeva<sup>1</sup>, H. Singh<sup>3</sup>, S.V. Solomatin<sup>1</sup>, S.L. Thomsen<sup>6</sup>, P.M. Henrichs<sup>5</sup>, A.A. Oraevsky<sup>1</sup>

<sup>1</sup>Center for Biomedical Engineering, <sup>2</sup>Department of Pathology, <sup>3</sup>Department of Radiology,

<sup>4</sup>Department of Surgery, University of Texas Medical Branch at Galveston, Texas

<sup>5</sup>LaserSonix Technologies Inc., Houston, Texas, <sup>6</sup>MD Anderson Cancer Center, Houston, Texas

## ABSTRACT

Optoacoustic tomography combines advantages of pronounced optical contrast between different tissues and high resolution of wide-band ultrasound imaging. Laser pulses may be effectively used to produce acoustic sources in tissue with enhanced optical absorption. Ultrasonic waves can propagate in biological tissue with minimal distortion and deliver diagnostic information to the surface of tissue, where they may be detected with wide-band ultrasonic transducers. Current status of the optoacoustic tomography applied in early detection of cancerous lesions in the breast (utilizing forward mode) and in oral cavity (utilizing backward mode) is reviewed.

*Keywords: Optoacoustic imaging, in vivo diagnostics, breast cancer, ultrawide-band acoustic transducer, laser, ultrasound*

## 1. INTRODUCTION

Laser optoacoustic imaging system (LOIS) was proposed for cancer detection in order to combine advantages of optical contrast and sensitive, high-resolution ultrasonic detection in one tomography system [1-4]. One of the major applications of LOIS is the detection of early breast cancer [5-7]. Other cancerous lesions (such as in prostate and digestive system) having optical properties different from normal tissues also can be detected with optoacoustic tomography (OAT) [8-10]. OAT utilizes analysis of profiles of acoustic (ultrasonic) signals induced by laser pulses in tissue with tumors [11-13]. Application of the ultrawide-band ultrasonic detection instead of detection of photons helps to overcome problems associated with strong optical scattering in biological tissues and improve depth of monitoring, sensitivity and spatial resolution [14-16]. The profiles of acoustic waves generated under irradiation conditions of temporal pressure confinement in the volume of tissue resemble the profiles of absorbed laser energy in the tissue, and can be used to replicate the tissue structure. Tumors with dimensions of 1.5-mm to 15-mm irradiated with laser pulses represent themselves as sources of acoustic waves with ultrasonic frequencies of ~1 MHz to ~100 kHz. Such ultrasonic waves can propagate in biological tissues with insignificant attenuation [17,18]. Therefore, tumors in the breast can be detected at distances of up to 7-8 cm. However, spherical propagation of acoustic waves changes initial profile of absorbed laser energy (especially in the ultrasonic frequency range  $\leq 1$  MHz), so that the detected signals must be processed by integrating them over the entire time-course of detection in order to be used in the optoacoustic image reconstruction [5-7]. Smaller cancerous lesions or other tissue structures produce wider range of ultrasonic frequencies up to 100 MHz [17]. Due to stronger attenuation of high-frequency ultrasound, optoacoustic profiles arising from microscopic lesions and other profiles with fine structure or can be picked up from shallower depths of  $< 1$ -cm. The detection of ultrasonic waves can be achieved with ultrawide-band piezoelectric transducers [18-20] or optical interferometers [21-23]. The advantage of the former is superior sensitivity and low noise per unit bandwidth. The advantage of the latter is noncontact detection and rapid examination of large area.

There are two modes of detection for the laser-induced pressure transients (LIPT), termed as "forward" and "backward" modes. In both cases the irradiation of the surface of tissue under evaluation takes place through an optically and acoustically transparent buffer (such as quartz, water or plastic). This "optoacoustic buffer" permits good acoustic coupling to the tissue and incorporation of light delivery system and detection system. Usually as wide laser beam is employed for tissue illumination. The thermal pressure arising inside heated volume, due to rapid deposition of laser energy, yields ultrasonic transients launched in two opposite directions, one into absorbing and the other one into transparent buffer. The temporal shape of the LIPTs depends on the ratio of acoustic impedances of tissue and optoacoustic buffer [16-18] and may be different for LIPTs propagating forward into tissue and backward into optoacoustic buffer. In the forward mode, the detection is being made of LIPT launched into the tissue forward along the direction of the laser beam. The ultrasonic detection takes place at the rear surface of the irradiated tissue.

The temporal shapes of LEUT propagated into the absorbing medium are well established and quantitatively investigated both theoretically and experimentally (see, for example [18,24-26]). Their use is perspective for numerous applications, but in a case of the forward mode detection one has to have a two-sides access to the medium under investigation - both irradiated and rare surfaces of the medium have to be accessible. The backward mode of LEUT detection eliminates this problem. In this case the detection of ultrasonic transient takes place at the rear surface of transparent medium, coupled to investigated one (the irradiation of the absorbing medium is realized through the side of transparent medium). As the transparent medium can be taken smooth enough, an additional ultrasonic scattering and absorption in a course of ultrasonic wave propagation can be eliminated.

The two detection modes allow certain flexibility for *in vivo* and *in vitro* measurements and enables one to investigate both, the absorbed optical energy distribution [22,23] and ultrasonic back-scattering [18,26]. This paper reviews optoacoustic tomography of the breast cancer in the forward mode and imaging of early cancer in oral mucosa using the backward mode.

The initial years of our research in the area of optoacoustic imaging of the breast yielded the following results: (1) first clinical prototype system for the breast imaging was developed, fabricated and extensively tested in phantoms [10,12], (2) detection and localization of breast tumors in surgical mastectomy specimens were demonstrated [15], (3) parameters of LOIS were compared with X-ray mammography, MRI and ultrasound imaging [15]. The main merit of optoacoustic imaging was found in the possibility to utilize high tissue contrast based primarily on optical absorption and simultaneously preserve high resolution of ultrasonic imaging. The image contrast is defined as the difference in optoacoustic image brightness in tumors and in adjacent normal tissue divided to the brightness of normal tissue background. The value of optoacoustic contrast was found in the range of 1 to 5, which substantially exceeds any other endogenous tissue contrast currently utilized in medical imaging: ultrasonography, MRI and X-ray radiography. Based on preliminary comparative analysis of gross tumor cross-sections, immunohistology and optoacoustic images we hypothesize that the optoacoustic contrast results primarily from increased optical absorption in the dense microvasculature of the tumors [7,12]. However, optical scattering in tumors, especially those treated with chemo- and radiotherapy, may also significantly contribute to the optoacoustic contrast [27]. Thermoelastic properties of the breast tumors may also add to the optoacoustic contrast, however, were not yet quantified [28]. Comparison of optoacoustic images with those of X-ray radiography, MRI and ultrasound imaging performed *in vitro* revealed good correlation in tumor size and location, and the spatial resolution equal to that of ultrasound (better than 1 mm) was achieved [15].

In continuous effort of developing an imaging modality with better spatial resolution applicable for sensitive detection of variety of cancerous lesions, our group designed the optoacoustic front surface transducers (OAFST) operating in the backward mode, i.e. detecting acoustic profiles at the site of laser irradiation [29]. Feasibility study in characterization of tissue structure performed with of OAFST confirmed its utility for *in vivo* imaging of various skin lesions and cancer staging in oral cavity [30,31]. An ultrawide band of ultrasonic detection realized in OAFST yields in-depth resolution of about 15- $\mu$ m. In order to achieve lateral resolution of OAFST comparable with in-depth resolution, a focused optoacoustic front surface transducer was developed [28]. The new transducer design is referred to as Confocal Opto-Acoustic Transducer (COAT). The performance of COAT was initially tested in optically homogeneous and heterogeneous phantoms [29,31]. Experiments *in vivo* also were performed demonstrating capability of the developed transducer in imaging and distinguishing early stages of squamous cell carcinoma in oral mucous of golden hamsters [23-25].

## 2. OPTOACOUSTIC TOMOGRAPHY OF DEEP TUMORS IN THE BREAST

### 2.1. Laser Optoacoustic Imaging System

Schematic diagram of LOIS is shown in Fig. 1a. An Nd:YAG laser (Big Sky Lasers, MA) operating at 1064 nm was used as a source of pulses of 10-ns duration with repetition rate of 20 Hz. A quartz optical fiber was employed for the laser pulse delivery to the tissue surface. A telescope was used to expand laser beam from the fiber and deliver a parallel beam with diameter of 1-cm to the surface of the skin. A 32-element arc-shaped array of PVDF acoustic transducers was employed in LOIS for detection of LIPTs within ultrasonic frequency band of 20 kHz to 2 MHz (see Fig.1). An aperture angle of 120 degrees provides lateral resolution of about 1.2-mm, comparable with in-depth resolution of 0.8-mm, determined by frequency band of the transducer. On the other hand, this geometry provides sufficient resolution within the field of view of 50-mm x 80-mm around the focal zone. The sensitivity of the piezoelectric transducers was  $S = (10 \pm 2) \mu\text{V}/\text{Pa}$ . The noise level of the transducer with the preamplifier corresponded to the pressure value 2.5-3 Pa. The dynamic range of the ultrasonic detection system was estimates as 73 dB. These specifications make it possible to obtain high quality optoacoustic image at the depth of up to 80-mm using laser fluence of 20 mJ/cm<sup>2</sup> incident on the irradiated surface.

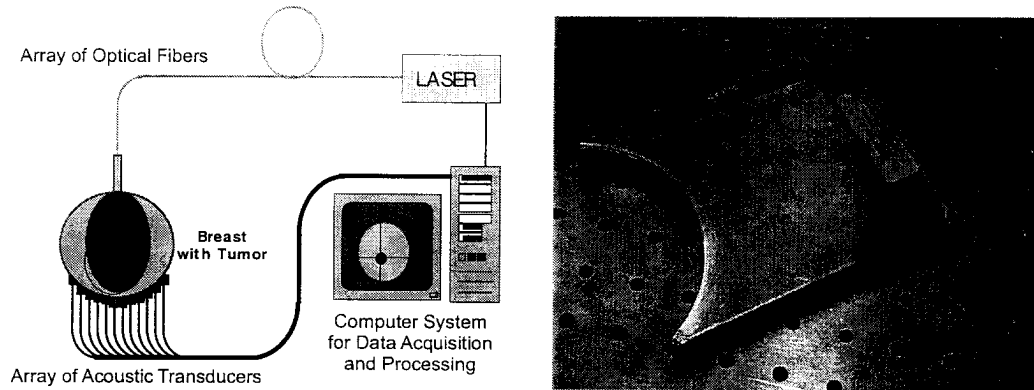


**Figure 1.** Schematic diagram of clinical LOIS (a) and a photograph of the 32-element arc transducer array (b).

Various band-pass filters were applied for optoacoustic signal treatment. They were used for elimination of exponential background, arisen due to regular attenuation and absorption of laser radiation in tissue. The location of irradiated surface area relatively to the transducer was determined from the optoacoustic signals and marked with bright line.

A radial back-projection algorithm, developed for the optoacoustic imaging and described in [10, 32-34] was employed. For the reconstruction of two-dimensional optoacoustic images we used signal integrals projected back onto the two-dimensional grid taking into account the directivity pattern (angle of acceptance) of each transducer in the array. The image represents distribution of a product of thermo-acoustic efficiency, optical absorption and absorbed laser energy. The back-projected images acquired with only limited number of detectors display artifacts associated with and image reconstruction using incomplete set of data. The contrast of these images could be improved through the image filtration procedure applied to the entire two-dimensional image [15]. However, unprocessed optoacoustic images contain quantitative information of distribution of absorbed optical energy in tissue. This quantitative information may be used for functional imaging and estimate of tissue optical properties.

Data acquisition in LOIS is realized with high efficient 32-channel 12-bit ADC. The laser pulse repetition rate was 20 Hz and averaging over 16 pulses are employed. Data processing and back-projected image formation takes 0.8 – 3 seconds (depending on the quantity of pixels in image). Image filtration takes 0.2 seconds. So, total time equals 2-4 sec. Current design of the laser optoacoustic imaging system (LOIS) allows operator to scan the acoustic detector array manually through the breast and to obtain images of chosen parts of the breast.

## 2.2. Initial Tests of Clinical LOIS

There is a strong evidence that malignant breast tumors have significantly enhanced content of deoxygenated blood in the tumor angiogenesis [35,36]. We hope that based on imaging hemoglobin vs deoxyhemo spectroscopic optoacoustic. Therefore, the Laser Optoacoustic Imaging system was tested in phantoms resembling breast with blood vessels. As shown in the diagram on Figure 2, the artificial blood vessels were located at different depths and were placed either parallel or perpendicular to the imaging plane. Position of the transducer array was at the bottom of the image (not shown). Surface position is visible as a bright area on the images. A single fiber was used for irradiation at only one location on the surface of the phantom. A photograph of the phantom is presented in Fig. 2 (right). The phantom was imaged twice, one time with optical fiber positioned at one point of its surface and the second time at the opposite position (the phantom was rotated 180 degrees).

Two-dimensional images of blood vessels of different diameter and filled with blood having different level of oxygenation is shown in Figure 3. Whole milk was diluted by water to obtain the effective optical attenuation coefficient  $1.4 \text{ cm}^{-1}$  in order to mimic the upper limit of optical scattering in the breast tissue at the wavelength of 1064 nm. Optical absorption coefficients of blood in vessels varied from 0.8 to 4.0 per cm depending on oxygen content. The first image was reconstructed using filtered optoacoustic signal in order to remove the exponential trend associated with effective optical attenuation (Fig. 3 left). The second image was not filtered, so that exponential profile of light distribution in the phantom could be observed (Fig. 3, right).

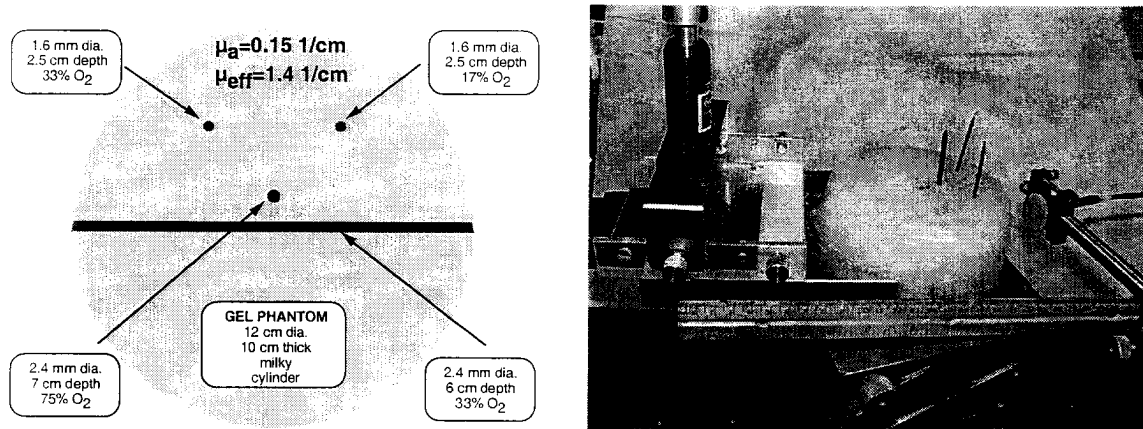


**Figure 2.** Left panel: Collagen gel phantom with artificial blood vessels filled with rabbit blood having various levels of oxygenation. Positions of blood vessels and percent of oxyhemoglobin are shown in windows. Optical properties of this phantom were similar to the optical properties of the breast at the wavelength of 1064 nm. Right panel: Photograph of the same phantom with artificial blood vessels. Transducer array and optical fiber are also presented on the photograph..

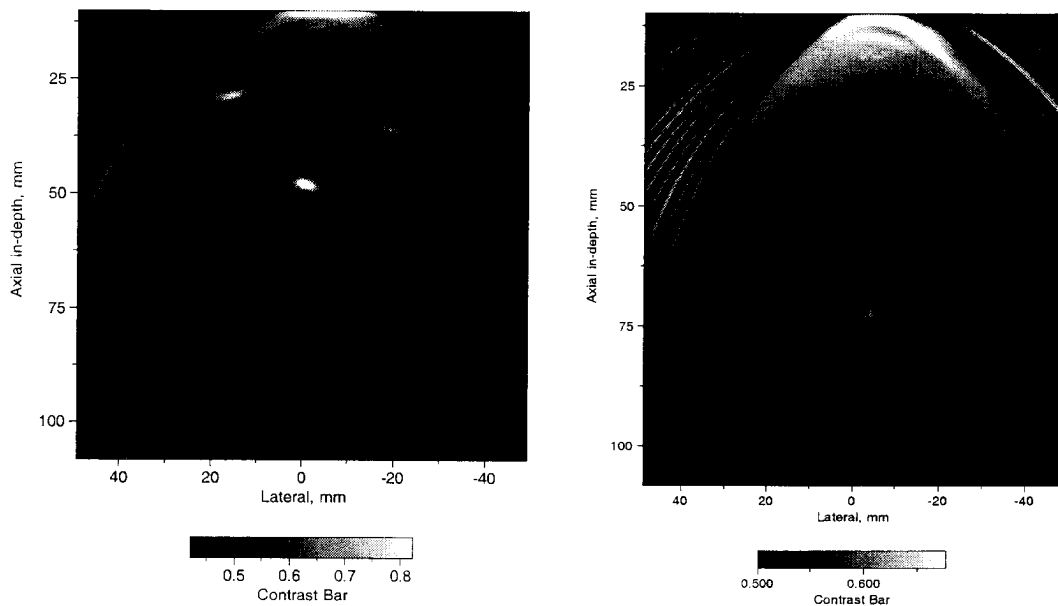


**Figure 3.** Optoacoustic image of blood vessels in milky gelatin phantom. Contrast of blood vessels relative to background is shown on Contrast Bar. Depth from the surface is depicted on the left vertical axis of each image.

The image of blood vessel cross-sections differs from the correct circular shape. This fact can be explained by limited angle aperture of the transducer. This limited lateral resolution in the far zone of the images presented in Fig. 3. An increase of the acceptance angle for the blood vessel located farther from the irradiation site and closer to the detector array resulted in a better reproduction of its circular cross-section in the image, as clearly depicted in Fig. 3 (right panel) showing an image of a blood vessel closer to the transducer. The angle of acceptance in this case is about 180° and as a consequence the shape of image highly correlates with real shape of the circle. Note that our image reconstruction algorithm allows accurate reproduction of spherical objects and cylindrical objects (see a blood vessel in the center going in horizontal direction). Thus, we may predict that objects with random shapes will be correctly reproduced on LOIS images.

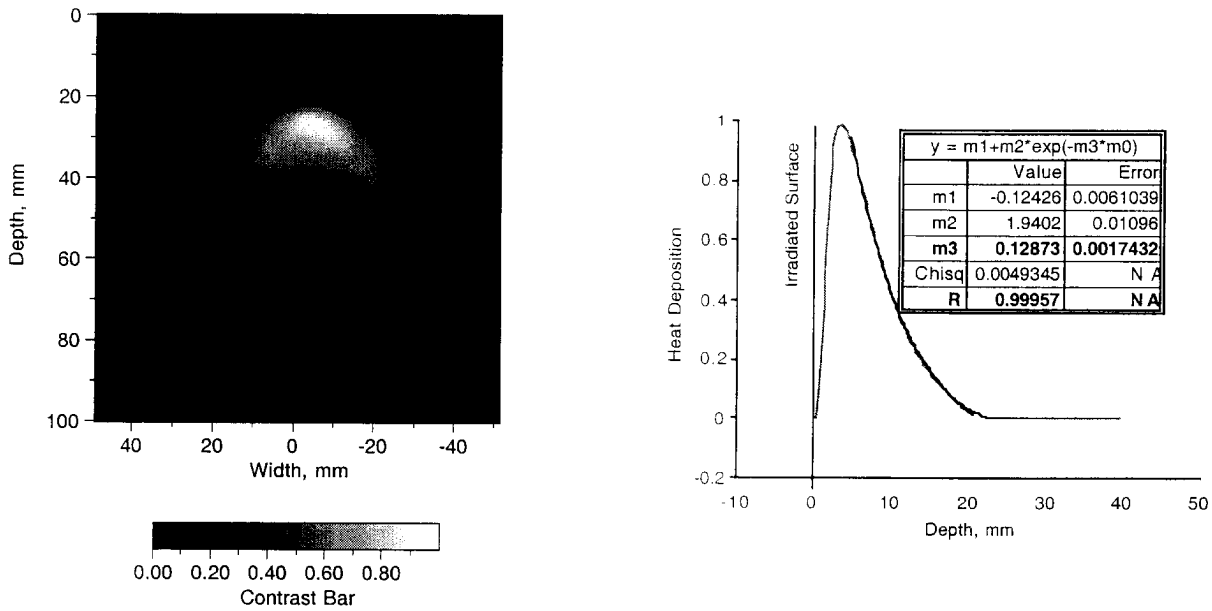


Figure 4. Optoacoustic image of human arm in the area of byiceps (left panel) and in-depth cross-section of this image resembling the profile of absorbed optical energy (right panel). The effective optical attenuation coefficient,  $\mu_{\text{eff}} = 1.28 \text{ cm}^{-1}$ .

All blood vessels were clearly resolved and depicted as separate objects. The relative position of the blood vessels as depicted on the optoacoustic images accurately resembles their position as shown on photograph Fig. 2 (right panel) and their depths are in good agreement with their real location. This imaging experiment demonstrated sensitivity of LOIS sufficient for detection of blood vessels at the depth of over 75 mm in an optical scattering and absorbing phantom. The brightness of the blood vessel images was proportional to the amount of absorbed optical energy, which in turn was proportional to the level of blood oxygenation in each vessel.

### 2.3. Quantitative Optoacoustic Imaging

Optoacoustic tomography visualizes the spatial distribution of absorbed optical energy in tissue. However, distortion of optoacoustic signals upon propagation through thick layers of tissue and signal processing may in principle modify the original profile. We tested possibility to obtain axial in depth profiles of absorbed optical energy from optoacoustic images from human muscle tissue. A human arm was imaged in the area of byiceps with LOIS designed for breast cancer imaging (see Fig.4).

Only high frequency filtering was applied to the optoacoustic image. This experiments demonstrated that quantitative information can be obtained from optoacoustic images. Neither signal correction for acoustic diffraction, nor reconstruction of absorbed optical energy distribution from optoacoustic signals, nor correction for sensitivity of individual piezoelectric transducers changed quantitative information. The effective optical attenuation coefficient,  $\mu_{\text{eff}} = 1.28 \text{ cm}^{-1}$ , determined from exponential fit of the optoacoustic profile, was in a good agreement with results of direct measurements of optical properties in this tissue.

### Imaging Breast Cancer *in vivo*

Eligible patients were chosen from the group of patients scheduled for radical surgical mastectomy with breast cancer diagnosed with x-ray mammography or a combination of x-ray mammography and other imaging modalities (ultrasound, MRI) and biopsy. The patients were imaged in the surgery room before surgery. Two-dimensional optoacoustic images were acquired in several locations on the breast with cancer. Irradiation with 16 pulses from a nanosecond Nd:YAG laser operating at the wavelength of 1064 nm was performed only at one site of breast skin surface. Optoacoustic transducer array was placed on the opposite side of the breast approximately beneath the point of irradiation. Irradiation point was placed approximately above the area suspicious of being a tumor. The exact location of tumors was not known prior to optoacoustic imaging procedure, however, approximate location could be determined from the mammogram. Tumors were sometimes palpable and biopsy incision was visible on the spared segment of skin. However, some tumors were not palpable and located deep within the breast. Two exemplary optoacoustic images of breast carcinoma are presented in Figure 5.

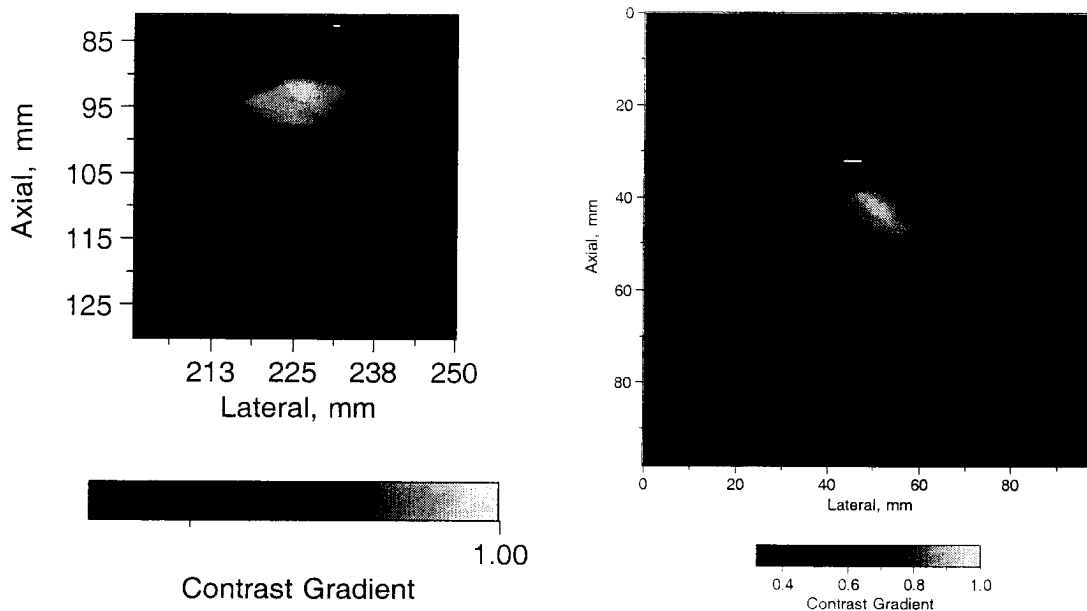


Figure 5. Optoacoustic image of a malignant tumor obtained *in vivo* (left, UTMB patient # 315221Q), Optoacoustic image of a malignant tumor obtained *in vivo* (right, UTMB patient # 026372P).

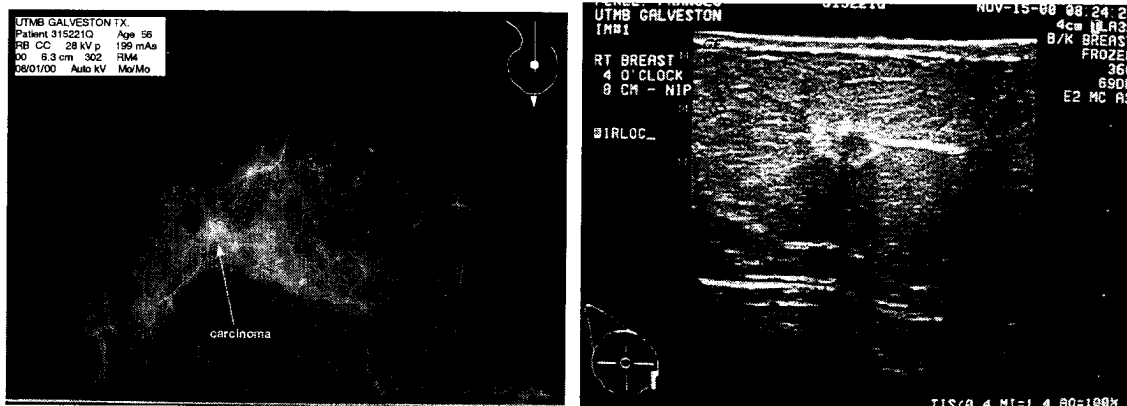


Figure 6. X-ray mammography image of a cancerous breast (left). There were 2 suspicious areas on mammogram, only one of them was a ductal carcinoma. Ultrasound image of the same breast showing malignant tumor. UTMB Patient # 315221.

The main conclusion that could be made from clinical experiments on breast cancer patients is that optoacoustic tomography provides enhanced contrast between normal tissues and cancerous tumors. This contrast varies, however, no one tumor of 5 tumors examined had contrast less than 1, i.e. the optoacoustic amplitude is twice higher in tumors relative to normal background. Optoacoustic images presented in Fig. 5 depict details of tumor structure based mainly on optical properties of cancerous tissues. Location of the tumors inside the breast and the tumor dimensions also were accurately determined from the optoacoustic images and confirmed through comparison with x-ray mammography, ultrasound and pathological examination (see Figure 6). Figure 6 presents x-ray mammography and ultrasound images of the breast with a malignant tumor, which was depicted in optoacoustic image in Fig. 5 (left). The position of the tumor relative to the skin surface was better determined from ultrasound image. However, detailed structure of the tumor was better visualized in x-ray mammography image. On the other hand, x-ray image depicted two areas suspicious of being cancerous, and only one area contained malignant tumor (as determined by pathology study). The tumor core brightly displayed in the optoacoustic image was not visible in neither x-ray or ultrasound images, but was confirmed after subsequent pathology examination. The dimension of a tumor core can be estimated as 10x7 mm. Tumor was detected at the depth of 11 mm from the surface. Contrast between the tumor and surrounding normal tissues in this image exceeds 1.2. The contrast in ultrasound image and x-ray mammography image of the same tumor did not exceed 0.1. Resolution of image visualization with LOIS (~ 1-mm) was comparable with that of x-ray mammography and ultrasound. Results of comparison between optoacoustic, ultrasonic and x-ray radiography images for the patient 026372 (see Fig. 5, right) and for the other 3 patients were qualitatively similar.

### 3. CONFOCAL OPTOACOUSTIC MICROSCOPY

#### Confocal Optoacoustic transducer

Confocal optoacoustic transducer has sharp focusing of the incident optical beam and narrow focus of the ultrasonic detection system. The distribution of focused light and the caustic of the ultrasonic detection form the volume of monitoring for the COAT. The schematic diagram of COAT is presented in Fig. 1. Pulsed laser radiation was delivered to the COAT via optical fiber, focused by a lens onto the tissue surface through opto-acoustic lens. Ultrasonic waves induced in tissue by laser pulses propagating backward through the opto-acoustic lens, were focused with the opto-acoustic lens onto the ring-shaped piezoelectric detector. Combination of flat piezo-transducer and opto-acoustic lens is aimed to obtain focused receiving ultrasonic transducer with narrow and long waist of the focal zone right under the irradiated tissue surface. The shape of the lens curvature allowed transformation of a spherical acoustic wave from tissue into a planar acoustic wave without phase distortion. A charge preamplifier was used to transform acoustic transducer signals into amplified electronic signals for further data acquisition and processing.

Laser pulses from a Q-switched Nd:YAG laser operating at the fundamental ( $\lambda=1.064 \mu\text{m}$ ), the second ( $\lambda=0.532 \mu\text{m}$ ) and the third ( $\lambda=0.355 \mu\text{m}$ ) harmonics were used in studies of light absorption distribution in phantoms and tissues. The temporal shape of laser pulses was close to Gaussian with full width at the max/e level  $2\tau_L=12\text{ns}$  for  $\lambda=532 \text{ nm}$  and  $2\tau_L=10\text{ns}$  for  $\lambda=355 \text{ nm}$ . The energy of each laser pulse was measured with a calibrated joulemeter (ED-200, GenTec, Canada). Sensitivity of the opto-acoustic transducer, permitted detection of ultrasonic waves with signal-to-noise ratio,  $\text{SNR}=1$  in tissues with absorption of  $20 \text{ cm}^{-1}$  while using incident laser fluence of  $F_0 < 1 \text{ mJ/cm}^2$ , suitable for safe application in medical imaging.<sup>21</sup>

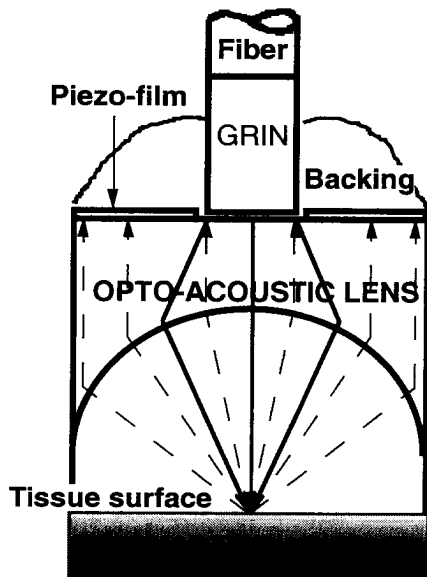


Figure 7. Principle schematics of Confocal Opto-Acoustic Transducer.

#### 3.2. Test experiments and tissue phantoms

Opto-acoustic imaging studies utilizing confocal optoacoustic transducer were carried out with optically clear solutions of potassium chromate and optically turbid (scattering) aqueous solutions of polystyrene microspheres colored with potassium chromate. A solution of 3.5 g of potassium chromate in  $10 \text{ cm}^3$  of water yields an absorption coefficient of about  $10^4 \text{ cm}^{-1}$  at the wavelength of 355 nm. Optical absorption coefficient of aqueous solutions at the wavelength of 355 nm was varied in the range from 70 to  $1,000 \text{ cm}^{-1}$  in order to study response of the opto-acoustic transducer to ultrasonic signals with various temporal shape and duration. Acoustic properties of solutions with different concentrations of potassium chromate were similar.

##### 3.2.1. Spectral sensitivity of COAT.

The spectral response of ultrasonic sensitivity for COAT is presented in Figure 8. This curve was obtained irradiating a thin layer of concentrated aqueous solution of potassium chromate ( $\mu_a \sim 10^4 \text{ cm}^{-1}$ ) placed onto the surface of the Opto-Acoustic lens. The absorbing solution was irradiated with a wide laser beam. The spectral response of COAT was calculated as a ratio of spectra of the detected opto-acoustic signal and the Fourier spectrum of laser pulse measured with fast photodiode. The spectral transfer function of laser generation of ultrasound for media with very strong optical absorption is constant. Therefore, laser-generated spectrum of opto-acoustic transients should coincide with the spectrum of the laser pulse.

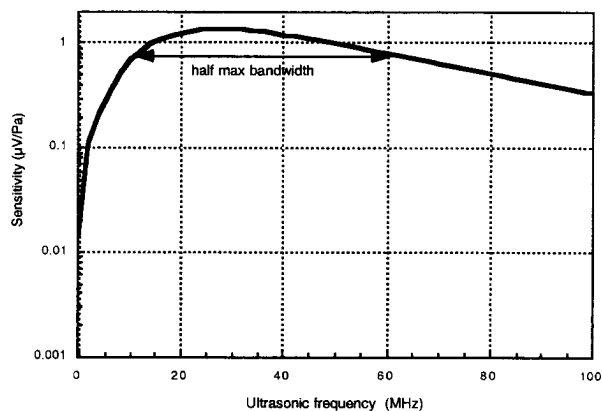


Figure 8. Absolute sensitivity of COAT

### 3.1.2. Reconstruction of light absorption.

A homogeneous absorbing media were employed to demonstrate the procedure of reconstruction of absorbed optical energy distribution. Aqueous solution of potassium chromate was irradiated by the third harmonic of Nd:YAG laser. The de-convolution of detected signal and reference OA-signal, obtained with high absorbing medium (light absorption coefficient about  $10^4 \text{ cm}^{-1}$ ), was applied. Figure 9 shows an example signal detected in potassium chromate solution with absorption coefficient of  $(6.5 \pm 0.1) \cdot 10^2 \text{ cm}^{-1}$  (line with dots). The profile of the optoacoustic transient depicted in Fig. 9 is determined by the optical absorption coefficient, the laser pulse duration, diffraction of ultrasonic wave and transducer sensitivity within the detected frequency band. The result of de-convolution is presented on Fig. 9 as a plain line. In clear absorbing aqueous solutions, the exponential slope of the opto-acoustic profile is defined solely by the optical absorption coefficient. Exponential fitting the slope yielded the absorption coefficient, which was equal to  $(648 \pm 8) \text{ cm}^{-1}$ .

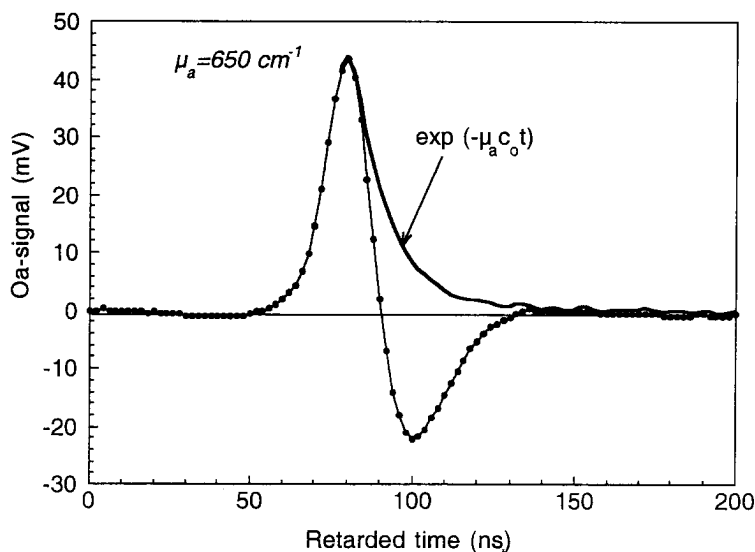


Figure 9. Opto-acoustic signal (line with dots) and reconstructed distribution of absorbed optical energy.

### 3.2.3. Image of cylindrical objects.

Polystyrene latex beads with average diameter of  $0.76 \mu\text{m}$  in  $\approx 1\%$  concentration were employed to make optically scattering solutions with effective scattering coefficient of  $10 \text{ cm}^{-1}$ . The first model object was aluminum wire with diameter of approximately  $100\text{-}\mu\text{m}$  placed in optically scattering solution at various depths from  $100 \mu\text{m}$  to  $1.5 \text{ mm}$ . The second model object was a human hair embedded in aqueous solution at the depth of  $600\text{-}\mu\text{m}$ . Thickness of the hair was measured with micrometer and equal  $80 \mu\text{m}$ . Thin wire and hair were imaged with COAT in order to determine in-depth and lateral resolution of the confocal opto-acoustic front surface transducer.

The Al wire was placed in polystyrene beads water suspension at various depths parallel to the transducer surface. Scans across the wire axis were performed. Opto-acoustic signal amplitude as a function of lateral coordinate is given in Figure 10. The full width at  $1/e$  of the amplitude equals to  $210 \mu\text{m}$  for  $290 \mu\text{m}$  depth, as measured from the curve in Fig. 10. The dependence widened with depth of detection. Therefore lateral resolution decreases with depth, as the opto-acoustic cone of detection widens.

The axial in-depth resolution within the transducer sensitive volume is equal to the thickness of tissue where laser-induced pressure is confined during laser energy deposition. This thickness is defined by the product of the laser pulse duration and the speed of sound in tissue and equal  $18\text{-}\mu\text{m}$ .

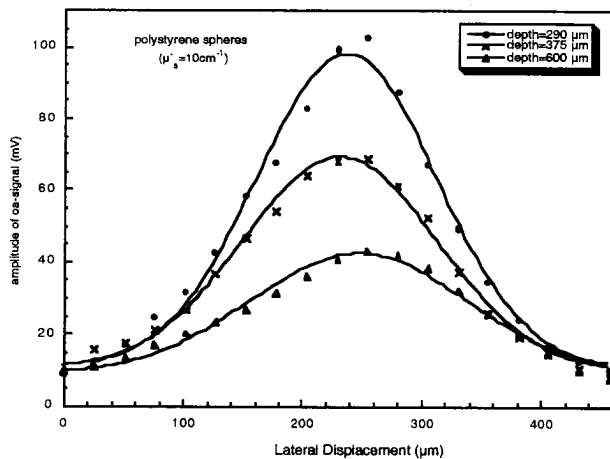


Figure 10. Signal amplitude dependences vs lateral displacement for various depth.

To demonstrate spatial resolution of the transducer opto-acoustic imaging of human hair was carried out. Hair with diameter of  $80 \mu\text{m}$  was placed in water and irradiated with green laser pulses. Scanning across the hair axis was performed with lateral step of  $25.4 \mu\text{m}$ . Obtained signals were processed using absorption reconstruction procedure and resulting image was created. The image is presented in Figure 11. It shows the hair as a bright strip with the thickness corresponding to the thickness of the hair, as in-depth resolution is high. The width of the image is several times greater, then the thickness due to relatively low angular aperture of the transducer. One can conclude, that in confocal laser optoacoustic microscopy the size of image in lateral direction will be greater then in-depth size according to angular aperture of optoacoustic lens.

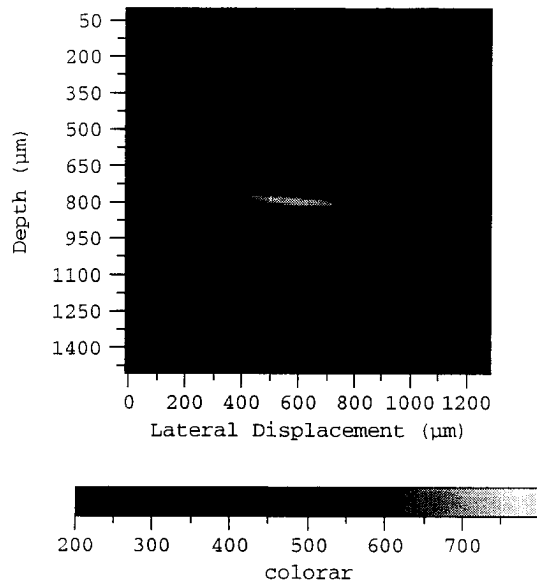


Figure 11. Opto-acoustic image of human hair.

### 3.3. Noninvasive detection of oral cancer *in vivo*

A well-established animal model of DMBA-induced squamous cell carcinoma in oral cavity was used in this study [35]. Syrian golden hamsters, weighing ~200 grams were employed. The motivation of using hamster model was the development of hamster buccal pouch carcinoma comparable to human oral cancer, as shown in [36,37]. DMBA solution (0.5% of 9,10-Dimethyl-1,2-Benzanthracene dissolved in mineral oil) was applied twice a week onto the buccal mucosa of the left cheek pouch using a small brush until the first lesion was visible with a naked eye. Photographs of the final lesions were taken and the animal was euthanized. Hamster pouches were cut, stretched and fixed with pins on a flat cork, and then embedded in paraffin. Tissue sections were stained with H&E (hematoxylin-eosin). Histological sections were used as a gold standard in order to compare with opto-acoustic images of different types of lesions and stages of squamous cell carcinoma (from dysplasia to carcinoma *in situ* to invasive malignant lesion).

Opto-acoustic imaging scans were performed every week during the lesion induction period. The procedure consisted of translating the transducer along the wet surface of pouch mucosa. A slight pressure was applied for better acoustic contact that resulted in flattening of irradiated tissue surface. Confocal opto-acoustic transducer was applied to the pouch surface with a thin water layer to provide acoustic coupling between the transducer and the tissue. During the experimental period, the animals had free access to food and water, except during the actual opto-acoustic measurements, when no food was allowed in order to prevent potential contamination of the opto-acoustic images.

The main goal of our study was to test feasibility of the proposed technique in detection and staging of cancer in oral mucosa. Previous studies performed with well-defined models of animal oral carcinoma consistently reported the following sequence of histologic changes that occur in the affected pouch mucosa: (1) hyperplasia, (2) dysplasia, (3) carcinoma *in situ*, (4) invasive carcinoma and (5) extensive tumors. Scanning of the opto-acoustic transducer along the cheek surface was performed to acquire data. Images presented below show a thin (10-30 µm) water layer as the top layer, so that the first mucosal surface is located at about 10-30-µm depth. The recorded signals were processed using reconstruction procedure (see section 2.4) and plotted on the two dimensional plane as 25-µm wide columns. Thereby reconstruction of two-dimensional images was made in hamsters with various stages of cancer development. Opto-acoustic images were compared with histological microscopic sections stained with hematoxylin-eosin.

#### Optoacoustic imaging of normal mucosa in oral cavity

Histological H&E sections of normal hamster cheek pouch were described in the literature previously.<sup>22-25</sup> There are several distinct layers in a normal cheek pouch. Figure 12 depicts a microscopic histology section (left) and corresponding opto-acoustic image of a normal hamster cheek pouch (right). Both, the histology and the opto-acoustic tomography display distinct layers that correspond to keratinized stratified squamous epithelium (E), a very thin basal membrane separating epithelium from mucosa of lamina propria (L), muscle fiber mucosa (M), submucosa connective tissue (S).

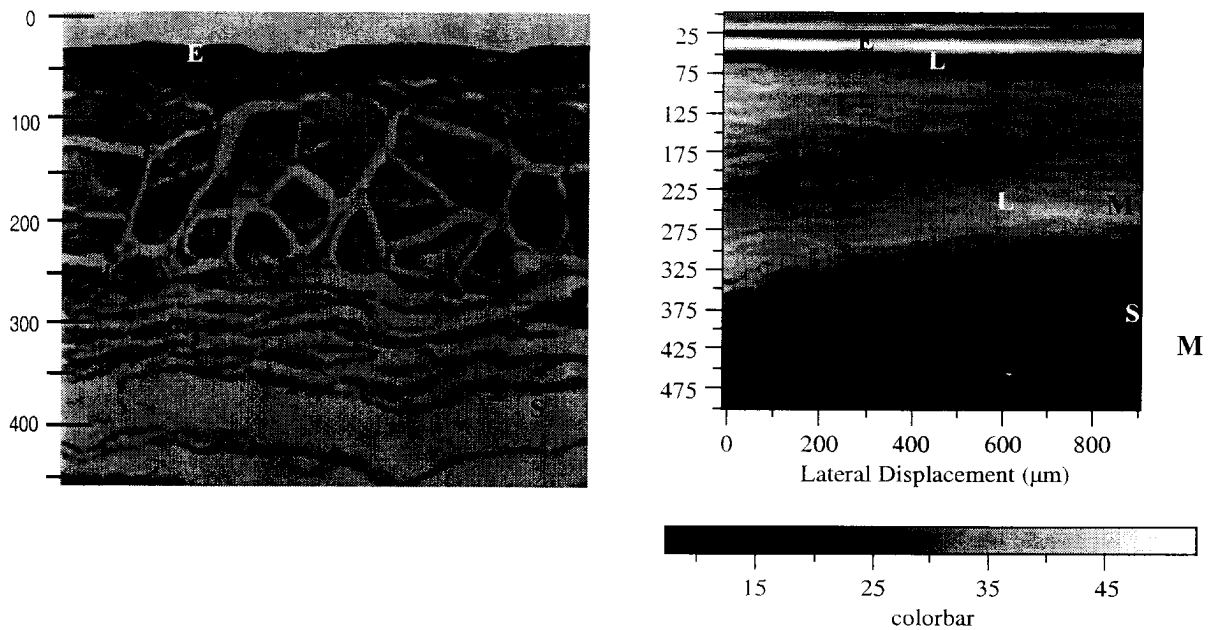


Fig. 12. Histological section and opto-acoustic image of hamster normal cheek pouch. Normal buccal mucosa pouch is characterized layered structure with distinct layers: keratin on top of epithelium (E), lamina propria (L) muscle fiber mucosa (M), submucosa connective tissue (S).

### 3.4.2 Displasia

A process of cancer development leads to gradual destruction in layered structure of mucosa. The earliest stage of cancer is characterized by hyperplasia and irregularly increased thickness of epithelium, however without compromise to the layered structure. Hyperplasia is an early precancerous stage, which can not be definitely outlined.

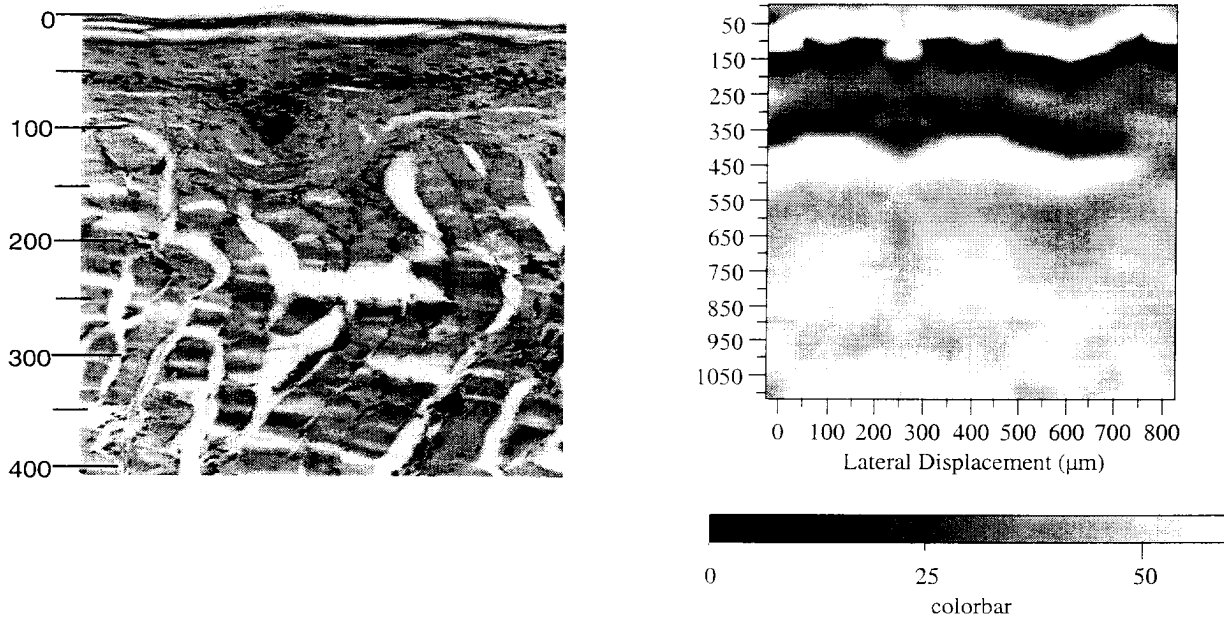


Figure 13. Earliest stage of cancer development. An opto-acoustic image measured *in vivo* from a normal hamster cheek pouch (right image) and corresponding microscopic histology section (left image) employing hematoxylin-eosin staining.

The second stage, displasia, is characterized with more prominent thickening of epithelium layer with rare and irregular breaks in the layered structure, made of local accumulation of epithelial cells with bigger nuclei and higher concentration of nuclei. Histological criteria used for determining dysplasia is irregular epithelial stratification. These abnormal epithelial cells

start proliferation into deeper mucosal layers. Histological section of dysplasia is depicted in Figure 8 (left). Opto-acoustic image presented in Fig. 13 (left) shows a focal point of dysplasia. The epithelium layer looks almost normal around the microscopic region with dysplasia.

### 3.4.3. Carcinoma *in situ*

Figure 14 presents histological section and opto-acoustic image of hamster pouch treated with DMBA for 6weeks (left picture). At this time microscopic malignant lesions could be found throughout the treated area.

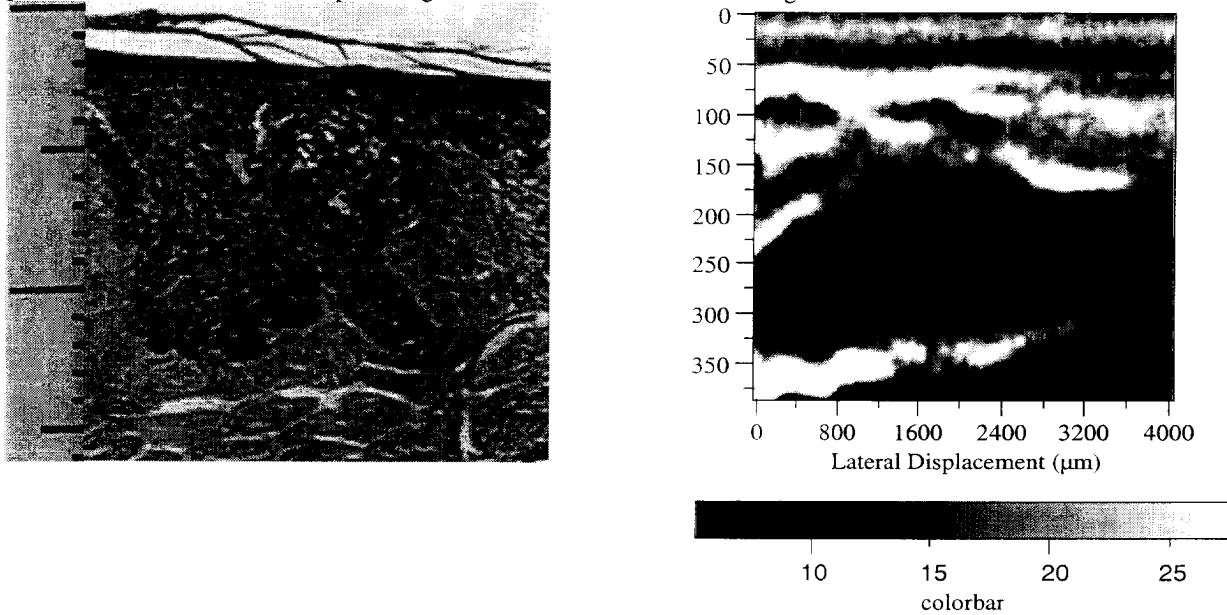


Figure 14. A microscopic histology section showing carcinoma *in situ* of a hamster cheek pouch treated with DMBA carcinogenic agent (left image, H&E staining) and corresponding opto-acoustic image (right image).

Microscopic squamous cell carcinoma *in situ* were noted in histology section by presence of acanthosis, lack of maturation, cellular atypia, mitoses. Opto-acoustic image (right) shows partial loss of layered tissue structure with local invasions of epithelial cells into deeper mucosa, irregularly shaped areas in mucosa of lamina propria.

### 3.4.4. Invasive carcinoma.

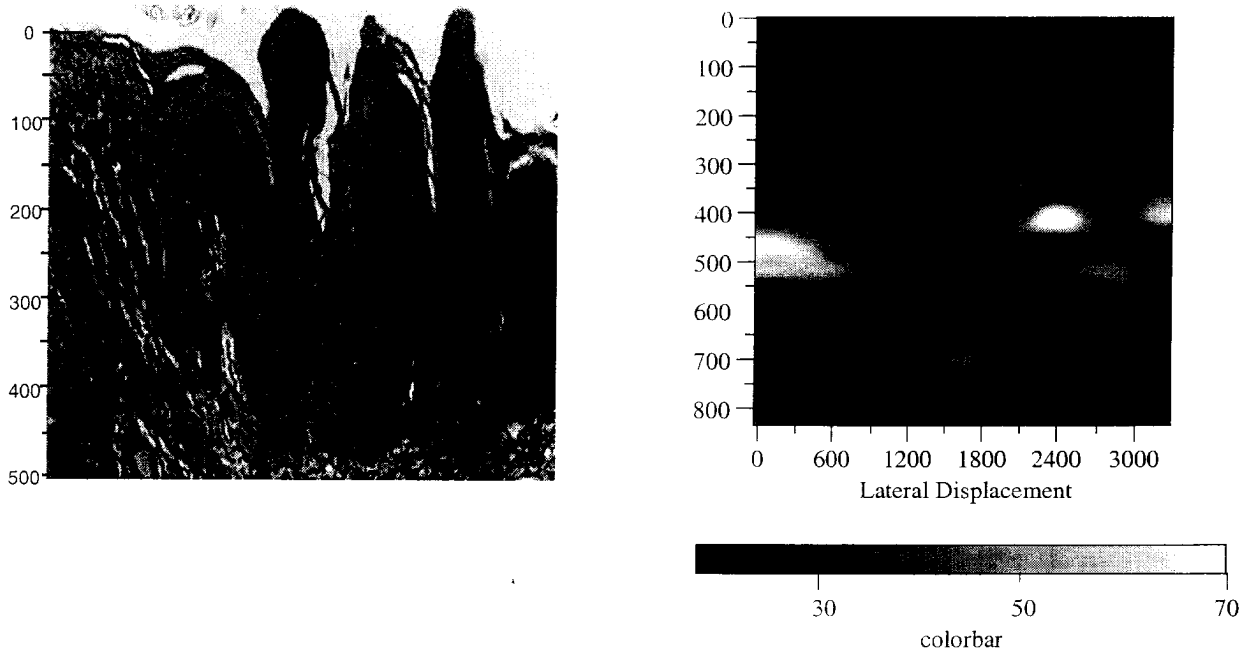


Figure 15. H&E stain of DMBA model treated during 12 weeks (left) and corresponding opto-acoustic image (right). Histological section of the hamster pouch shows invasive carcinoma. The tumor nests have an irregular outline with infiltrative borders.

Further progression of carcinoma development was observed in all animals by presence of invasive carcinoma. Hamster pouch treated with DMBA for 12 weeks showed structural changes characterized as multiple carcinomas *in situ* and invasive carcinomas. Scanning across lesion area was made and opto-acoustical image was reconstructed. A typical opto-acoustic image showing invasive carcinoma and correspondent histology H&E section are displayed in Figure 15).

## CONCLUSIONS

The first clinical prototype of the laser optoacoustic system for two-dimensional imaging of the breast *in vivo* was developed and employed for detection of breast cancer in 5 patients. The system employed an array of 32 elements of ultra wide-band PVDF transducers (20kHz-2MHz) shaped as an arc of 120 degrees. The system initially was tested in various phantoms and demonstrated specifications that make it suitable for high-contrast imaging human tissues. Sensitivity of LOIS permits detection of 2-mm blood vessels at the depth of 7.5 cm. In depth resolution equals 0.4 mm, lateral resolution is about 1 mm depending on position of tumor relative to the transducer array. Quantitative information on distribution of absorbed optical energy can be obtained from optoacoustic images. This clinical prototype LOIS is the basis for the next generations of three-dimensional imaging systems to be developed at UTMB in collaboration with LaserSonix Technologies, Inc. (Galveston, TX).

A novel confocal opto-acoustic transducer for imaging layered tissues *in vivo* was developed. This transducer combines focused optical system for laser irradiation of tissue and a focused piezoelectric detection system operating in the ultrasonic band of 1MHz to 100 MHz.

Axial in-depth resolution of the transducer is 15  $\mu\text{m}$  for biological tissue. Lateral resolution is not worse than 60  $\mu\text{m}$  at the depth of up to 600  $\mu\text{m}$ . The major advantage of COAT compared with OAFST is improved lateral resolution over the range of depths in tissue from 0 to 1.5 mm. A deconvolution procedure for reconstruction of absorbed energy distribution was developed and tested yielding satisfactory accuracy of quantitative analysis.

Confocal opto-acoustic imaging was sufficiently sensitive to depict structural changes in mucosal tissues much earlier than any changes could be noticed on the tissue surface with naked eye. Furthermore, the opto-acoustic images yielded information of in-depth tissue structure that closely resembled structures provided by optical microscopy of histology sections. Microscopic dysplasia can be differentiated from the normal mucosa and carcinoma *in situ* could be differentiated from dysplasia. The differentiation of the invasive carcinoma from normal and precancerous lesions was very prominent. Changes associated with gradual cancer development could be characterized as a transformation of tissue layered structure into a heterogeneous structure. The nature of the opto-acoustic contrast in mucosa and carcinoma needs to be established in order to enhance further the imaging sensitivity. We speculate that differentiation of cancer is based on tumor angiogenesis.

The results of the presented studies confirmed feasibility of COAT technique in differentiation of normal mucosa from cancerous, and in characterization of early stages of squamous cell carcinoma in animal model. The results from the *in vivo* study suggest that there is a potential for confocal opto-acoustic tomography for imaging, monitoring and guiding biopsy.

## 5. ACKNOWLEDGMENTS

This work was supported by the National Cancer Institute (grant #R29-CA80221), DOD Breast Cancer Research Program, US Army (grant #DAMD17-99-1-9404) and US Civilian Research and Development Foundation (grant # RP2-2109), Advanced Technology Program of the Texas Higher Education Coordinating Board (grant # 004952-054), and UTMB Technology Program.

## 6. REFERENCES

- A.A. Oraevsky, S.L. Jacques, R.O. Esenaliev, F.K. Tittel: Time-Resolved Optoacoustic Imaging in Layered Biological Tissues", In: "Advances in Optical Imaging and Photon Migration", vol. 21, ed. by R.R. Alfano, Academic Press (1994) pp. 161-165.
- A.A. Oraevsky, S.L. Jacques, R.O. Esenaliev, F.K. Tittel: Laser based optoacoustic imaging in biological tissues, *Proc. SPIE* 1994; 2134A: 122-128.
- R.A. Kruger, P. Liu: Photoacoustic ultrasound: Pulse production and detection in 0.5% Liposyn, *Medical Physics*, 1994; 21(7): 1179-1184.

- A.A. Oraevsky, R.O. Esenaliev, S.L. Jacques, S. Thomsen, F.K. Tittel: Lateral and z-axial resolution in laser optoacoustic imaging with ultrasonic transducers, *Proc. SPIE* 1995; 2389: 198-208.
- RA Kruger: Photoacoustic ultrasound, *Med. Phys.* 1994; 21(1): 127-131
- A.A. Oraevsky: Laser optoacoustic imaging for cancer diagnosis, *LEOS NewsLetter* 1996; 10(6): 17-20.
- A.A. Oraevsky, R.O. Esenaliev, S.L. Jacques, F.K. Tittel: Laser Opto-Acoustic Tomography for medical diagnostics: principles, *Proc. SPIE* 1996; 2676: 22-31.
- A.A. Oraevsky, R.O. Esenaliev, S.L. Jacques, F.K. Tittel, D. Medina: "Breast Cancer Diagnostics by Laser Optoacoustic Tomography", In: "Trends in Optics and Photonics", vol. II, ed. by R.R. Alfano and J.G. Fujimoto, OSA Publishing House, pp. 316-321 (1996).
- A.A. Oraevsky, R.O. Esenaliev, S.L. Jacques, S. Thomsen, F.K. Tittel: Lateral and z-axial resolution in laser optoacoustic imaging with ultrasonic transducers, *Proc. SPIE* 1995; 2389: 198-208.
- A.A. Oraevsky, V.G. Andreev, A.A. Karabutov, R.O. Esenaliev: Two-dimensional optoacoustic tomography: array transducers and image reconstruction algorithm, *Proc. SPIE* 3601: 256-267 (1999).
- R.O. Esenaliev, A.A. Karabutov, A.A. Oraevsky: Sensitivity of laser opto-acoustic imaging in detection of small deeply embedded tumors, *IEEE J. ST Quant. Electr.* 1999; 5(4):981-988.
- A.A. Oraevsky, A.A. Karabutov, V.G. Andreev, R.O. Esenaliev: Laser opto-acoustic imaging of the breast: Detection of cancer angiogenesis, *Proc. SPIE* 3597: 352-363 (1999).
- A.A. Karabutov, N.B. Podymova, V.S. Letokhov: Time-resolved laser optoacoustic tomography of inhomogeneous media, *Appl. Phys. B* 63, pp. 545-563, 1996.
- A.A. Oraevsky, R.O. Esenaliev, A.A. Karabutov: Laser optoacoustic tomography of layered tissues: signal processing, *Proc. SPIE* 1997; 2979: 59-70.
- V.A. Andreev, A.A. Karabutov, V.S. Solomatin, E.V. Savateeva, V.A. Aleynikov, Y.V. Julina, D.R. Fleming, A.A. Oraevsky: Optoacoustic Tomography of tumors in the breast, *Proc. SPIE* 2000; 3916: 36-47.
- A.C. Tam *Rev Mod. Phys.* 58, 381 (1986).
- W. Arnold, B. Hoffmann, H. Willems, "Crack depth estimation by photoacoustic microscopy", *Zeitschrift fur Physik B.- Condensed Matter*, 64, 31-34 (1986).
- V.E. Gusev, A.A. Karabutov, *Laser optoacoustics*. (AIP, New-York, 1993).
- A.A. Karabutov, M.P. Matrosov, N.B. Podymova, V.A. Pyzh, "Acoustic pulse spectroscopy using a laser sound source", *Sov. Physics. Acoustics* 37(2), 157-163 (1991).
- B. Haberer, M. Paul, H. Willems, W. Arnold, Measurement of internal friction in polycrystalline materials using laser-generated ultrasound, *J. of Alloys and Compounds*, 211-212, 636-639 (1994).
- A.A. Karabutov, N.B. Podymova "Nondestructive evaluation of fatigue changes of composite structure by laser-excited ultrasonic waves", *Proceed. SPIE* 3396, 255 (1998).
- A.A. Karabutov, N.B. Podymova, V.S. Letokhov, "Time-resolved optoacoustic tomography of inhomogeneous media", *Applied Physics B* 63, 545-563 (1996).
- S.M. Park, M.I. Khan, H.Z. Cheng, G.J. Diebold, "Photoacoustic effect in strongly absorbing fluids", *Ultrasonics* 29(1), p. 63-68 (1991).
- M.I. Khan, T. Sun, G.J. Diebold, "Photoacoustic waves generated by absorption of laser radiation in optically thin layers", *J. Acoust. Soc. Am.* 93(3), 1417-1425 (1993).
- A.A. Oraevsky, A.A. Karabutov, V.V. Murashov, N.B. Podymova, "Laser opto-acoustic inspection of layered composites", *Proceed. SPIE* 3396, 103 (1998).
- N. Weidner, J.P. Semple, W.R. Welch, and J. Folkman: Tumor angiogenesis and metastasis - correlation in invasive breast carcinoma, *New Engl. J. Med.*, 324, pp. 1-7, 1991.
- A.A. Karabutov, A.A. Oraevsky: Ultimate sensitivity of wide-band detection for laser-induced ultrasonic transients, *Proc. SPIE* 2000; 3916: 228-239.
- N. Ghosh, S.K. Mohanty, S.K. Majumder, P.K. Gupta: Measurement of optical transport properties of normal and malignant human breast tissue, *Appl. Optics* 2001; 40(1): 176-184.
- A. Oraevsky: Nanosecond acoustic transducer with applications in laser medicine, *LEOS Newsletter* 8(1), pp. 6-8, 1994.
- A.A. Karabutov, E.V. Savateeva, A.A. Oraevsky: Imaging of layered structures in biological tissues with opto-acoustic front surface transducer, *SPIE* 3601, pp. 284-295 1999.
- A.A. Oraevsky, A.A. Karabutov, E.V. Savateeva, B. Bell, M. Motamedi, S.L. Thomsen, P.J. Pasricha: Opto-acoustic imaging of oral cancer: Feasibility studies in hamster model of squamous cell carcinoma, *SPIE* 3597, pp. 385-396, 1999.
- G.S. Kino: "Acoustic waves. Devices, imaging, and analog signal processing", Prentice-Hall, Englewood Cliffs, 1987.
- P. Liu: Image reconstruction from photoacoustic pressure signals. *Proc. SPIE* 2681: 285 - 296 (1999).
- K.C. Ternovoy, M.V. Sinkov: "Introduction to modern tomography", Naukova Dumka, Kyiv, Ukraine (1996).
- T.J. Slaga, I.B. Gimenez-Conti, An animal model for oral cancer, *J. Natl. Cancer Inst.*, Review, 13, pp. 55-60 1992.

H. Santis, G. Shlar, H.H. Chauncey: Histochemistry of experimentally induced leukoplakia and carcinoma of the hamster buccal pouch, *Oral Surg.*, 17, p. 307, 1964.

J.D. Schribner, R. Suss: Tumor initiation and promotion, *Int. Rev. Exp. Pathol.*, 8, p. 137, 1978.